

THESIS

THE BIRTH AND DEATH OF THE MJO: AN OBSERVATIONAL STUDY

Submitted by

James J. Benedict

Department of Atmospheric Science

In partial fulfillment of the requirements
for the Degree of Master of Science
Colorado State University
Fort Collins, Colorado
Spring 2005

COLORADO STATE UNIVERSITY

MARCH 9, 2005

WE HEREBY RECOMMEND THAT THE THESIS PREPARED UNDER OUR SUPERVISION BY JAMES JOSEPH BENEDICT ENTITLED THE BIRTH AND DEATH OF THE MJO: AN OBSERVATIONAL STUDY BE ACCEPTED AS FULFILLING IN PART REQUIREMENTS FOR THE DEGREE OF MASTER OF SCIENCE.

Committee on Graduate Work

Allan T. Kirkpatrick

Roland A. Madden

David W. J. Thompson

David A. Randall, Advisor

Jeffrey L. Collett, Department Head

ABSTRACT OF THESIS

THE BIRTH AND DEATH OF THE MJO: AN OBSERVATIONAL STUDY

The Madden-Julian Oscillation (MJO), an eastward-propagating equatorial wave most active during the boreal winter, dominates atmospheric intraseasonal (10-100 day) variability in the tropical Indian and West Pacific Ocean areas. This phenomenon is characterized by cyclic periods of suppressed convection (dry phase) and intense rainfall (wet phase). In this study, we examine important physical mechanisms observed during the “birth” (wet phase approach) and “death” (wet phase departure) of the MJO.

Analyses of single events and event composites based on TRMM precipitation highlight cogent features of the MJO. Unlike previous studies, we base MJO events on hydrological activity due to its strong ties to latent heating, the primary driver of tropical circulations. Dynamical fields of mesoscale resolution are diagnosed from ECMWF reanalysis datasets (ERA40).

Prior to the onset of intense rainfall, a slow increase in low-level temperature and moisture leads to greater instability. An enhancement of shallow cumulus activity, as inferred from the reanalysis data, is associated with increased moisture detrainment and an erosion of a mid-tropospheric dry layer. In this stage, vertical moisture advection is dominant over the horizontal component.

The “death” of the MJO involves immediate and delayed drying processes. Within five days after maximum rainfall, we observe anomalous low-level drying by horizontal advection during a time of weak moistening by vertical motions. This

immediate drying has not been analyzed explicitly in previous composite studies. Subsidence drying is delayed, beginning and then peaking one and two weeks after intense precipitation, respectively.

Physical attributes of the composite results are compared to current wave instability theories. Our findings lend support to the discharge-recharge mechanism which involves a gradual, local build-up of instability.

Currently, no widely-accepted theory exists that can fully explain the MJO. Accurately diagnosing and modeling this phenomenon is of critical importance for weather and climate studies. It is our hope that this study contributes toward an improved understanding of the MJO and its depiction in atmospheric models.

James J. Benedict
Department of Atmospheric Science
Colorado State University
Fort Collins, CO 80523
Spring 2005

ACKNOWLEDGMENTS

This thesis would not have been possible without the help of my advisor, Dr. David A. Randall. I am extremely grateful for his guidance and encouragement. It is truly an honor to have the opportunity to work with and learn from him. I would also like to thank Drs. Roland A. Madden, David D. J. Thompson, and Allan T. Kirkpatrick for their participation as members of my thesis committee.

Special thanks is owed to the Randall research group—particularly Takanobu Yamaguchi and Maike Ahlgrimm—for our invaluable scientific discussions. To my parents, family, friends, and former teachers, you made writing this thesis that much easier.

This research project was funded by Department of Energy (DOE) Atmospheric Radiation Measurement (ARM) program grant DE-FG02-02ER63370, National Aeronautics and Space Administration (NASA) contract NNG04G125G, and National Science Foundation (NSF) grant ATM-981212384.

TABLE OF CONTENTS

SIGNATURE PAGE.....	ii
ABSTRACT OF THESIS.....	iii
ACKNOWLEDGMENTS.....	v
TABLE OF CONTENTS.....	vi
LIST OF TABLES.....	viii
LIST OF FIGURES.....	ix
Chapter 1: Introduction.....	1
Chapter 2: Data and Methodology.....	9
2.1. Data Sources.....	9
2.2. Methodology.....	14
2.2.1. General statistical methods.....	14
2.2.2. Meridionally-averaged framework.....	18
2.2.3. Gridpoint-based framework.....	20
Chapter 3: Results and Discussion I: Composites of Basic Variables.....	21
3.1. What Do the Tropics Look Like?.....	21
3.2. Sensitivity Testing of Filtering and Event Selection Criteria.....	30
3.3. Meridionally-averaged Composite Results.....	32
3.4. Gridpoint-based Composite Results.....	42

Chapter 4: Results and Discussion II: Mechanisms of the MJO.....	52
4.1. Advective and Convective Processes of the MJO.....	53
4.1.1. Horizontal and vertical components of advective transport of heat and moisture.....	53
4.1.2. Convective processes of the MJO (Q_1 and Q_2).....	61
4.2. Putting It All Together.....	68
4.2.1. Driving heat and moisture variances.....	69
4.2.2. Spatial composite, gridpoint-based.....	81
4.2.3. Single event (spatial), gridpoint-based (21 October 1998).....	86
4.2.4. Wave theories and the MJO: How does it work?.....	94
4.2.5. Comments on statistical significance.....	101
4.3. Exploratory Analyses.....	103
4.3.1. Comments on the precipitation budget.....	104
4.3.2. Cloud-top characteristics: GLAS and MODIS.....	107
Chapter 5: Summary and Conclusions.....	111
APPENDIX A: Composite Anomaly Calculation.....	115
APPENDIX B: Heat and Moisture Budget Analysis: Advective Form.....	117
APPENDIX C: Simple Forms of the Apparent Convective Heat Source (Q_1) and Apparent Moisture Sink (Q_2).....	120
REFERENCES.....	123

LIST OF TABLES

TABLE 2.1: Specifications of datasets used in analysis.....	10
TABLE 3.1: Comparison of several atmospheric and oceanic ERA40 variables between long-term climatology and the MJO “background state”.....	28
TABLE 3.2: Specifications of MJO events based on meridionally-averaged (10°S- 5°N) TRMM precipitation.....	33
TABLE 3.3: Specifications of MJO events based on individual gridpoint-based TRMM precipitation.....	43
TABLE 4.1: Boreal winter-mean (NDJF) hydrologic variables associated with Equation.....	106

LIST OF FIGURES

FIG. 1.1: Longitude-height schematic diagram of MJO wave propagation.....	4
FIG. 2.1: Schematic representation of the source data date ranges in this analysis.....	11
FIG. 2.2: Example of the application of spectral filtering on a raw data field.....	16
FIG. 3.1: Annual (left) and October-April (right) accumulated total precipitation from TRMM (top) and ECMWF 40-yr Reanalysis (ERA40; bottom).....	22
FIG. 3.2: October-April mean zonal winds (u) at 200 hPa (top) and 850 hPa (bottom).....	23
FIG. 3.3: October-April mean meridional winds (v) at 200 hPa (top) and 850 hPa (bottom).....	24
FIG. 3.4: October-April mean pressure velocities (w) at 400 hPa (top; near level of expected maximum vertical motions in the Tropics) and 850 hPa (bottom).....	25
FIG. 3.5: October-April mean outgoing longwave radiation (OLR). Lower values represent colder, higher clouds tops and areas of deeper convection.....	25
FIG. 3.6: Vertical profiles of the “MJO background state” (solid black lines) and 18-year climatology (1984-2001; dotted green lines).....	27
FIG. 3.7: Spectral power diagrams of tropical wave types based on asymmetric (a) and symmetric (b) TRMM rainfall data about the Equator.....	29

FIG. 3.8: Map of the eleven MJO events, detected both in the TRMM and ERA40 datasets, that make up the composite time-height cross-sections seen in Section 3.3 (red), as well as the more recent TRMM-based events that occurred after the end of the ERA40 analysis period (blue).....	32
FIG. 3.9: Time-height cross-sections of zonal wind anomalies (u') during the composite MJO event based on the meridionally-averaged (10°S - 5°N) framework.....	34
FIG. 3.10: As in Fig. 3.9, but for anomalous meridional wind magnitudes ($ v' $).....	34
FIG. 3.11: As in Fig. 3.9, but for pressure velocity anomalies (ω').....	36
FIG. 3.12: As in Fig. 3.9, but for temperature anomalies (T').....	36
FIG. 3.13: As in Fig. 3.9, but for specific humidity anomalies (q').....	37
FIG. 3.14: As in Fig. 3.9, but for relative humidity anomalies (RH').....	37
FIG. 3.15: Composite timeseries of the departures of surface latent heat flux (SLHF') from the MJO background state for the meridionally-averaged (10°S - 5°N) framework.....	39
FIG. 3.16: As in Fig. 3.15, but for precipitable water anomalies (PW').....	39
FIG. 3.17: As in Fig. 3.15, but for mean sea-level pressure anomalies (MSLP').....	40
FIG. 3.18: As in Fig. 3.15, but for MODIS-derived cloud-top pressure (CTP).....	40
FIG. 3.19: As in Fig. 3.15, but for anomalous sea-surface temperatures (SST' ; solid orange line) and anomalous solar radiation absorbed at the surface (SSA' ; dotted purple line).....	41
FIG. 3.20: As in Fig. 3.15, but for anomalous outgoing longwave radiation (OLR' ; solid green line) and anomalous brightness temperature (T_b' ; dotted blue line).....	41

FIG. 3.21: Map of the nine MJO events, detected both in the TRMM and ERA40 datasets, that make up the composite time-height cross-sections seen in Section 3.4 (red), as well as the more recent TRMM-based events that occurred after the ERA40 analysis period (blue).....	42
FIG. 3.22: Time-height cross-sections of zonal wind anomalies (u') during the composite MJO event based on the individual gridpoint framework.....	44
FIG. 3.23: As in Fig. 3.22, but for meridional wind anomalies (v').....	44
FIG. 3.24: Time-height cross-sections of anomalous pressure velocities (ω' ; hPa/s x 100) for the MJO gridpoint composite event based on events selected with use of 20-100-day filtered TRMM rainfall.....	45
FIG. 3.25: As in Fig. 3.24, but for the MJO gridpoint composite event based on events selected with use of 10-100-day filtered TRMM rainfall.....	45
FIG. 3.26: As in Fig. 3.22, but for temperature anomalies (T').....	46
FIG. 3.27: Time-height cross-sections of anomalous specific humidity (q') for the MJO gridpoint composite event based on events selected with use of 20-100-day filtered TRMM rainfall.....	47
FIG. 3.28: As in Fig. 3.27, but for the MJO gridpoint composite event based on events selected with use of 10-100-day filtered TRMM rainfall.....	47
FIG. 3.29: Time-height cross-sections of anomalous relative humidity (RH') for the MJO gridpoint composite event based on events selected with use of 20-100-day filtered TRMM rainfall.....	48
FIG. 3.30: As in Fig. 3.29, but for the MJO gridpoint composite event based on events selected with use of 10-100-day filtered TRMM rainfall.....	48
FIG. 3.31: Composite timeseries of the departure of surface latent heat flux	

(SLHF') from the MJO background state for the individual gridpoint framework.....	49
FIG. 3.32: As in Fig. 3.31, but for precipitable water anomalies (PW').....	49
FIG. 3.33: As in Fig. 3.31, but for mean sea-level pressure anomalies (MSLP').....	49
FIG. 3.34: As in Fig. 3.31, but for MODIS-derived cloud-top pressure (CTP).....	49
FIG. 3.35: As in Fig. 3.31, but for anomalous sea-surface temperatures (SST'; solid orange line) and anomalous solar radiation absorbed at the surface (SSA'; dotted purple line).....	50
FIG. 3.36: As in Fig. 3.31, but for anomalous outgoing longwave radiation (OLR'; solid green line) and anomalous brightness temperature (T_b '; dotted blue line).....	50
FIG. 4.1: Time-height cross-sections of the (a) zonal, (b) meridional, and (c) vertical components of the anomalous time rate of change of drying for the meridionally-averaged (10°S-5°N) framework.....	54
FIG. 4.2: As in Figure 4.1, but for the individual gridpoint framework and based on events selected with use of 20-100-day filtered TRMM rainfall.....	55
FIG. 4.3: As in Figure 4.1, but for the individual gridpoint framework and based on events selected with use of 10-100-day filtered TRMM rainfall.....	56
FIG. 4.4: Time-height cross-section of total vertical advective contribution to the anomalous time rate of change of temperature for the meridionally-averaged (10°S-5°N) framework.....	58
FIG. 4.5: As in Figure 4.4, but for the individual gridpoint framework and based on events selected with use of 20-100-day filtered TRMM rainfall.....	58

FIG. 4.6: Time-height cross-sections of the (a) horizontal, (b) vertical, and (c) combined (horizontal + vertical) components of the anomalous time rate of change of drying for the meridionally-averaged (10°S-5°N) framework.....	60
FIG. 4.7: Schematic diagram illustrating cloud system scale differences.....	62
FIG. 4.8: November-February (NDJF) climatological mean (1984-2001) latitude-height cross-sections of the apparent heat source (Q_1 ; a) and apparent moisture sink (Q_2 ; b) averaged from 150°E-160°E (West Pacific warm pool region).....	64
FIG. 4.9: Time-height cross-sections of (a) Q_1' , (b) T' , (c) Q_2' , and (d) q' for the meridionally-averaged (10°S-5°N) framework.....	66
FIG. 4.10: Vertical profiles of heating ($Q_1'T'$; red line) and moistening ($-Q_2'q'$, green line) averaged over the entire MJO composite event based on the individual gridpoint framework.....	69
FIG. 4.11: Vertical profiles of heating ($Q_1'T'$; top row) and moistening ($-Q_2'q'$; bottom row) averaged over the entire MJO composite event based on the individual gridpoint framework.....	71
FIG. 4.12 (a-s): Time-height cross-sections and timeseries for a host of dynamic and thermodynamic variables for the composite MJO event based on the individual gridpoint framework.....	74-78
FIG. 4.13: Composite map sequences of (a) TRMM total rainfall and 850 hPa wind anomalies, (b) OLR and 200 hPa wind anomalies, (c) $q_{600\text{hPa}}$ and 600 hPa wind anomalies, and (d) $\omega_{600\text{hPa}}$ and 600 hPa wind anomalies for the individual gridpoint framework.....	82-84
FIG. 4.14: Map sequences of (a) TRMM total rainfall and 850 hPa wind	

anomalies, (b) OLR and 200 hPa wind anomalies, (c) $q_{775\text{hPa}}$ and 775 hPa wind anomalies, (d) $\omega_{775\text{hPa}}$ and 775 hPa wind anomalies, (e) SLHF and 1000 hPa wind anomalies, and (f) precipitable water and 850 hPa wind anomalies for the single event of 21 October 1998 based on the individual gridpoint framework.....	87-91
FIG. 4.15: Time-height schematic diagram of the discharge-recharge mechanism.....	98
FIG. 4.16: Composite timeseries of anomalous dry static stability for the meridionally-averaged (10°S-5°N) framework.....	99
FIG. 4.17: Dry static stability for the single event of 21 October 1998 based on the individual gridpoint framework.....	100
FIG. 4.18: Statistical significance shading of the time-height cross-sections of (a) Q_1' and (b) Q_2' for the individual gridpoint framework, as well as (c) the zonal component of anomalous time rate of change of specific humidity for the meridionally-averaged case.....	102
FIG. 4.19: Latitude-height cross-section of GLAS-derived cloud-top heights totaled between 16 October-19 November, 2003, for the longitude range 80°E-90°E.....	108
FIG. 4.20: A single track segment of GLAS cloud data for 20 October 2003 as represented in a time-height cross-section.....	110
FIG. 4.21: MODIS-derived daily-averaged 1°x1° cloud-top pressure (CTP) values corresponding to a time and space location similar to that of the GLAS cross-section in Figure 4.20.....	110
FIG. A.1: Illustration detailing the anomaly calculations used to construct MJO	

composite cross-sections..... 116

Chapter 1

Introduction

The tropical atmosphere is a complex realm of many wave types. One such wave, the Madden-Julian Oscillation [MJO; also called the Intraseasonal Oscillation (ISO)], dominates atmospheric variability on intraseasonal (10-100 days) timescales. The MJO is an eastward-propagating wave most active during the boreal winter months in the Indian and West Pacific Ocean regions. This phenomenon involves multi-scale cloud and precipitation processes and is manifested in numerous atmospheric variables. The combination of a poor representation of this tropical wave in most current general circulation models (GCMs) and a lack of comprehensive understanding of several of its mechanisms highlights the need for continued research of the MJO. This thesis focuses on the “birth” (wet phase approach) and “death” (wet phase departure) of the MJO and their related precipitation, convective, and advective processes. It is our hope that this study and others like it will contribute toward a better conceptualization of the MJO, its physical mechanisms, and its accurate depiction in GCMs.

The Tropics, which encompass roughly half the surface area of the Earth, are the focal point of MJO wave activity and, in addition, play a vital role in global atmospheric dynamics and circulation patterns. Although the equatorial band receives far more annual insolation than the higher latitudes, only small horizontal variations in temperature and pressure exist in these low-latitude regions. Here, latent heating is of primary importance. This heating drives multi-scale circulation systems and is balanced by adiabatic and radiative cooling. Within the Tropics, large-scale subsidence is interrupted by isolated but intense upward motion. Eastward- and westward-propagating weather systems are commonly

observed. These convective systems, including the MJO, are the mechanisms by which the impacts of anomalous, localized heating are communicated through the tropical atmosphere.

Perhaps the most important pioneering study of equatorial waves was conducted by Matsuno (1966), who created dispersion curves in wavenumber-frequency space of theoretical tropical wave types, some of which had not yet been observed. Although numerous equatorial waves were described in Matsuno's diagram, the MJO was absent due to its lack of linear mathematical roots (it was later found to resemble a coupled Kelvin-Rossby mode). It was not until the early 1970s that the MJO was first noted in observational data. Madden and Julian (1971, 1972; see also Madden and Julian, 1994) discovered the oscillation using cross-spectral analysis of lower- and upper-tropospheric zonal winds and sea-level pressure. Since that time, a growing number of studies have rapidly advanced our understanding of the MJO. In particular, the general physical characteristics and lifecycle of the wave as seen in a number of atmospheric variables have been researched [Rui and Wang (1989), Hendon and Salby (1994), Zhang and Hendon (1997), DeMott and Rutledge (1998), Maloney and Hartmann (1998), Yanai et al. (2000), Meyers and Waliser (2003)]. The convective and stratiform cloud and precipitation processes during the MJO wet phase have also been investigated [Houze (1982), Lin and Johnson (1996a,b), Mapes (2000), Kikuchi and Takayabu (2004)]. Several other studies have focused on the regional environment within which wave initiation occurs in the Indian Ocean and what related mechanisms are most important [Bladé and Hartmann (1993), Hu and Randall (1994), Kemball-Cook and Weare (2001)]. Straub and Kiladis (2003) examined the structure of convectively-coupled Kelvin waves, a type of wave that closely resembles the MJO. The importance of ocean-atmosphere interactions in conjunction with the MJO—including the wind-induced surface heat exchange (WISHE) mechanism—has been the focus of several papers over the past two decades [Emanuel (1987), Neelin et al. (1987); Stephens et al. (2004)]. A number of studies have also reported on the possibility of connections between the MJO and the

extratropics in both pre- and post-convective stages [e.g., Hsu et al. (1990), Bladé and Hartmann (1993)]. Spectral analysis and filtering techniques involving a decomposition of atmospheric variables into wavenumber-frequency space have been implemented in a few studies to effectively isolate and analyze the MJO signal [Wheeler and Kiladis (1999), Yang et al. (2003), Cho et al. (2004)]. Recently, vast improvements in the depiction of MJO-like waves in atmospheric models have been achieved [Grabowski (2003), Grabowski and Moncrieff (2005, in press), Biello and Majda (2005, submitted), Grabowski (2005, submitted)].

The research studies listed above have broadened the knowledge base of many complex features of the MJO. As previously noted, the MJO dominates intraseasonal variability in the equatorial atmosphere. We now know that it is a first baroclinic mode, equatorially-trapped, convectively-coupled, zonal wavenumber 1-2 disturbance. This broadband oscillation has a period of approximately 20-100 days, is interdecadally robust, and is most intense during the boreal winter. Numerous variables—including zonal and vertical winds, outgoing longwave radiation (OLR), geopotential, water vapor mixing ratio, temperature, and precipitation—reflect variability associated with the MJO. In terms of the general lifecycle, the wave disturbance originates in the West Indian Ocean (WIO), propagates eastward at 3-8 m/s into the West Pacific Ocean (WPO), and dissipates soon after the International Date Line (180°). Observational evidence exists of a weaker but detectable signal (mostly in upper-tropospheric winds) which travels across the Western Hemisphere at 12-15 m/s and returns to the WIO [see Madden and Julian (1994) for review]. The dry phase of the MJO is characterized by weak surface easterly wind anomalies and ocean-atmosphere fluxes, lightly- or non-precipitating shallow cumuli, and strong surface absorption of insolation (see Figure 1.1). As the main area of convection approaches from the west, the continued heating and moistening of the lower troposphere by shallow cumuli destabilize the atmosphere. The wet phase arrives with intense, deep convection flanked by

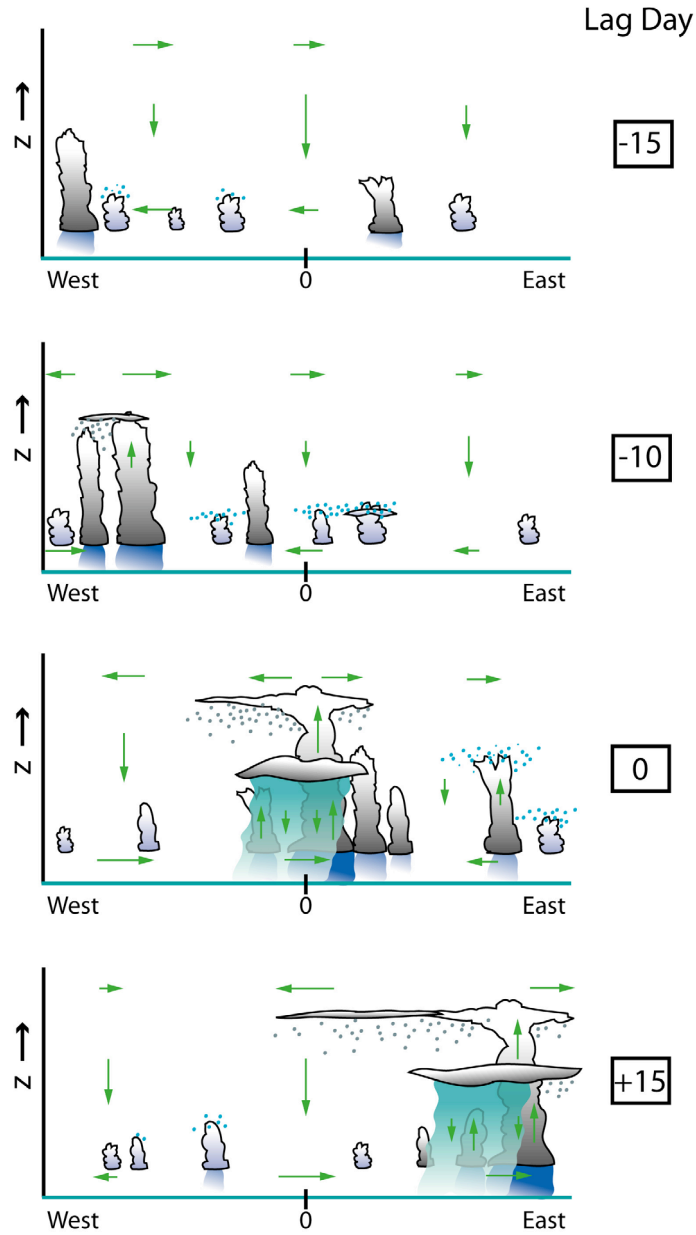


Figure 1.1: Longitude-height schematic diagram of MJO wave propagation. The aqua horizontal axis represents the ocean or land surface, and the "0" mark is the location of interest. Lag days relative to the maximum rainfall at the location of interest are indicated to the right of each panel. Green arrows represent wind anomalies associated with the oscillation. Both convective (large vertical scales) and stratiform (large horizontal scales) are depicted. Light blue dots above shallower convective clouds represent moistening via detrainment, while gray dots below stratiform cloud types represent ice crystal fall-out and moistening. Convective precipitation is indicated by darker-blue rain shafts, and stratiform precipitation areas are light-blue and slightly transparent. Strong subsidence, a cool and dry free troposphere (not shown), and suppressed deep convection highlight day -15 (dry phase). Enhanced shallow convection and low-level moistening commence near day -10 as deep convection approaches from the west (these features signal the "birth" of the MJO wet phase). Vigorous convection and intense rainfall evolve into a steadier stratiform rainfall near day 0 as wind anomalies abruptly become westerly. Competing updraft and downdraft processes occur at this time. Rain intensity diminishes fairly rapidly after day 0, signaling the "death" of the wet phase). Westerly wind anomalies culminate near days +10 to +15 as subsidence and tropospheric drying return. Cirrus clouds may linger well after the wet phase has ended due to moist advection by upper-level easterly wind anomalies.

moderate surface easterlies to the east and strong surface westerlies to the west. After a few days, intense precipitation dissipates as drier westerly winds develop. About two weeks after the main convection has passed, lower-tropospheric winds, subsidence, and surface fluxes are strongest and deep convection is suppressed. Collectively, the dynamical characteristics that describe the MJO have both similarities and differences with theoretical Kelvin waves. The two wave types share features such as eastward propagation, approximate geostrophic balance in the meridional direction, and primarily zonal wind anomalies. Concerning differences, the MJO has a periodicity and phase speed slower than that of a *dry* Kelvin wave, and upper- and lower-level MJO wind fields do not match those of a *dry* Kelvin wave.

Several theories that have been proposed to explain the physical mechanisms of the MJO. In the theory of conditional instability of the second kind as applied to tropical waves (wave-CISK), instability occurs as a result of “cooperation” between localized convective heating and its environmental large-scale circulation [e.g., Hayashi (1970), Lindzen (1974)]. Once a disturbance is initiated, large-scale, low-level moisture convergence produced by the wave tends to promote a favorable environment for convection. At some point, convection is triggered and its associated latent heat release helps drive a secondary circulation, causing additional large-scale convergence. In this way, the wave-CISK disturbance is maintained by the mutual feedback of cumulus heating and larger-scale circulations. One drawback of the wave-CISK concept is that it produces faster phase speeds and significantly shallower vertical structure as compared to the observed MJO. More intricate versions of the wave-CISK model (e.g., Chang, 1977) produce results that resemble the observed MJO wave, but some of the assumptions and specifications in these newer versions are not entirely consistent with observations.

A second theory is based on the WISHE mechanism [Emanuel (1987), Neelin et al. (1987)] and involves an instability that arises through the interaction of surface heat and

moisture fluxes and large-scale wave dynamics. This theory states that eastward-propagating convective systems are maintained by increased inflow of low-level moisture, a result of surface evaporation from the ocean by anomalous easterlies. Thus, the WISHE feedback requires a background low-level easterly wind flow, but climatological winds across much of the Indian and West Pacific Oceans are westerly (see Figure 3.2). Additionally and as we will see in the coming chapters, the strongest surface fluxes are often found to the *west* of the disturbance; however, WISHE may play a role in the initiation of MJO waves in the West Indian Ocean [e.g., Grabowski and Moncrieff, 2005 (in press)].

The discharge-recharge mechanism (e.g., Yamagata and Hayashi (1984); Bladé and Hartmann (1993), Hu and Randall (1994)], a third theory used to describe the MJO, involves a gradual remoistening of the troposphere during the dry phase in preparation for the next convective triggering. According to this theory, the lower and middle troposphere are exhausted of moisture following the MJO wet phase. Shallow cumuli then redevelop and low-level moist static energy gradually increases. Strong vertical moisture transport is accomplished by growing cumuli. At some point, a critical level of instability is achieved and the main convective event is triggered, once again exhausting the lower levels of moisture. This cycle may be related to MJO periodicity in that wave growth is restricted by the efficiency and speed of remoistening and generation of instability. Because many aspects of discharge-recharge theory are noted in the results of this study (see Section 4.2.4), we feel that this mechanism plays an important role in the MJO lifecycle.

The fourth, recently-proposed mechanism is that of stratiform instability, an instability generated by a positive correlation between a second-mode temperature profile and second-mode stratiform heating structure [Houze (1997), Mapes (2000), Majda and Shefter (2001)]. During the stage of a wave cycle in which the lower troposphere is anomalously cool, for example, this vertical temperature structure would act to destabilize the lower layers [negative lower- to mid-tropospheric lapse rate, reduced convective inhibition

energy (CIN); see Mapes (2000)]. Deep convection would then be more apt to develop, with attendant stratiform heating developing at lag. Stratiform heating tends to warm the upper troposphere and cool the middle to lower troposphere, and thus it is in phase with the original vertical temperature structure. This in-phase relationship, a positive correlation of heating and temperature anomaly, generates available potential energy and wave growth and will be discussed in detail in Section 4.2.1. Although this mechanism may be a viable explanation for certain aspects of the MJO, Straub and Kiladis (2003) point out distinct differences between observations and waves modeled using stratiform instability, particularly in the result that upper-level warm anomalies *lead* convective heating.

Because the MJO explains much of the intraseasonal variability in the Tropics and has ties to the extratropics, accurately diagnosing and modeling this phenomenon is of critical importance for weather and climate studies. Currently, no widely-accepted theory exists that can fully explain the MJO. A comprehensive understanding of several of its dynamic and thermodynamic aspects, and how these processes are to be parameterized in atmospheric models, remains elusive. In addition, enhanced satellite datasets with increasingly-finer spatial and temporal resolution are now becoming available. The advent and success of the TRMM satellite program have provided a unique research opportunity. To our knowledge, few if any previous studies have presented or commented on a composite MJO event based on TRMM rainfall; rather, most research endeavors of the past have based composite lifecycles on zonal winds, OLR, or relative humidity [e.g., Weickmann et al. (1985); Hendon and Salby (1994); Maloney and Hartmann (1998); Meyers and Waliser (2003)].

The purpose of this study is to explore certain features of the MJO—particularly the approach and departure of the wet phase—using analyses of both single events and event composites based on hydrological activity. In this report, we focus on the cloud and advective processes, as gathered from reanalysis datasets, that are associated with the evolving

MJO wave. A novel aspect of this study is that it deals with the immediate and delayed drying processes following the MJO wet phase. This facet of the MJO lifecycle has not been analyzed explicitly in previous observational composite studies; rather, most studies [e.g, Hendon and Salby (1994); Maloney and Hartmann (1998)] have implemented smoothed or filtered data fields to highlight the delayed drying associated with Rossby wave circulations. It is our hope that the results of this thesis contribute toward a better conceptualization of the MJO and ultimately a more accurate depiction of intraseasonal variability in atmospheric models.

The various data sources and statistical methods employed in this paper are outlined in Chapter 2. In Chapter 3, composite MJO time-height cross-sections of the fundamental atmospheric and oceanic variables (\mathbf{v} , T , q , SST, etc.) are presented and analyzed. Our primary results, including a detailed discussion of the convective and advective processes which highlight the various stages of the MJO, are featured in Chapter 4, followed by concluding remarks in Chapter 5.

Chapter 2

Data and Methodology

The following is a discussion of the various data sources used in this study, and the statistical techniques implemented to organize those data.

2.1 Data Sources

One challenge facing those who study the Madden-Julian Oscillation is the lack of observations in the geographic region where the disturbance is most active: the tropical ocean. Current, reliable, surface-based observations are limited to the Indonesian Maritime Continent and a small number of islands within the Indian Ocean. The evolution and enhancement of geosynchronous and polar-orbiting satellite systems have provided a clearer picture of the atmosphere and ocean in this data-sparse area. In 1997, the Tropical Rainfall Measuring Mission (TRMM) began collecting atmospheric data via a space-borne instrument package including a precipitation radar, microwave imager, and visible and infrared scanner. Since its inception, TRMM has been quite successful at providing quality datasets of moisture, clouds, and precipitation over the remote equatorial ocean areas. Nonetheless, the accurate monitoring of many atmospheric fields such as surface winds and tropospheric temperatures in the tropical Indian and Pacific Oceans remains a challenge. To partially overcome this problem, hybrid techniques which combine surface-based observations, satellite data, data assimilation procedures, and model output have been implemented to create reanalysis datasets. These datasets, however, are limited by the physics, parameterizations, and resolutions within the model.

The datasets that are utilized in deriving the results of this paper are drawn from four sources: TRMM, ERA40 (European Centre for Medium-Range Weather Forecasts 40-year reanalysis), MODIS-Terra (Moderate Resolution Imaging Spectroradiometer - Terra satellite), and GLAS (Geoscience Laser Altimeter System). We present specifications of these data sources in Table 2.1, and a graphical representation of the date ranges of the source data in Figure 2.1.

Table 2.1. Specifications of the datasets used in this analysis. For some variables listed, such as *Horizontal domain*, the values indicated may only be a subset of the entire dataset (e.g., the full ERA40 source has global coverage). The ERA40 variables are zonal (u) and meridional (v) wind, vertical velocity (ω), temperature (T), specific humidity (q), mean sea-level pressure (MSLP), surface latent heat flux (SLHF), sea-surface temperature (SST), and solar radiation absorbed at the surface (SSA).

	<i>TRMM (3B42)</i>	<i>ERA40</i>	<i>MODIS</i>	<i>GLAS</i>
Origin/Platform	Satellite (TRMM)	Observations and model forecasts	Satellite (Terra)	Satellite (ICESat)
Horizontal resolution	1° x 1°	2.5° x 2.5°	1° x 1°	Swath segment 70 m wide, 28 km long
Horizontal domain	180°W-180°E, 30°S-30°N	180°W-180°E, 30°S-30°N	180°W-180°E, 30°S-30°N	Global
Vertical levels	Surface	1000, 925, 850, 775, 700, 600, 500, 400, 300, 250, 200 hPa	Single level	76.8 m resolution
Temporal resolution	Daily-averaged	Daily-averaged	Daily-averaged	Continuous
Temporal domain	1 Jan 98 - 28 Feb 04	1 Jan 97 - 31 May 02	1 Jan 98 - 28 Feb 04	16 Oct 03 - 18 Nov 03
Gridded/Orbital	Gridded	Gridded	Gridded	Orbital
Variables	Total precipitation	$u, v, \omega, T, q,$ MSLP, SLHF, SST, SSA	Cloud-top temperature (CTT), cloud-top pressure (CTP)	Cloud-top height (CTH), cloud layer thickness
	<i>TRMM(3B42)</i>	<i>ERA40</i>	<i>MODIS</i>	<i>GLAS</i>

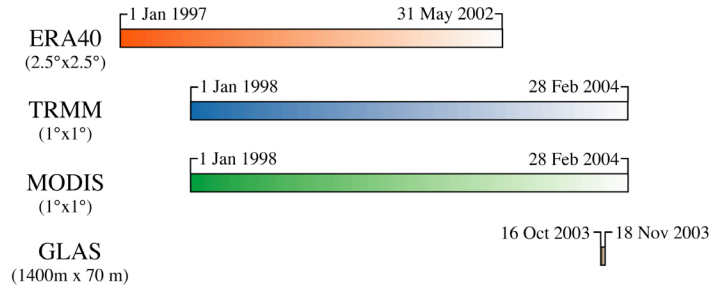


Figure 2.1: Schematic representation of the source data date ranges in this analysis.

Our primary source for precipitation estimates during the period of analysis is the TRMM satellite. The TRMM data product 3B42 (V5) is derived from a number of space-borne instruments (Kummerow et al., 2000). The radar radiance fields detected by the precipitation radar (PR), passive microwave imager (TMI), and visible and infrared spectrometer (VIRS) onboard TRMM are combined to generate a preliminary rainfall estimate. This TRMM estimate is then implemented to adjust independent precipitation values derived from Geostationary Operational Environmental Satellite (GOES) infrared observations, finally yielding the 3B42 product.

The advent of the TRMM satellite program provides a unique research opportunity. Never before has the detection of tropical precipitation of such high spatial and temporal resolution been possible (Kummerow et al., 2000). Prior to the inception of TRMM, low-latitude rainfall estimates varied greatly between the large number of diverse satellite sensors used to monitor such parameters. The accuracy of these pre-TRMM estimates, including reanalysis products (e.g., see Figure 3.1), remains very uncertain (Kummerow et al., 2000). TRMM’s precipitation radar, the first radar instrument designed to operate onboard a satellite, provides unparalleled rainfall resolution and accuracy. This, combined with improved TMI and VIRS instrumentation as well as a sufficiently long data record (7+ years), offers the opportunity to study the MJO based on accurate, high-resolution rainfall data. Although our results based on dynamical fields are entirely independent of the

TRMM data products, we are reassured by how well these dynamical fields match up with TRMM's hydrological patterns (see Chapters 3 and 4).

In this report, we employ ERA40 data to describe the dynamic and thermodynamic state of the tropospheric depth during our period of analysis. The ERA40 dataset is constructed from techniques which combine observations, data assimilation, and model forecasts. The premise behind the reanalysis procedure is to allow information of the atmospheric state to be communicated from areas of dense observational coverage to areas of sparse observational coverage (Simmons et al., 2000). Output from a model forecast is first meshed with observations to create an "analysis," the analysis is then adjusted for small errors (assimilation), this adjusted analysis initializes the next model forecast, and the process continues in a cyclic fashion. Although the reanalysis method minimizes missing data points, such datasets are limited by the physics, parameterizations, and resolutions within the forecast model.

A host of hydrological, radiational, and chemical parameters are found in the MODIS-Terra MOD08 D3 dataset, but our analysis will utilize only cloud-top pressure (CTP) and temperature (CTT) data. A CO₂ slicing method centered around the 15- μ m band is implemented in calculating CTP. This method takes advantage of differing partial absorption IR bands within the broad 15- μ m CO₂ spectral region. Each band is sensitive to a different atmospheric level; high clouds will affect all bands but low clouds might not be seen by the high-absorption bands. Upwelling IR radiances for two nearby spectral bands are measured simultaneously from the Earth-atmosphere system. By measuring the ratios of the differences of these retrievals and assuming that the emission and absorption of the two neighboring spectral bands are identical, CTP can be determined (Menzel et al., 1982). The CO₂ slicing method performs best at and above the 700 hPa level (~3 km). The accuracy of this technique is highest where the cloud signal (clear sky – measured radiance) is greatest. In the case of low clouds, a special procedure is employed: the 11- μ m brightness

temperature (T_b) is used to diagnose CTT, assuming the cloud is optically thick, and then a CTP is assigned by comparing the measured T_b to a temperature profile from the National Centers for Environmental Prediction (NCEP) Global Data Assimilation System (GDAS). Low clouds that are not optically thick likely have a shallow bias due to transferred radiances from lower (warmer) atmospheric levels. GDAS (1°, 6 hr resolution) is also the source of required clear-sky radiances that are compared to the measured radiances from Terra. Once a CTP value is determined, a CTT is computed from the GDAS temperature profile. The CO₂ slicing technique allows for multiple cloud layers to be detected. When this occurs, the most representative CTP value is computed using an equation relating the observed IR radiances and a radiative transfer model (see Eq [1] in Menzel et al., 1982). This optimum CTP value occurs when the difference between the observed and modeled radiance quotients is minimized. While the accuracy of CTPs in the context of multiple cloud layers is difficult to characterize, CTP values for non-overlapping clouds above 700 hPa are accurate to within 50 hPa (Platnick et al, 2003; King et al., 2003).

We employ cloud data taken from the GLAS instrument as a complementary, independent, but limited alternative to the MODIS cloud-top data. Although the GLAS cloud information is at a high spatial and temporal resolution within a particular orbital swath, the large gaps void of data between swaths and the limited temporal range restrict its usage. Because no well-defined MJO convective episodes occurred during the GLAS data acquisition period (see Tables 2.1, 3.2, and 3.3), the lidar data is implemented for a simple comparison with MODIS estimates in the context of general tropical cloud features. The lidar is onboard NASA's Ice, Cloud, and land Elevation Satellite (ICESat) and was launched in January of 2003. Repetitive laser pulses at 40 Hz and 532 nm (and 1064 nm should the 532 nm signal become saturated) generate a radiance backscatter profile. The backscatter profiles are averaged over 4 s to improve the signal-to-noise ratio. Two different algo-

rithms applied to each averaged profile allow the determination of up to 10 cloud/aerosol layers, with discrete layer top and bottom heights (Palm et al., 2002).

2.2 Methodology

The tropical atmosphere is complex, composed of a symphony of wave types. These oscillations transport energy (among other things) horizontally and vertically, operate on a range of spatial and temporal scales, and interact with one another. Some waves are “well-behaved” and follow rules outlined by simple linear theory (e.g., Matsuno, 1966). Others, including the MJO, diverge from this basic model due to coupled processes that alter certain aspects of the wave, such as propagation speed. Despite these complexities, we can decompose the raw dataset into its fundamental zonal wavenumber and frequency components, thereby allowing the MJO signal to be separated from other wave types. The act of extracting the MJO signal, however, has some negative consequences, including a spatial and temporal smoothing of the field in question. This degradation of resolution potentially masks many of the small-scale features that play critical roles in the MJO lifecycle. In the discussion that follows, we explain how such problems are alleviated, the usefulness of spectral analysis, and the intricacies of generating an MJO composite picture.

2.2.1 General statistical methods

A number of statistical techniques are applied to the data. To isolate features that are related to the MJO, we spectrally analyze and filter several variables in zonal wavenumber and frequency space. Distinct convective episodes associated with the MJO are composited based on maximum daily TRMM rainfall. Further statistical parameters, such as covariances, are derived from these composites.

Our analysis begins with a space-time spectral analysis of TRMM rainfall. We closely follow the procedures outlined in Wheeler and Kiladis (1999, hereafter WK99). The conver-

sion of atmospheric data from physical to spectral space highlights wave characteristics within the dataset. Wave features not immediately recognizable in physical space often emerge clearly in a spectral power diagram, as is the case with equatorial rainfall. A spectral categorization of wave types, each associated with distinct dynamic and thermodynamic mechanisms, is possible based on differences in frequency, wavenumber, and direction of propagation.

Concerning the spectral analysis procedure, we first remove the mean and first three harmonics of the composite annual cycle. The resulting anomaly field (T) is decomposed into symmetric (S) and antisymmetric (A) components about the Equator, where $S(\phi) = [T(\phi) + T(-\phi)]/2$, $A(\phi) = [T(\phi) - T(-\phi)]/2$, and ϕ is latitude. The data is then temporally sliced into successive 96-day segments with an overlap of 60 days, the mean and linear trend of each segment are removed, and the ends of each segment are tapered using a Hanning window. The choice of segment length eliminates wave features with periods greater than 96 days while effectively preserving those on synoptic and intraseasonal timescales. Application of the Hanning window limits spectral “leakage,” and the 60-day overlap prevents loss of information near the ends of the tapered time segments. At this point, the data are structured in an array of dimensions (longitude, latitude, segment time, segment number), where *segment time* extends from 1 to 96. We perform complex fast Fourier transforms (FFTs) on the *longitude* dimension to obtain real and imaginary coefficients, and follow this by performing complex FFTs on the *segment time* dimension. The power values are then calculated for each Fourier coefficient pair. Averaging together all segments eliminates the segment number dimension, and summing the power values from 10°S-5°N completes the conversion of data from physical to spectral space (zonal wavenumber-frequency domain). A red noise background spectrum is computed by averaging the symmetric and antisymmetric spectra together, and then strongly smoothing in both wavenumber and frequency. The spectral diagram (Figure 3.7) presented in Section 3.1 is

produced by dividing the symmetric (or antisymmetric) power values by their associated red noise values. As previously mentioned, further details of this spectral analysis are outlined in WK99.

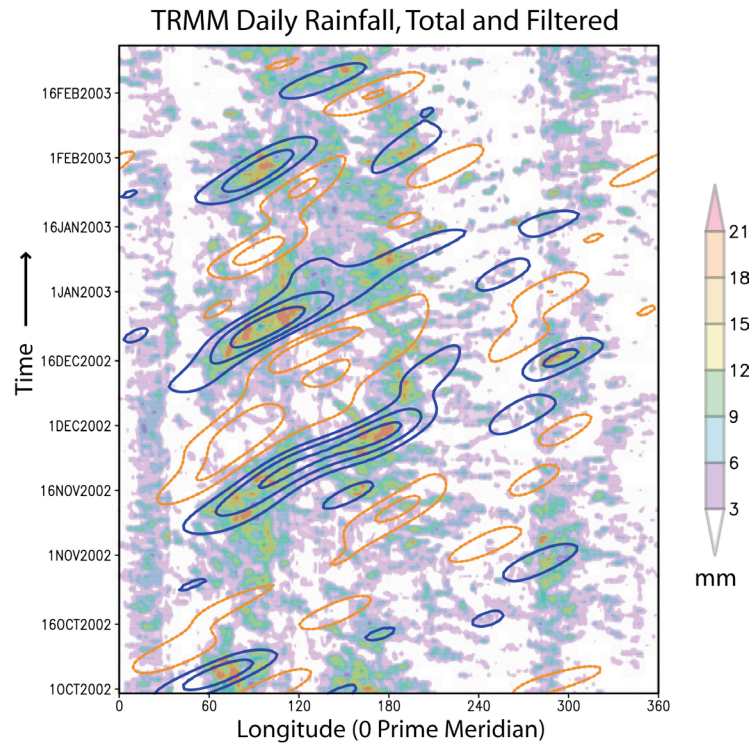


Figure 2.2: Example of the application of spectral filtering on a raw data field. Light shading indicates unfiltered rainfall accumulation from the TRMM dataset. Blue (wet) and orange (dry) contours represent rain anomalies derived from a spectral filter (the MJO spectral region: wavenumbers 1-5, periods 10-100 days). Note that time increases upwards.

In addition to the basic spectral analysis discussed above, we also implement spectral filtering methods to extract particular wave features from the raw data. Figure 2.2 is a superposition of the filtered MJO signal (contours) on the unfiltered TRMM precipitation (shaded) and is shown as an illustration of the filtering process. Despite the high degree of spatial and temporal variability of equatorial rainfall, we find that the larger-scale rain structures are captured reasonably well by spectral filtering over the periods and wavenumbers of interest, especially in a meridionally-averaged sense. The filtering procedure is similar to the spectral analysis method, with the key difference that the data are not tempo-

rally segmented or decomposed into symmetric and antisymmetric parts. Segmenting the data would prohibit the physical timeseries from being recovered after spectral filtering, and no decomposition is undertaken because, according to Figure 3.7, the MJO has both symmetric and antisymmetric components. The mean and first three harmonics of the composite annual cycle are subtracted from the full data record. The first and last 10% of the timeseries are also tapered to mitigate spectral leakage. These anomalies are next transformed into zonal wavenumber-frequency space via complex FFTs. With guidance from Figure 3.7, we isolate signals characterized by eastward-propagating waves of wavenumber 1-5 and period 20-100 days. Although we primarily use the 20-100 day period filter, parallel analysis is also undertaken using a 10-100 day filter (see Section 3.2 for a discussion on sensitivity testing). For comparison, WK99 use wavenumbers 1-5 and periods 30-96 days, and Kemball-Cook and Weare (2001, hereafter K-CW01) effectively retain wavenumbers 1-6 and periods 10-100 days as spectral thresholds appropriate for MJO filtering. Numerous studies report MJO periods in the range 20-80 days (Madden and Julian, 1994). To obtain the MJO signal in physical space, all Fourier coefficients outside of the wavenumber-frequency thresholds are set to zero, and an inverse FFT is performed first in time and then in longitude (opposite sequence to “forward” FFT). The resulting longitude-latitude timeseries represents the portion of the total signal associated with MJO-like variability in physical units.

Versions of this MJO-filtered dataset are implemented in (a) distinguishing individual convective events associated with the MJO phenomenon and (b) the construction of a composite MJO event. We analyze the convective events in two frameworks; the first involves a timeseries of meridionally-averaged (10°S - 5°N) rainfall anomalies, and the second involves a timeseries of an individual gridpoint.

2.2.2 Meridionally-averaged framework

In the first framework, an area-averaged mean (\bar{x}) and standard deviation ($\bar{\sigma}$) of the MJO-filtered TRMM precipitation anomalies are calculated, where

$$\bar{x} = \frac{1}{N} \sum_{i,j} \left(\frac{1}{T} \sum_t x_{i,j,t} \right) \quad (2.1)$$

and

$$\bar{\sigma} = \frac{1}{N} \sum_{i,j} \left[\sqrt{\frac{1}{T-1} \sum_t (x_{i,j,t} - \bar{x}_{i,j})^2} \right], \quad (2.2)$$

the i,j,t are longitude, latitude, and time indices, respectively; T is the total number of time points; and N is the total number of gridboxes in the defined domain (0-360°, 10°S-10°N). All data points within the defined area are next standardized using

$$x_{i,j,t} = \frac{x_{i,j,t} - \bar{x}}{\bar{\sigma}}. \quad (2.3)$$

Area-averaging x and σ serves to slightly clarify rainfall events in the highly-variable tropical Indian and West Pacific Oceans while tempering signals not associated with the MJO outside this region. Utilizing these “standardized” rainfall anomalies, we construct Hovmöller diagrams by averaging the data from 10°S-5°N. These meridional boundaries are chosen to capture the maximum MJO variance, which occurs during the boreal winter, and are consistent with the findings of WK99 (their Figure 7c).

Individual convective events in the first, meridionally-averaged framework are defined according to a stringent set of criteria, similar in nature to the constraints imposed by Rui and Wang (1990). To qualify as an MJO convective episode, the standardized, filtered rainfall anomaly (R) in the Hovmöller diagram must exceed 1σ in strength and 20° in longitude throughout its lifetime, which must be a minimum of 15 days. During its lifetime, R must also exceed 1.5σ at some point. The entire event must occur in the Indian or

West Pacific Ocean region (50°E-140°W) during the boreal non-summer months (15 September - 31 May). The 17 MJO convective events defined under these constraints are visually verified by comparison with Hovmöller diagrams of raw, unfiltered TRMM rainfall.

A goal of this paper is the exploration of the atmospheric dynamics and cloud characteristics during the developmental and decaying stages of the MJO. Such processes of interest occur on spatial and temporal scales possibly eliminated during spectral filtering. In an attempt to return to these convective processes under the umbrella of the larger-scale MJO wave, we use the defined events based on R simply as a guide. For each event, the longitude and time of maximum R is recorded. This longitude and time become the centerpoint of a search area involving an identical Hovmöller diagram (summed 10°S-5°N) of *raw, unfiltered* TRMM rainfall. We devised the search area, which scans $\pm 15^\circ$ longitude and ± 5 days for the maximum meridionally-averaged rainfall value, because the date and location of the filtered precipitation maximum often was not collocated with its unfiltered counterpart. Following the search procedure, the resulting longitude and time of the unfiltered rainfall maximum defines the *base point* (lag day 0) of the event, upon which all other variables are centered. We analyze the timeseries of this base point, a meridional averaging at fixed longitude, from 30 days prior to rain maximum (lag -30) to 20 after rain maximum (lag +20). The rainfall maximum base point is implemented in the construction of time-height cross-sections of other variables (see Table 2.1) for all the MJO events defined. A compositing procedure averages together information from all events, for all non-precipitation variables. The final composites of these variables are converted into anomaly forms, defined as departures from the mean atmospheric state during an MJO convective event (see Appendix A for details). This anomaly definition guarantees a zero time mean for the event span, a useful feature for later statistical analyses.

2.2.3 Gridpoint-based framework

In addition to the meridionally-averaged framework, we also define events based on a single gridpoint using a similar procedure. The point-based analysis is conducted to identify any highly-localized features that may be masked by meridional averaging.

The point-based procedure involves extracting the MJO signal (wavenumber 1-5, periods 20-100 days) from the total rainfall anomalies in which the mean and first three harmonics of the composite annual cycle have been subtracted. The filtered data in physical space are then standardized (based on Equation 2.3) in time for each gridpoint, and local maxima in this dataset are tracked. To qualify as an MJO convective event, the local maxima must exceed 2σ for at least 10 consecutive days, must be located within the Indian or West Pacific Ocean region (50°E - 180° , 10°S - 5°N) at all times, and must occur between 15 September and 31 May. Most events satisfying these criteria travel more than 50° in longitude and eclipse 2.5σ in magnitude. As with the meridionally-averaged framework, the point-based method uses the filtered rain anomalies as a guide only. The longitude, latitude, and time of maximum event strength (when the local maximum of filtered rainfall anomalies is at largest magnitude) are recorded and become the centerpoint of the search area, which scans $\pm 15^{\circ}$ longitude, $\pm 2^{\circ}$ latitude, and ± 5 days in the raw, unfiltered dataset. Once rainfall maxima are located in the unfiltered dataset, procedures identical to those outlined in Section 2.2.2 are again implemented in constructing events and composites. The relatively small latitudinal search area is employed in order to restrict searching outside the 10°S - 5°N domain. We feel that the search area is appropriate considering the highly zonal nature of the MJO. In addition, extensive testing (see Section 3.2) suggests that the final composite cross-sections are not strongly sensitive to adjustments in the search area parameters.

Chapter 3

Results and Discussion I: Composites of Basic Variables

In this chapter, the climatology of the tropical atmosphere is first presented, followed by a discussion on sensitivity testing of the rainfall filtering techniques and MJO event selection criteria. In the final two sections, the behavior of basic atmospheric variables—wind, temperature, surface fluxes, etc.—for the meridionally-averaged and gridpoint-based frameworks (respectively) is reviewed.

3.1 What Do the Tropics Look Like?

The Madden-Julian Oscillation both contributes toward and is affected by the seasonal state of the atmosphere. Intraseasonal oscillations such as the MJO are superimposed onto a climatological state with influences from land-sea contrasts, interactions between the atmosphere and ocean, and large-scale circulation patterns such as the Hadley and Walker cells. In this section, we will explore the tropical climatological arena in which the MJO is active, discuss the characteristic profiles of the MJO background state as described in the previous chapter, and present a brief spectral assessment of significant equatorial wave types.

A comparison of TRMM and ERA40 total precipitation is displayed in Figure 3.1 for the period of record of each dataset (see Fig. 2.1). Despite the different temporal ranges, we assert that more than six years of data is sufficient to capture the general features of tropical precipitation. Even if the 1997-98 El Niño event is removed, the tropical rainfall patterns remain similar to those shown. Maps of ERA40 long-term (1984-2001) precipitation show

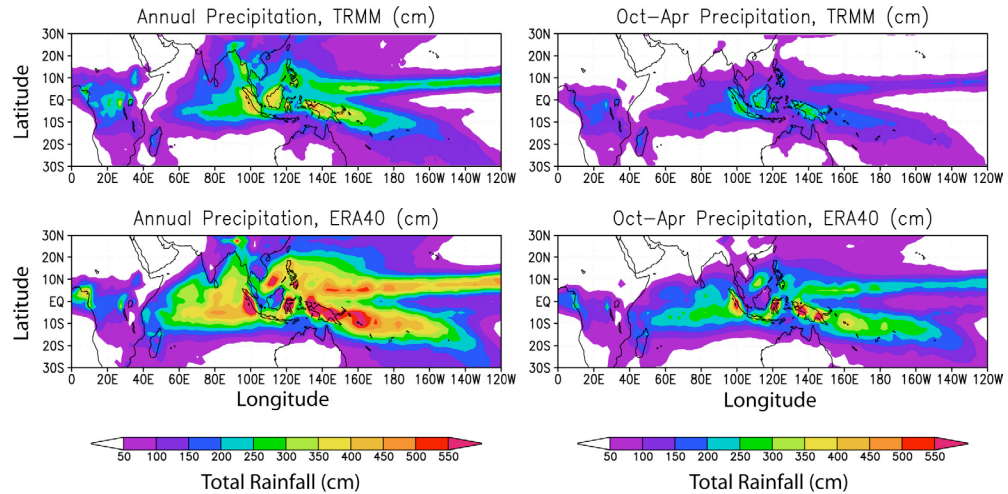


Figure 3.1: Annual (left) and October-April (right) accumulated total precipitation from TRMM (top) and ECMWF 40-yr Reanalysis (ERA40; bottom).

a strong similarity with the lower left panel of Fig. 3.1. Several physical features are clearly visible in the maps of annual rainfall (left column), most notably the enhanced precipitation of the Northern Hemispheric branch of the Intertropical Convergence Zone (ITCZ) as well as the South Pacific Convergence Zone (SPCZ). Maxima in rainfall are also observed over equatorial Africa and the Maritime Continent, likely the combined effect of large-scale dynamics and localized diurnal influences. During the boreal winter months (right column), much of the precipitation shifts south of the Equator following maximum solar heating. Examination of Fig. 3.1 suggests that the ERA40 dataset overestimates precipitation as seen from TRMM by 50-100 cm annually throughout much of the Tropics. Additional analyses (not shown) indicate that the precipitation from ERA40 also exhibits significantly higher temporal variance than that from TRMM. Despite these discrepancies, we feel strongly that many non-precipitation variables of the ERA40 dataset—including horizontal and vertical winds, temperature, moisture, pressure, and surface fluxes—are acceptable for use in an analysis of the MJO, especially in the context of meridional averaging and compositing. The ERA40 dataset represents a vast improvement to the previous 15-year reanalysis version, and provides an uninterrupted output data stream from a single, physically consistent model system (Troccoli and Kållberg, 2004). However, as a

precaution, any data deemed unphysical are removed from the final composite results (see Sections 3.3 and 3.4).

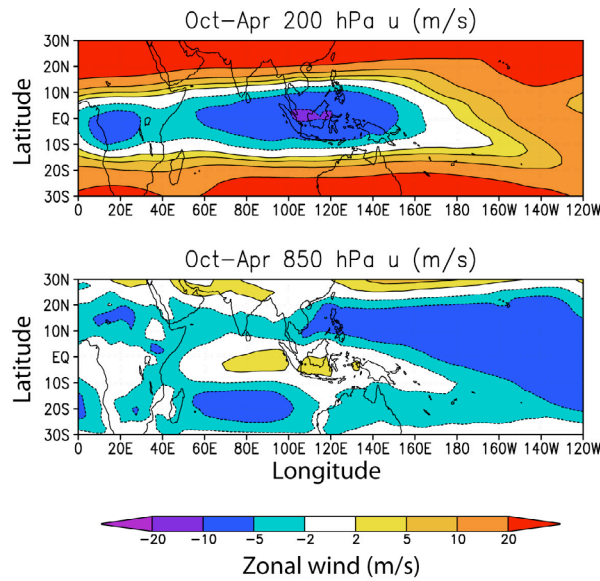


Figure 3.2: October-April mean zonal winds (u) at 200 hPa (top) and 850 hPa (bottom).

Upper- (200 hPa) and lower-level (850 hPa) zonal winds for the boreal winter months are presented in Figure 3.2. Upper-level easterly winds at speeds of 5-15 m/s dominate the equatorial Indian Ocean and Maritime Continent, with weak westerly flow in the tropical Central Pacific. A weaker and opposite wind regime is observed at 850 hPa, suggesting a pattern of low-level convergence and upper-level divergence, thus supporting a region of enhanced climatological convection over the West Pacific warm pool.

Climatological meridional winds (Figure 3.3), though weaker than \bar{u} , also have a distinguishable circulation pattern. Over the Indian Ocean and Maritime Continent, upper-level meridional winds are divergent. At 850 hPa, \bar{v} tends to be weakly convergent over these same areas.

Figure 3.4 is a display of vertical motions at two atmospheric levels, 400 hPa and 850 hPa. At 400 hPa (top panel), vertical velocity magnitudes in the Tropics tend to be largest

(Lin and Johnson, 1996a). This panel correlates nicely with the map of precipitation, with the northern and southern convergence zones clearly outlined. Over the Indian and West

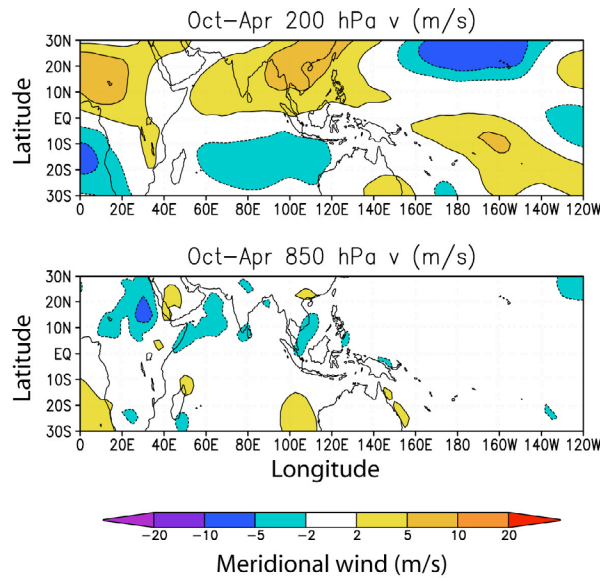


Figure 3.3: October-April mean meridional winds (v) at 200 hPa (top) and 850 hPa (bottom).

Pacific Oceans as well as the Maritime Continent, vertical motions at this pressure level tend to be upward, supporting convection on climatological scales. Locally, however, the convective updrafts are isolated and intense, breaking the weak but expansive environmental subsidence. At 850 hPa, very weak rising motions are observed over the Indian and West Pacific Oceans, with more intense upward velocities over the Maritime Continent, likely a result of land-surface heating. In light of this last observation, we minimized possible influences of land-ocean contrasts in our composite results (Sections 3.3 and 3.4) by discarding several individual events that occurred over land.

We present boreal winter OLR from the MJO region in Figure 3.5. The lowest OLR values—those associated with the highest, coldest cloud tops—extend from the Central Indian Ocean eastward to the West Pacific warm pool and match the pattern of maximum precipitation. As we will discuss in forthcoming sections, the omnipresence of cirrus

clouds in the equatorial band, as supported by Fig. 3.5, can sometimes make the detection of underlying shallow convective clouds quite difficult.

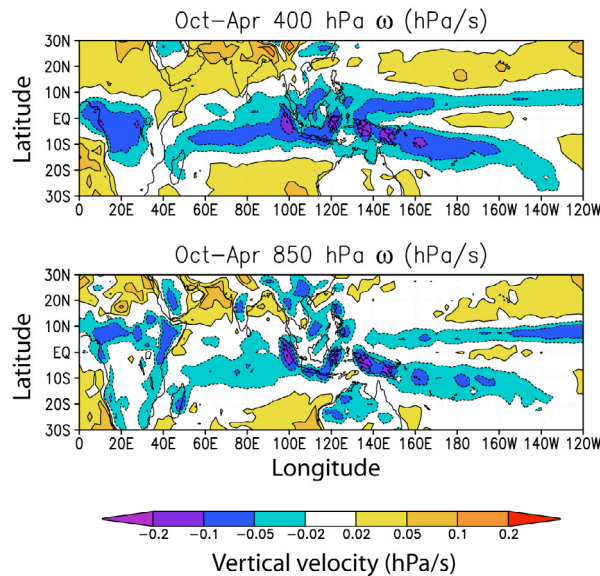


Figure 3.4 (above): October-April mean pressure velocities (ω) at 400 hPa (top; near level of expected maximum vertical motions in the Tropics) and 850 hPa (bottom).

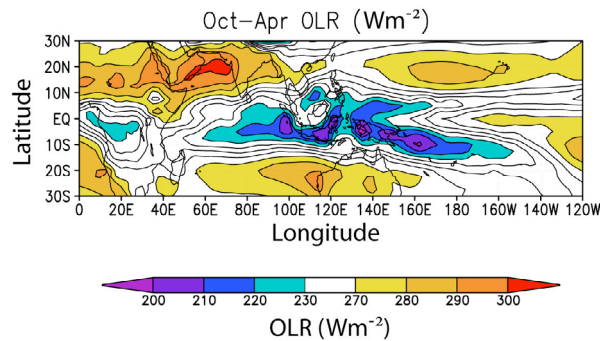


Figure 3.5: October-April mean outgoing longwave radiation (OLR). Lower values represent colder, higher clouds tops and areas of deeper convection.

The resulting time-height composite cross-sections that appear in Sections 3.3 and 3.4 are anomalies based on departures from the mean atmospheric state during times of high MJO wave activity (called the “MJO background state”). Details of this anomaly calculation procedure are outlined in Appendix A. Vertical profiles of the MJO background state and the corresponding 18-year climatology are displayed in Figure 3.6. Essentially, these are time-mean vertical profiles from the meridional band (10°S-5°N) associated with maxi-

imum unfiltered TRMM rainfall. The time mean encompasses all lag days from all events, including both the complete dry and wet phases of the MJO, and contains more than 550 data entries. Examination of Fig. 3.6 suggests that the atmospheric state during increased MJO wave activity is one of slightly enhanced vertical shear ($\frac{\partial u}{\partial z}$) as compared to climatology, stronger meridional and upward vertical motions, warmer temperatures (especially in the upper troposphere), and elevated moisture levels, particularly below 700 hPa. The increased vertical shear, which would act to weaken intense convection, is likely a result of the enhanced MJO activity rather than a cause of it. Lin and Johnson (1996b), in their study of convective processes during the Tropical Ocean Global Atmosphere (TOGA) Coupled Ocean Atmosphere Response Experiment (COARE) intensive observing period (IOP), noted that strong vertical wind shear accompanies westerly wind bursts, which occur during phases of suppressed convection 1-3 weeks following peaks in rainfall. Similarly, the increased winds and warmer upper-tropospheric temperatures appear to be a result of active MJO periods, as will be shown shortly. The elevated lower-tropospheric moisture levels arise from enhanced surface fluxes brought about by the wave approach and departure; these moisture increases simultaneously destabilize the environment, and therefore are likely both a cause and effect of the MJO.

A comparison between long-term climatology and the MJO background state for several variables appears in Table 3.1 for the meridionally-averaged framework. With the exception of $|v|$ (not shown) and mid- to upper-level T values, the differences between the MJO background and 18-year climatological states are small percentages of the cross-section anomalies to be presented shortly. Even if the anomaly computations were based on the departures from the 18-year climatology, in most cases the sign of the anomaly would not change and the physical structure of the departure would remain nearly the same. Generally, the mean difference between the MJO state and the long-term climatology is near or

less than one standard deviation of the differences based on each individual event (see caption for Table 3.1).

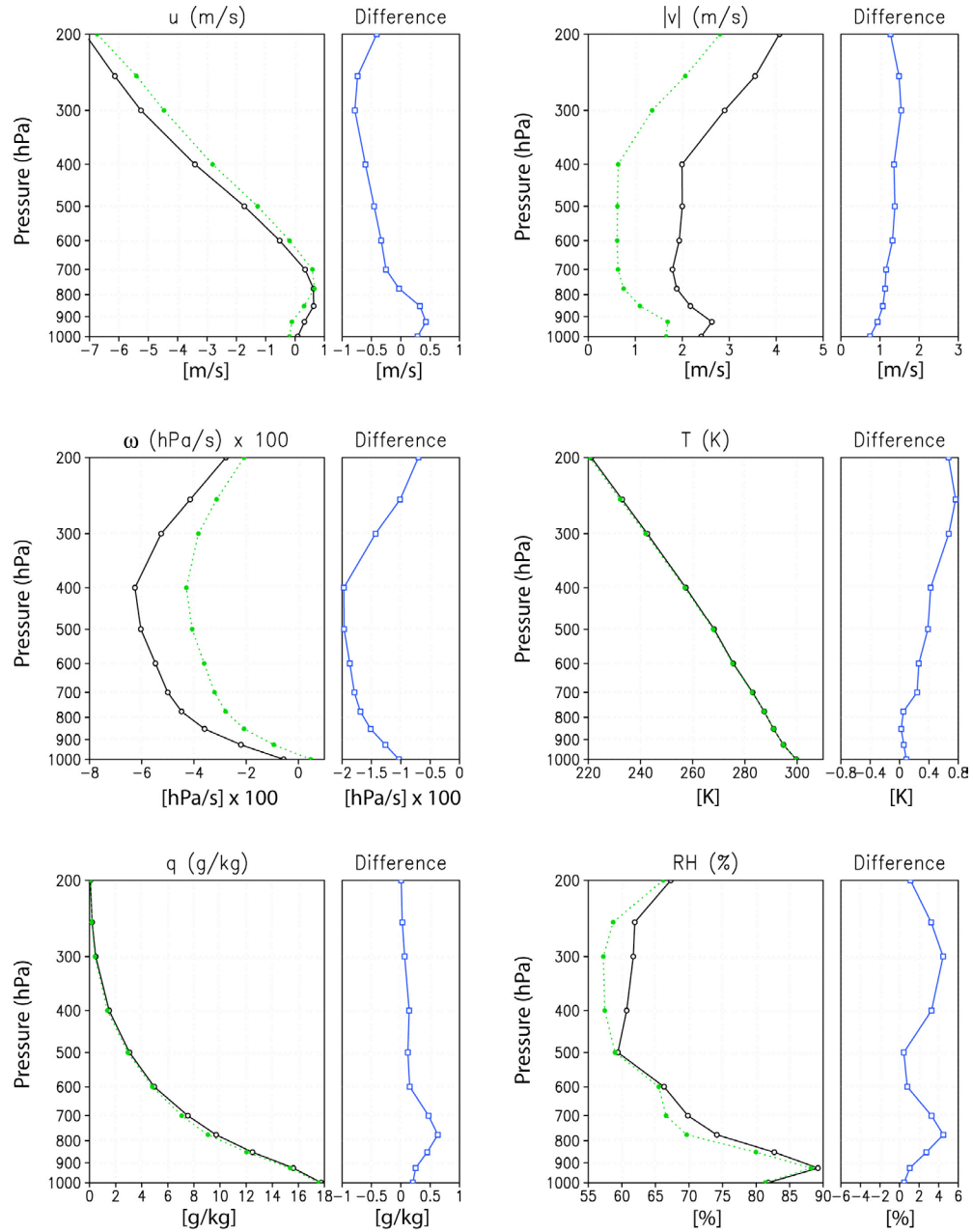


Figure 3.6: Vertical profiles of the “MJO background state” (solid black lines) and 18-year climatology (1984-2001; dotted green lines). Zonal wind (u), meridional wind magnitude ($|v|$), pressure velocity (ω), temperature (T), specific humidity (q), and relative humidity (RH) are plotted. The MJO background is defined as the departure from the mean atmospheric state during an MJO convective event (see Appendix A for description). Differences between the MJO background state and climatology (MJO-climatology; solid blue lines) are included at the right of each panel.

Table 3.1. A comparison of several atmospheric and oceanic ERA40 variables between long-term climatology and the MJO “background state.” The background state is defined as that value averaged over all lag days for all events (see Appendix A for details). The column titled σ_{diff} represents the standard deviation of differences between each event’s time mean (all lag days) and its corresponding 18-yr calendar-day climatology. The variable list includes zonal wind u , temperature T , specific humidity q , outgoing longwave radiation (OLR), sea-surface temperature (SST), precipitable water (PW), and surface latent heat flux (SLHF).

<i>Variable</i>	<i>Units</i>	<i>18-yr Climatology</i>	<i>"MJO" State</i>	<i>σ_{diff}</i>
u (1000 hPa)	ms^{-1}	-0.2	0.1	0.7
u (850 hPa)	ms^{-1}	0.3	0.6	1.0
u (200 hPa)	ms^{-1}	-6.7	-7.2	1.4
T (850 hPa)	K	291.0	291.0	0.4
T (200 hPa)	K	220.5	221.2	0.4
q (850 hPa)	gkg^{-1}	12.0	12.5	0.4
OLR	Wm^{-2}	228.4	221.0	8.0
SST	K	301.7	302.1	0.4
PW	mm	51.8	53.8	2.2
SLHF	Wm^{-2}	119.1	124.9	8.4

As a final assessment of the climatological tropical atmosphere, we spectrally analyze daily TRMM precipitation. This procedure, discussed in Chapter 2, involves removing the smoothed, “red” background signal from antisymmetric and symmetric components about the Equator, thus yielding relatively large peaks of rainfall in spectral space. Figure 3.7 reveals these relatively large peaks in spectral power of tropical precipitation decomposed by period and zonal wavenumber. Many of the distinguishing features in Fig. 3.7 match the theoretical wave types predicted by Matsuno (1966). Antisymmetric wave components (panel a) are most strongly organized into mixed Rossby-gravity waves (MRG), $n=0$ eastward-propagating inertio-gravity waves (EIG), and the MJO. There is also evidence of westward-propagating tropical cyclones in the antisymmetric plot, showing power at periods 3-8 days and wavenumbers -5 to -14. Tropical waves that are symmetric about the Equator (panel b) tend to be organized into Kelvin waves, $n=1$ equatorial Rossby waves (ER), intraseasonal oscillations such as the MJO, and westward-propagating inertio-gravity waves (WIG). The results of Fig. 3.7 are similar to those of previous studies. Cho et al.

(2004) utilized TRMM precipitation and OLR at slightly lower resolution (2.5°) to obtain results reminiscent of Fig. 3.7, while WK99 and Roundy and Frank (2004) present similar spectral diagrams of NOAA OLR. We call attention to the fact that the MJO wave type has both symmetric and antisymmetric characteristics, and its combined power signal is larger than any other individual wave type, reiterating the importance of intraseasonal oscillations on tropical atmospheric variability. As was mentioned in Chapter 2, a combined (symmetric + antisymmetric) spectral diagram is employed to isolate the MJO signal,

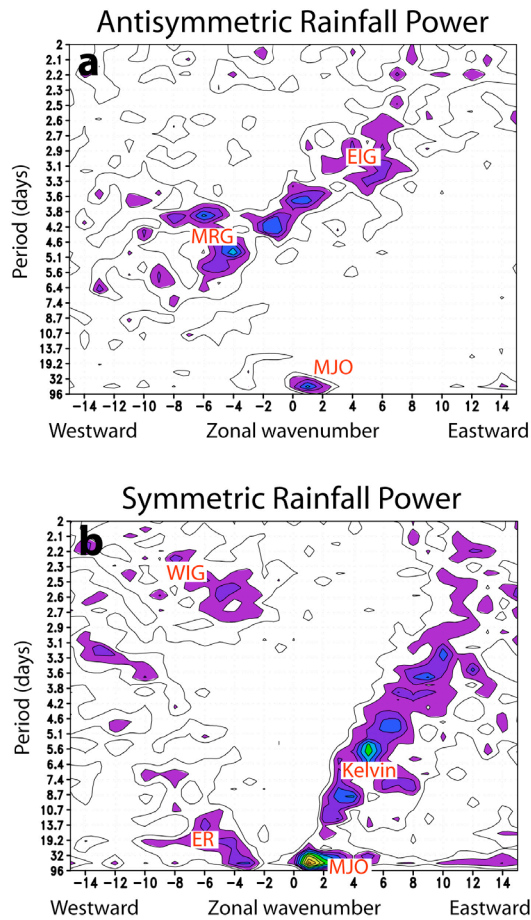


Figure 3.7: Spectral power diagrams of tropical wave types based on asymmetric (a) and symmetric (b) TRMM rainfall data about the Equator. The data have been transformed into zonal wavenumber-frequency space (plotted according to wave period). The \log_{10} of rainfall power summed between 15°S and 15°N is plotted, as in Wheeler and Kiladis (1999). Wave types are indicated in red letters and include westward- and eastward-propagating inertio-gravity waves (WIG and EIG, respectively), Kelvin waves, $n=1$ equatorial Rossby waves (ER), mixed Rossby-gravity waves (MRG), and the Madden-Julian Oscillation (MJO). No normalization of the power values has been applied. Shading indicates relatively larger power values, with orange shading representing the greatest power. See text for further details.

defined as all wave activity with periods of 20-100 days and wavenumbers 1-5 (positive wavenumbers correspond to eastward wave propagation). Inspection of Fig. 3.7 indicates that these spectral borders effectively capture much of the MJO phenomena.

3.2 Sensitivity Testing of Filtering and Event Selection Criteria

This section is a brief digression that focuses on the sensitivities of our MJO event selection process. We first discuss the Hovmöller data characteristics in the context of preliminary event selection, followed by some comments on temporal filtering.

In selecting MJO events based on meridionally-averaged TRMM precipitation, we chose normalized (involving the domain-averaged mean and standard deviation) rainfall anomalies as the data format in which the events were detected (see Chapter 2). Are anomaly rainfall data normalized in this fashion appropriate for the representation of precipitation systems on intraseasonal timescales? With only about six years of TRMM data, should anomaly calculations even be considered? To answer these concerns, two unique procedures are employed in the selection of MJO events in addition to the method outlined in Chapter 2. In the first alternate procedure, we avoid calculating anomalies of the rainfall data because, due to the short temporal range and large spatial and temporal variability, the *daily mean gridpoint precipitation* may be a very fragile statistical concept, such that intense convection on one particular day can radically change its value. Instead, we compute 11-day running means of the raw rainfall, average the smoothed data from 10°S-10°N, and apply criteria analogous to those discussed in Chapter 2 for selection purposes. The second alternative approach is a hybrid method that merges smoothing with departures from a mean. In this procedure, we smooth the data using 11-point temporal and 21-point zonal running means of the raw rainfall, the mean and first three harmonics of the composite annual cycle (based on the smoothed data) are subtracted, and strict criteria are applied to extract MJO events. The event selection results of both of these quantitative approaches

are nearly identical to the events detected using the methods described in Chapter 2. As a final step, we visually verify the list of final events through analysis of a Hovmöller diagram of raw, unfiltered TRMM precipitation.

As an abbreviated summary of the event selection technique, we (1) normalize spectrally-filtered rainfall anomalies, (2) conduct a preliminary event detection process (alternative methods of which are described above), (3) examine each event and pinpoint its date and location of maximum strength, (4) use that information to search for the maximum rain rate in the raw, unfiltered TRMM dataset, and (5) finally construct a timeseries (and composite) of that meridional band or single gridpoint. The final composite results are not strongly sensitive to adjustments in the search area (step 4; either longitude, latitude, or time). For example, whether the temporal search domain is ± 2 days or ± 5 days does not significantly impact the composite results. In terms of temporal filtering involving the wave period, the results based on meridional averaging are weakly sensitive to adjustments between applying a 10-100-day or 20-100-day filter. However, slight changes are noted in the gridpoint-based composites when these different temporal filters are applied, namely in the timing of the post-convective drying (these results will be discussed in detail in Chapter 4). Although the onset of drying by horizontal winds continues to lead that by vertical motions, absolute timing of this sequence may be shifted $\pm 1-2$ days when different filters are applied. A possible explanation of this issue is that the 20-100-day filter appears to detect the initiation of the MJO wave later in time (and farther east) than that of 10-100 days, owing to the nature of the spectral filter itself. The convective envelopes extracted from the raw data using the 20-100-day filter, when compared to the 10-100-day filter, last longer and have a weaker maximum signal, indicative of the enhanced space-time smoothing of the 20-100-day filter. Quantitatively, we discovered that the maximum MJO signal using the 20-100-day filter was on average 3-4 days later than and $7^\circ-8^\circ$ east of the maximum signal as detected by the 10-100-day filter. In some instances, this resulted in differ-

ent gridpoint locations being selected after the search had been run, possibly explaining the slight differences in the composites. In essence, the same eastward-propagating convective envelopes associated with the MJO are detected, but they are detected at different times and locations in their respective lifecycles. Despite this caveat, the coherent structure of the MJO convective envelope is assumed to remain nearly identical given a change of only a few days or a few degrees of longitude. Nonetheless, we must note that some differences do exist.

3.3 Meridionally-averaged Composite Results

Event locations, dates, and other information are displayed in Figure 3.8 and Table 3.2 for the meridionally-averaged framework. Of the 17 MJO events detected by the TRMM satellite, 11 are contained in ERA40 and 13 in the MODIS dataset. The locations of maximum convection occur across a range of geographic regions, from the central Indian Ocean to the West Pacific warm pool out to the International Date Line.

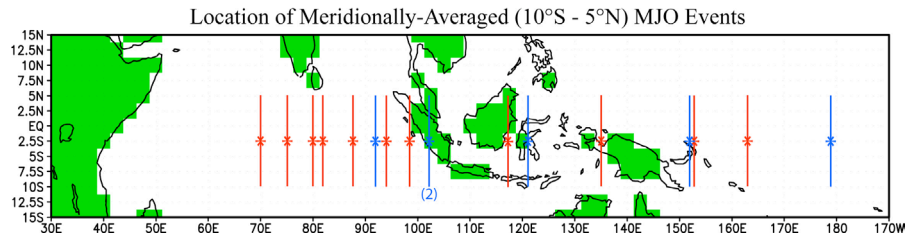


Figure 3.8: Map of MJO events, detected both in the TRMM and ERA40 datasets, that make up the composite time-height cross-sections seen in Section 3.3 (red), as well as the more recent TRMM-based events that occurred after the end of the ERA40 analysis period (blue). Green shading represents the land-sea mask of the ERA40 dataset. See Table 3.2 for details.

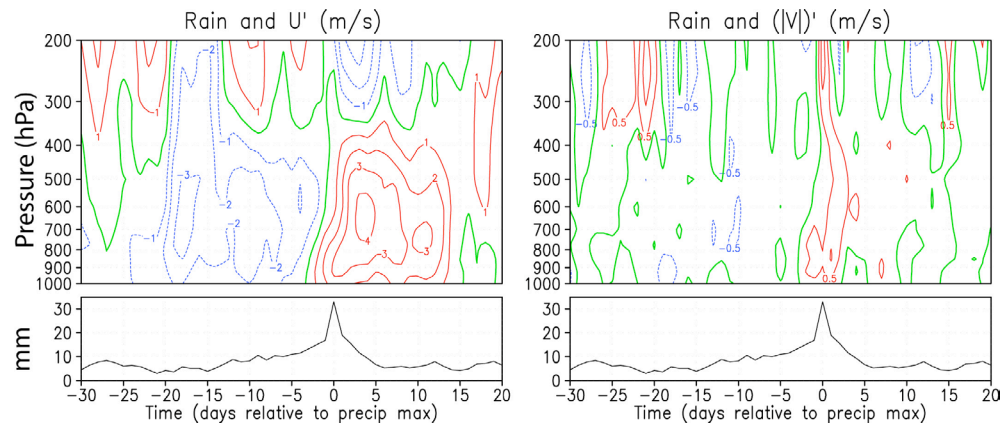
The meridionally-averaged composite time-height cross-sections of several dynamic and thermodynamic quantities are presented in Figures 3.9-3.14. The composite TRMM precipitation timeseries, as it appears repeatedly in each of these figures, is an average of all 17 MJO events. Because the TRMM dataset extends past the range of the ERA40 dataset,

Table 3.2. Specifications of MJO events based on meridionally-averaged (10°S-5°N) TRMM precipitation. Currently, ERA40 data is only available up to 31 May 2002. The table displays the event number, the date and longitude at which the maximum rainfall was detected, the (unfiltered) value of the maximum meridionally-averaged rainfall, and the datasets in which the event occurs.

<i>Number</i>	<i>Date</i>	<i>Longitude (East)</i>	<i>Max Rain (mm)</i>	<i>TRMM</i>	<i>ERA40</i>	<i>MODIS</i>
1	26 Sep 98	117°	26.1	*	*	
2	1 Nov 98	80°	27.0	*	*	
3	20 Jan 99	70°	31.6	*	*	
4	8 Dec 99	87°	30.0	*	*	
5	17 Sep 00	75°	30.0	*	*	*
6	21 Nov 00	98°	32.5	*	*	*
7	10 Feb 01	135°	27.9	*	*	*
8	16 May 01	163°	36.1	*	*	*
9	10 Dec 01	153°	28.3	*	*	*
10	26 Jan 02	94°	35.4	*	*	*
11	4 May 02	82°	38.1	*	*	*
12	30 Nov 02	179°	38.5	*		*
13	29 Dec 02	121°	44.9	*		*
14	31 Jan 03	102°	37.2	*		*
15	6 May 03	92°	30.1	*		*
16	17 Oct 03	102°	26.9	*		*
17	8 Feb 04	152°	41.4	*		*

more MJO events are detected (17 total) by TRMM than are observed in the ERA40 dataset (11); however, the 17- and 11-event TRMM precipitation composites are very similar, so we choose to use the 17-event composite timeseries for rainfall. The composite precipitation profile indicates minimal meridionally-averaged rainfall 10 to 30 days prior to the maximum in convective activity. This dry phase of the MJO, during which time the rain rate remains fairly steady at 4-8 mm/day, coincides with a period of large-scale subsidence (Fig. 3.11) and relatively low cloud-top heights (Fig. 3.18), suggesting that convective processes are suppressed. Convective activity increases gradually between days -10 and -2 as large-scale upward vertical motion strengthens. The composite rain rate is a maximum on day 0 (by construction) at approximately 30 mm/day and corresponds to the peak of the MJO wet phase. The first week following the rainfall maximum exhibits a rapid decline in

precipitation as convective processes weaken. Rain rates return to typical MJO dry phase levels (4-8 mm/day) during the second and third weeks following the peak rainfall of the wet phase. It should be noted that the meridionally-averaged rainfall profile is not symmetric about the zero lag day; rather, the profile in Fig. 3.9 (again, repeated in all figures) suggests a more gradual increase in precipitation prior to the peak and a more rapid decrease following it. For example, rain rates between days -10 and -5 are approximately 10 mm/day, while those of days +5 to +10 are less than half of that value. Many of the variables to be examined in the next few sections show consistency with this temporal precipitation asymmetry. Temporal asymmetry is consistent with the discharge-recharge theory of wave generation (Chapter 1) and will be discussed in greater detail in Section 4.2.4.



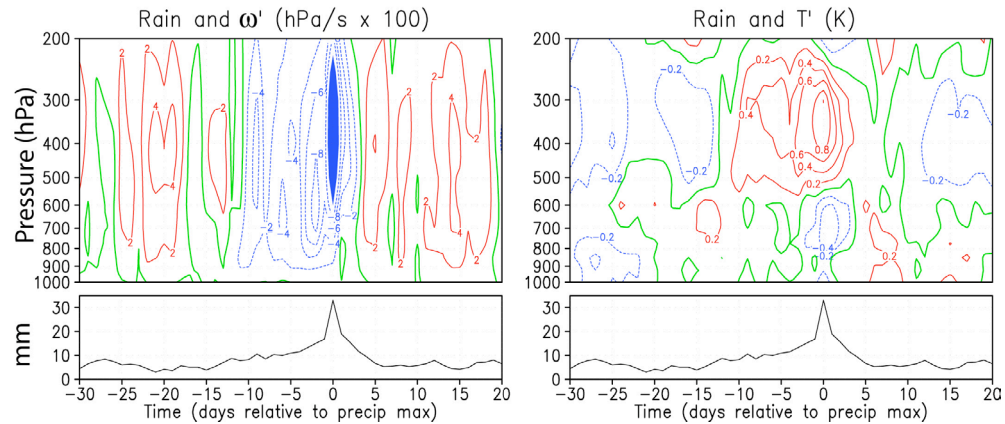
Figures 3.9 (l) and 3.10 (r): Time-height cross-sections of zonal wind anomalies (u') and anomalous meridional wind magnitudes ($|v'|$) during the composite MJO event based on the meridionally-averaged ($10^{\circ}\text{S}-5^{\circ}\text{N}$) framework. The events contained in this composite were selected with use of 20-100-day filtered TRMM rainfall (see text for explanation). The composite timeseries of total precipitation is plotted beneath both figures. Solid red lines indicate positive departures from the MJO background state, dashed blue lines represent negative departures, and thicker green lines the zero contour (see text and Appendix A for details). Lag days are indicated below the rainfall timeseries, with day 0 corresponding to the day of maximum total rainfall. Negative lag days represent those days prior to intense rain.

The composite zonal wind cross-section is displayed in Figure 3.9. In general, easterly wind anomalies dominate the troposphere up to 350 hPa between days -20 and -4. A deeper layer of easterly anomalies extends from the surface to above 200 hPa 2-3 weeks prior to the rainfall maximum. Zonal wind anomalies become westerly in the upper troposphere around day -14 and herald the approach of intense convection associated with the

MJO. Surface westerly wind anomalies first develop on day -3 and grow in depth and strengthen as the most intense precipitation passes. Simultaneously, strong easterly anomalies are observed near and just below the tropopause level and continue for two weeks following the main convective episode. Mid- and lower-tropospheric westerly anomalies commence near the time of main convection and, like the upper-level easterlies, do not diminish until day +15. Overall, the evolution of the zonal wind anomaly field corresponds nicely to the physical mechanisms of the MJO noted in Figure 1.1. A pattern of low- and mid-tropospheric convergence and upper-tropospheric divergence during the wet phase is clearly visible in the first-mode baroclinic structure of Fig. 3.9. The key features of this figure are consistent with the findings of many previous studies. K-CW01, who generated a composite MJO event (composed of eight individual events) for several variables based on radiosonde data from non-Maritime Continent stations, found wind structures (their Fig. 5) similar to those seen in Fig. 3.9 of this paper. Lin and Johnson (1996a, hereafter LJ96a) explored westerly wind bursts associated with intraseasonal oscillations (ISOs) during TOGA COARE IOP. They found that the strongest surface westerlies, which coincided with strong low-level westerlies maximized at 600-850 hPa, peaked 1-3 weeks following the intense convection (their Figures 3 and 16). Although the surface westerly anomalies in Fig. 3.9 of this paper have an absolute (but brief) maximum only one day following peak rainfall, we note a broad secondary wind maximum extending from day +7 to +11, somewhat consistent with the results of LJ96a.

The time-height evolution of the meridional wind within the equatorial band (not shown) is extremely weak owing to the meridional averaging procedure. Instead, we present $|v'|$ in Figure 3.10 to explore the flavor of meridional motions of any sort. Prior to day -3 and within much of the troposphere, meridional winds are within 0.5 m/s of their background values. With the passage of intense convection on day 0, a tongue of weak but positive $|v'|$ is observed from the surface to 200 hPa, indicating enhanced meridional motions at

this time. The anomalous magnitude of v remains slightly above average until day +14, with noted positive clusters near the surface on days +7 and +12 corresponding to the secondary maxima in u' . A detailed discussion of meridional wind magnitude and direction appears in Section 3.4 for the gridpoint framework.

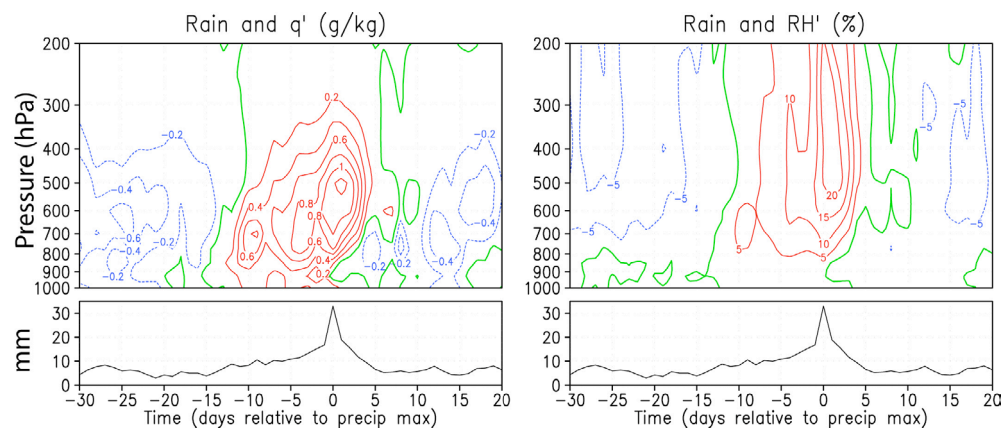


Figures 3.11 (l) and 3.12 (r): As in Fig. 3.9, but for pressure velocity and temperature anomalies (ω' and T' ; respectively). Pressure velocity anomalies less than -0.1 hPa/s ($\times 100$) are shaded blue.

Figure 3.11 displays the time evolution of the pressure velocity (ω) anomaly. In general, large-scale subsidence is observed during the dry phase, 2-4 weeks before precipitation intensity is greatest. Beginning around day -15 and extending until day -10, weak rising motion develops at low levels while subsidence continues in the middle to upper troposphere. This vertical structure of ω' could reflect the growth of shallow cumulus clouds, although the meridional averaging procedure might tend to mask localized, small-scale processes such as cumulus development. A detailed discussion of shallow cloud growth preceding intense convection associated with the MJO is given in Chapter 4. Rising motion throughout the depth of the troposphere commences on day -10 in the form of a moderate convective episode. Vertical velocities briefly diminish in magnitude following this initial convective burst but restrengthen on day -3. The ω' peak upward motion (< -0.15 hPa/s) corresponds to maximum rainfall intensity and occurs between 300 hPa and 500 hPa, consistent with the findings of LJ96a. Subsidence develops around day +4 throughout the entire depth of the troposphere and signals the onset of the MJO dry phase.

This sinking motion continues for approximately three weeks following the main convective event and is a maximum near day +14.

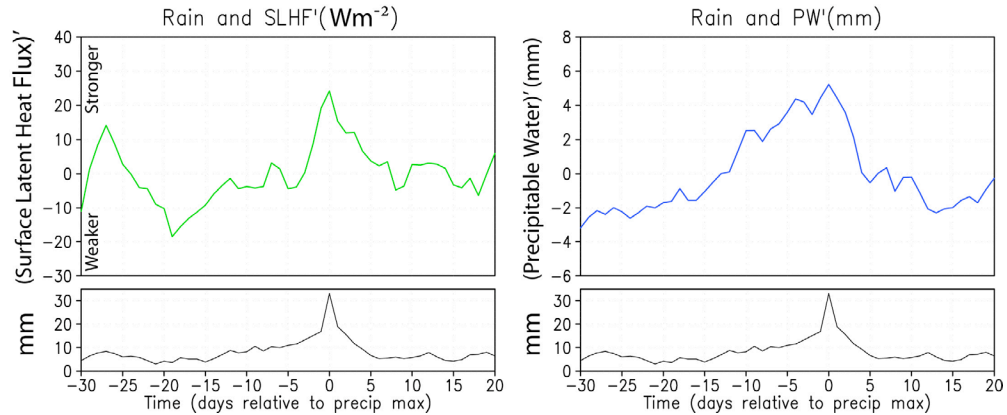
We present perturbations of meridionally-averaged tropospheric temperature in Figure 3.12. At the time of maximum rainfall, much of the middle and upper troposphere is anomalously warm with a peak temperature perturbation of 0.9 K at 300-400 hPa. Simultaneously, cool anomalies occur below 550 hPa and near tropopause level. The structure of the low-level cooling closely matches previous results based on radiosonde data (Straub and Kiladis, 2003, hereafter SK03; LJ96a), and likely arises from latent cooling of air within downdrafts (Reed and Recker, 1971) and stratiform precipitation processes (Houze, 1982). Webster and Stephens (1980) found that near-tropopausal cooling, the lower edge of which is noted in Fig. 3.12 of this paper between days -1 and +5 above 250 hPa, could result from longwave cloud-top cooling from deep convective clouds (see also Figure 3.26 in this paper). Madden and Julian (1972) speculate that this cooling may also be due to a higher tropopause level as a result of rising motion. Near day -20, weak cool anomalies erode below about 600 hPa as the lower troposphere begins to warm slightly. This weak cool-over-warm signature resumes approximately one week following the rainfall maximum.



Figures 3.13 (l) and 3.14 (r): As in Fig. 3.9, but for specific and relative humidity anomalies (q' and RH' ; respectively).

The specific and relative humidity plots appear in Figures 3.13 and 3.14, respectively. Prior to intense convection, abnormally dry air is observed during the suppressed phase of the MJO through much of the troposphere. This dry anomaly is maximized in the 600-700 hPa level. Beginning around day -20, there is a tendency for weak, shallow moistening to develop below 900 hPa, possibly due to the collective effects of shallow convective clouds. Positive moisture anomalies rise from 900 hPa to higher than 500 hPa between days -15 and -10. Note that this moistening coexists with weak $\omega' < 0$ and $T' > 0$, supporting the view that shallow cumuli play a role in preconditioning the atmosphere for later intense convection through destabilization (K-CW01, SK03). On day -4, a broad moisture maximum is observed between 650 and 750 hPa. This maximum rises to nearly 500 hPa by day +2. Delayed moistening of the middle and upper troposphere is also evident in Fig. 3.14, where positive relative humidity anomalies above 500 hPa are delayed until 2-3 days after maximum rainfall. Low-level drying (800-925 hPa) begins on day 0 and expands vertically up to the 650 hPa level by day +7. After this time, most of the troposphere abruptly returns to an anomalously dry state. In comparing these moisture results to radiosonde-based studies, we find that the spatial structures are quite similar but the magnitudes, especially for $q' > 0$ near the time of intense precipitation, are notably larger. For example, the maximum q' value in Fig. 3.13 is about 1.2 g/kg while a similar measure from K-CW01 does not exceed 0.8 g/kg. One possible explanation is that our composite contains different events (in different geographic locations) than that in K-CW01. The difference might also be explained by the ERA40 convective parameterization scheme, which constrains the behavior of several variables should convection develop (SK03).

Line profiles of several other atmospheric variables along with the TRMM composite rainfall are displayed in Figures 3.15-3.20. From Fig. 3.15, we note that the strongest surface evaporative flux anomalies (largest positive values) coincide with the strongest



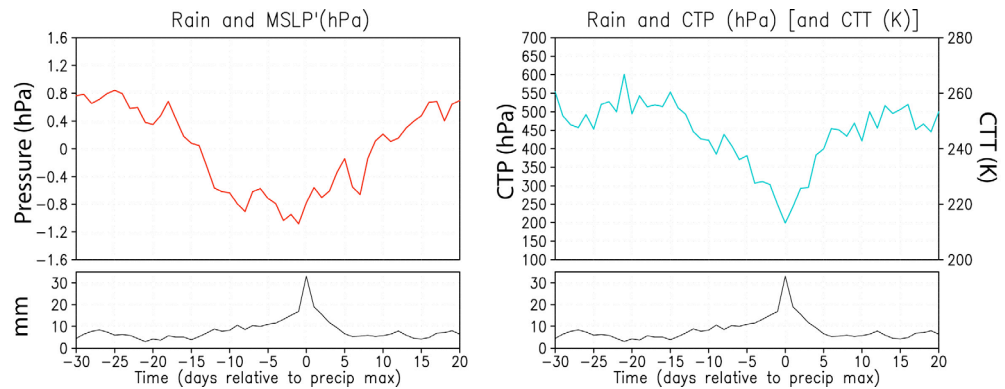
Figures 3.15 (l) and 3.16 (r): Composite timeseries of the departures of surface latent heat flux (SLHF') and precipitable water (PW') from the MJO background state for the meridionally-averaged (10°S-5°N) framework. The composites are based on the same events as those contained in Fig. 3.9.

surface winds and maximum rainfall on day 0. A weak secondary maximum in SLHF' is seen on days +10 to +14 and presumably corresponds to the combination of enhanced surface winds and low surface humidity levels at that time. This secondary maximum is far more robust in the point-based composite (see Figure 3.31), suggesting that surface latent heat fluxes associated with the MJO may be more important locally than in a meridionally-averaged sense. Leading up to the wet phase, surface evaporation associated with easterly wind anomalies is relatively weak, and thus we can conclude that, although it may be important in MJO wave generation (Grabowski and Moncrieff, 2005 in press), the WISHE mechanism does not appear to be operating during most of the events used in this composite.

The asymmetric characteristic of the TRMM rainfall profile is clearly mirrored in the precipitable water perturbation graph (Figure 3.16). A gradual but steady rise in PW' is seen in the weeks leading up to intense convection. Following the maximum in PW' (+0.5 cm), vertically-integrated moisture levels dramatically fall to the background value by day +4 and remain below average after day +8.

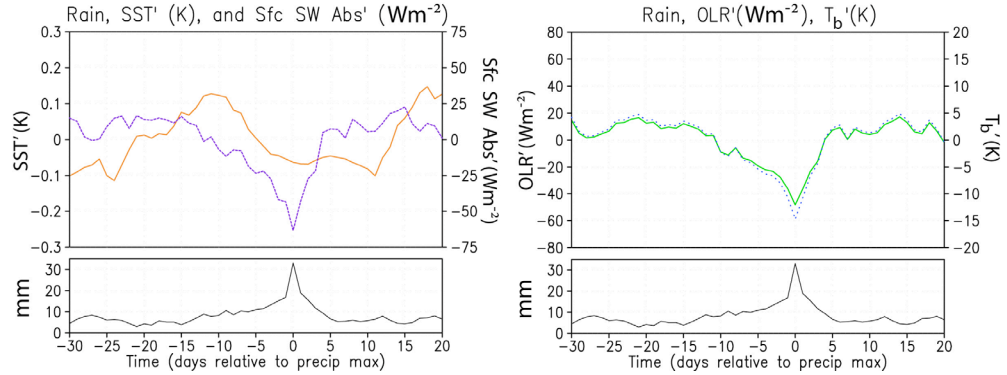
As mentioned previously, pressure gradients in the tropical regions are severely limited by the small Coriolis parameter and the ease with which the dynamics respond to mass

imbalances. Although very small compared to midlatitude baroclinic disturbances, pressure perturbations associated with tropical waves do show a characteristic ridge-trough pattern as the MJO wave passes (Figure 3.17). As we will also see in the point-based composites, a broad pressure minimum occurs just prior to the rainfall maximum. On days -3 to -1, while the pressure minimum is observed, it is likely that the vertically-integrated temperature and moisture act to lower the column density (and most likely the surface pressure), despite water loading from the increased rainfall. On day 0, the development of (a) cooler air below 550 hPa brought on by latent cooling (Reed and Recker, 1971) and (b) water loading associated with intense rainfall are likely dominant over the time rate of change of rising motion and thus slightly diminish the magnitude of the pressure fall.



Figures 3.17 (l) and 3.18 (r): As in Fig. 3.15, but for anomalous mean sea-level pressure (MSLP') and MODIS-derived cloud-top pressure (CTP; the right vertical axis of Fig. 3.18 also indicates the approximate cloud-top temperature CTT).

MODIS-derived cloud-top pressure (CTP) and temperature (CTT) are displayed in Figure 3.18. The MODIS and TRMM composites match nicely, with a minimum in meridionally-averaged CTP (200 hPa) corresponding to a maximum rainfall intensity. As with the PW' plot, a distinct temporal asymmetry is observed in CTP and CTT, with a gradual decrease in CTP prior to the wet phase and a rapid decline afterward. The drop in CTP between days -15 and -5 closely follows the elevation in q' height and magnitude and signifies the onset of deep convection. The MODIS-derived profiles and their connection to the MJO are discussed in more detail in Sections 3.4 and 4.3.2.



Figures 3.19 (l) and 3.20 (r): As in Fig. 3.15, but for anomalous sea-surface temperatures (SST' ; solid orange line in Fig. 3.19), anomalous solar radiation absorbed at the surface (SSA' , or "Sfc SW Abs"; dotted purple line in Fig. 3.19), anomalous OLR (OLR' ; solid green line in Fig. 3.20), and anomalous brightness temperature (T_b' ; dotted blue line in Fig. 3.20).

We present profiles of anomalous sea-surface temperature (SST') and solar radiation absorbed at the surface (SSA') in Figure 3.19. SST' generally rises between days -30 and -11 during which time $SSA' > 0$, suggesting less cloud coverage, weaker ocean surface mixing, and minimal rainfall. Meridionally-averaged SST' are maximized 10-12 days prior to intense precipitation and then decline as cloudiness and surface winds increase. A minimum in SST' (day +11) corresponds to the secondary maximum of surface westerlies (see Fig. 3.9). Concerning SSA', the distinct pattern of temporal asymmetry is again observed. Decreased solar absorption between days -15 and -5 is consistent with the vertical cloud growth implied by the CTP trend (Fig. 3.18).

Figure 3.20 depicts perturbations in OLR and T_b during the MJO lifecycle. As with SSA', OLR' values begin to decline around day -15, reaching a minimum (-48 Wm^{-2}) on day 0. The magnitudes of these perturbations are within the range of reasonable consistency with previous studies (LJ96a, SK03). Not surprisingly, OLR' values are greater in magnitude for the localized point-based composite (Fig. 3.36).

3.4 Gridpoint-based Composite Results

The MJO includes atmospheric processes on a number of spatial scales, from cloud scales [O(1 km)] to mesoscales [O(100 km)] to planetary scales [O(10,000 km)]. Thus far, we have analyzed the physical features of the MJO on synoptic scales [O(1000 km)] via meridional averaging. While the results from this approach capture large-scale MJO variability within the equatorial band, much of the mesoscale character of the wave may be masked by the averaging process. In an attempt to address this issue, we now explore analogous composite time-height cross-sections for single gridpoints in the TRMM, ERA40, and MODIS datasets. As with the meridional averaging framework, day 0 corresponds to the day of maximum precipitation. Additionally, and for comparison purposes, all gridpoint-based time-height cross-sections have identical contour levels as their meridionally-averaged counterparts.

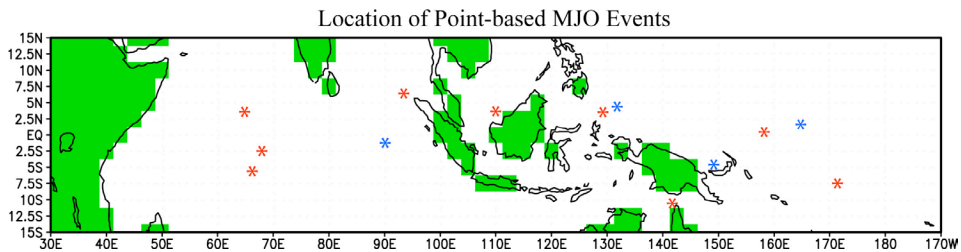


Figure 3.21: Map of MJO events, detected both in the TRMM and ERA40 datasets, that make up the composite time-height cross-sections seen in Section 3.4 (red), as well as the more recent TRMM-based events that occurred after the end of the ERA40 analysis period (blue). Green shading represents the land-sea mask of the ERA40 dataset.

Event locations, dates, and other information are displayed in Figure 3.21 and Table 3.3. Of the 13 MJO events detected by the TRMM satellite, nine are contained in both the ERA40 and MODIS datasets. Three events (not listed) were discarded after analysis of the ERA40 data revealed unreasonable values of certain variables. Most of the events listed in Table 3.3 correspond to the same eastward-propagating convective envelopes detected in

Table 3.3. Specifications of MJO events based on gridpoint-based TRMM precipitation. Currently, ERA40 data is only available up to 31 May 2002. The table displays the event number; the date, longitude, and latitude at which the maximum rainfall was detected; the (unfiltered) value of the maximum gridpoint rainfall, and the datasets in which the event occurs.

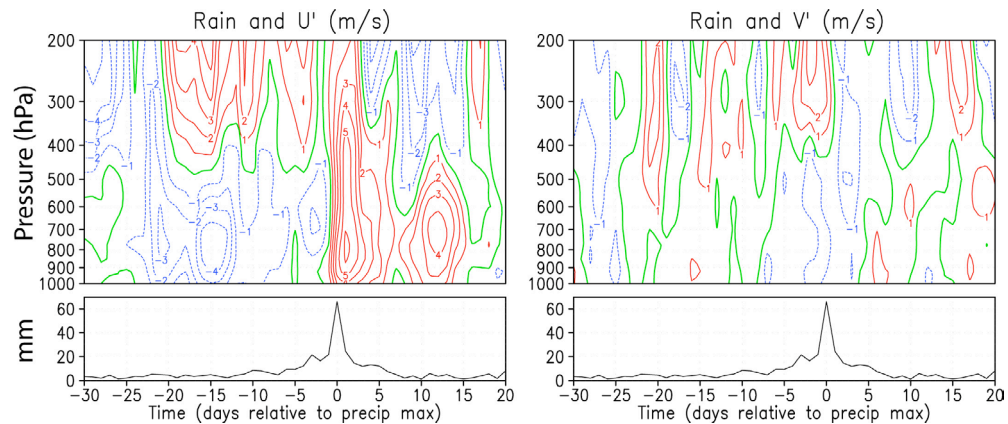
<i>Number</i>	<i>Date</i>	<i>Longitude</i>	<i>Latitude</i>	<i>Max Rain (mm)</i>	<i>TRMM</i>	<i>ERA40</i>	<i>MODIS</i>
1	21 Oct 98	68°E	2.5°S	80.1	*	*	
2	22 Oct 99	110°E	3.5°N	63.7	*	*	
3	29 Nov 99	65°E	3.5°N	73.8	*	*	
4	30 Dec 99	66°E	5.5°S	90.2	*	*	
5	2 May 00	158°E	0.5°N	75.2	*	*	*
6	22 Nov 00	94°E	6.5°N	56.8	*	*	*
7	13 Feb 01	142°E	10.5°S	47.6	*	*	*
8	13 May 01	172°E	7.5°S	61.1	*	*	*
9	11 May 02	129°E	3.5°N	64.5	*	*	*
10	29 Nov 02	165°E	1.5°N	67.7	*		*
11	4 Jan 03	149°E	4.5°S	54.8	*		*
12	27 Jan 03	90°E	1.5°S	63.6	*		*
13	16 May 03	132°E	4.5°N	62.7	*		*

<i>Number</i>	<i>Date</i>	<i>Longitude</i>	<i>Latitude</i>	<i>Max Rain (mm)</i>	<i>TRMM</i>	<i>ERA40</i>	<i>MODIS</i>
---------------	-------------	------------------	-----------------	--------------------------	-------------	--------------	--------------

the meridionally-averaged framework (see Table 3.2), although perhaps not at identical spatial or temporal points. The locations of maximum convection occur across a range of geographic regions, from the central Indian Ocean to West Pacific warm pool. None of the gridpoint locations occur immediately over Maritime Continent land masses as it is believed that strong diurnal convection in this area disrupts the large-scale instability associated with the MJO (Zhang and Hendon, 1997). In the interest of maintaining statistical integrity, we retain events located in the vicinity of the Maritime Continent and find, through further testing (not shown), that their profiles are not radically different than the profiles from open ocean gridpoints.

The gridpoint-based composite time-height cross-sections of a number of basic atmospheric and oceanic variables appear in Figures 3.22-3.30. The TRMM precipitation

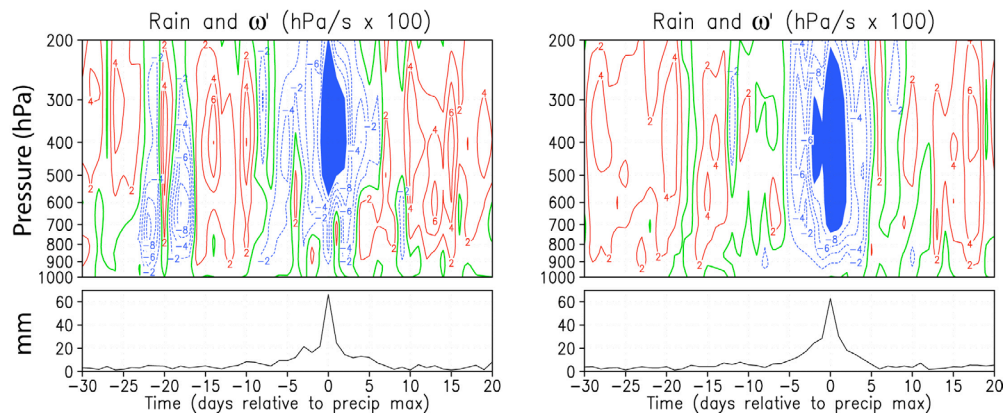
timeseries repeated in each figure is a composite based on all 13 events and is very similar to that based on the nine events (not shown) which make up the ERA40 composite cross-sections pictured. In the TRMM profile, the overall rain amounts prior to day -5 and after day +5 are quite similar (4-8 mm/day) to the meridionally-averaged case. However, precipitation values during the wet phase are higher for the single gridpoint composite, which has a strong day-0 peak (66 mm/day) nearly double that of the meridionally-averaged framework, whose maximum is noticeably less abrupt (e.g., see Fig. 3.9).



Figures 3.22 (l) and 3.23 (r): Time-height cross-sections of zonal and meridional wind anomalies (u' and v' , 3.22 and 3.23 respectively) during the composite MJO event based on the individual gridpoint framework. The events contained in this composite were selected with use of 20-100-day filtered TRMM rainfall (see text for explanation). The composite timeseries of total precipitation is plotted beneath both figures. Solid red lines indicate positive departures from the MJO background state, dashed blue lines represent negative departures, and thicker green lines the zero contour (see text and Appendix A for details). Lag days are indicated below the rainfall timeseries, with day 0 corresponding to the day of maximum total rainfall. Negative lag days represent those days prior to intense rain.

Zonal wind anomalies are presented in Figure 3.22. The same basic features are shared between the gridpoint- and meridionally-averaged cases, with several highlighted differences. The relative depths of the pre-convective low-level easterly and post-convective westerly anomalies are notably shallower in the gridpoint case. Additionally, the onset of strong westerlies occurs earlier and is more vertically uniform in the gridpoint framework. And finally, the secondary peak in lower-tropospheric westerlies in Fig. 3.22 appears more clearly defined than in Fig. 3.9, suggesting that the dynamics of such westerly bursts are important on scales of several hundred kilometers or less within the larger convective envelope, a result consistent with the findings of LJ96a.

Meridional wind anomalies assessed at a particular gridpoint are displayed in Figure 3.23. Comparison with u' (Fig. 3.22) and $|v'|$ (Fig. 3.10) suggests that (a) meridional wind anomalies are far weaker than zonal anomalies and (b) the enhanced meridional magnitudes immediately following the rainfall maximum and those near day +12 are northerly winds (negative values in Fig. 3.23). That there are relatively weak meridional winds is a reasonable expectation given the convectively-coupled Kelvin wave nature of the oscillation, where pure Kelvin waves are associated with only zonal wind perturbations. In terms of point (b) above, a number of previous observational studies, including LJ96a and Yanai et al. (2000; their Figs. 7b and 8b), have reported air motions related to the westerly wind bursts to be from a west-northwest direction, consistent with the findings here.



Figures 3.24 (l) and 3.25 (r): Time-height cross-sections of anomalous pressure velocities (ω' ; hPa/s \times 100) for the MJO gridpoint composite event based on events selected with use of 20-100-day filtered TRMM rainfall (Fig. 3.24) and 10-100-day filtered TRMM rainfall (Fig. 3.25; see Section 3.2 for explanation). The corresponding composite timeseries of total precipitation are plotted beneath both figures. Contours and shading are identical to those used in Fig. 3.11.

Perturbations of vertical motion as compared to the MJO background state appear in Fig. 3.24. These gridpoint-based profiles are noisier than their meridionally-averaged counterparts, but share the same physical characteristics: general subsidence during the dry phase, a tendency for weak rising motion near the surface 1-2 weeks prior to main convection, and intense upward motion coinciding with maximum rainfall. As an exploratory test, we generated a ω' composite for a 10-100-day filter with a smaller search area and found more clarity in the pre-convective area of weak rising motion and overlying subsidence (days -5

to -15 of Fig. 3.25). The profiles of individual gridpoints presented in this section capture mesoscale [$O(100 \text{ km})$] features of the MJO wave passage. In terms of the pressure velocity, we note the effects of stratiform precipitation processes, which play a substantial role in the dynamics and thermodynamics on mesoscales (Houze, 1982). In Fig. 3.24 on day +1, evidence of a narrow mesoscale downdraft underlying strong upward motion above 500 hPa is apparent. The stratiform precipitation signature is distinguishable even 3-6 days following the maximum rainfall, at which time weak subsidence underlies rising motion with an inflection point at 550 hPa, the approximate tropical freezing level (Johnson et al., 1996). The vertical motion field derived from a 10-100 day filter (Fig. 3.25) does not depict such stratiform processes as clearly as Fig. 3.24, but the temperature profile associated with the former figure (not shown) strongly suggests that stratiform processes are active.

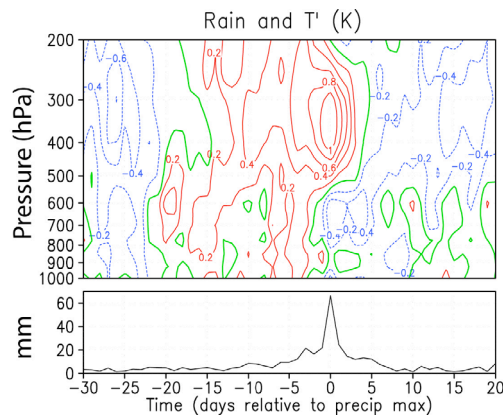
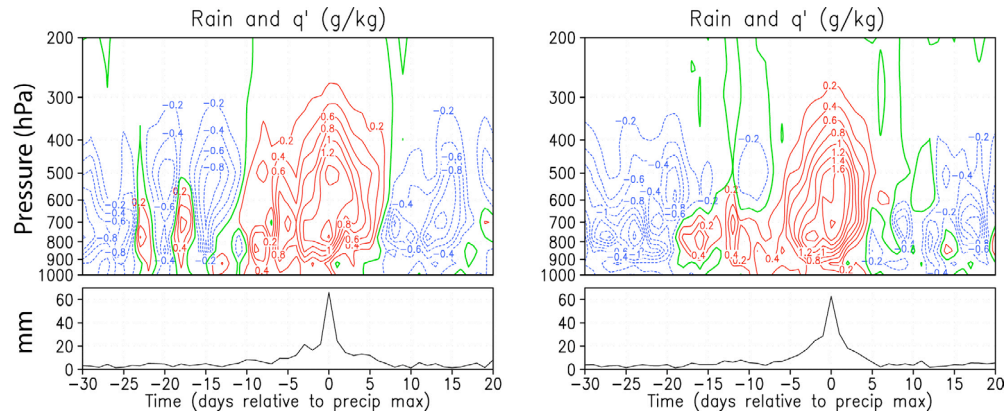


Figure 3.26: As in Fig. 3.22, but for temperature anomalies (T').

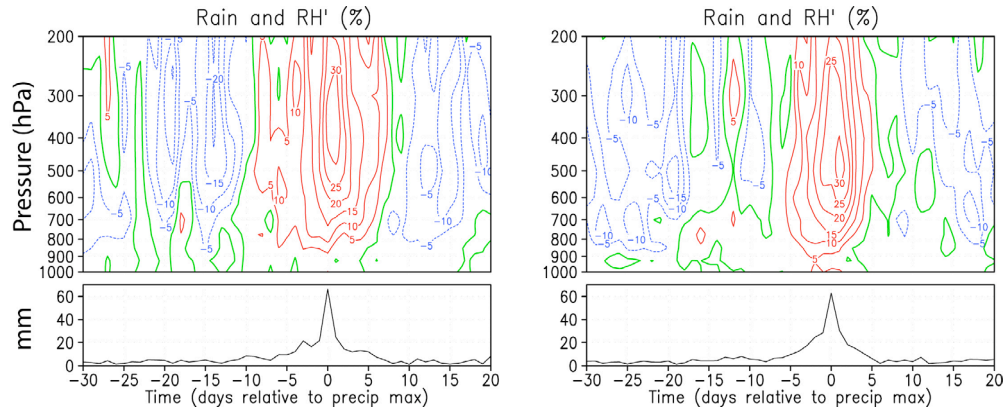
The temperature cross-section of Figure 3.26 appears very similar to that of the meridionally-averaged case. As one exception, advection of warm air by westerly winds (see Fig. 3.12) occurs a few days earlier in the mid- to upper troposphere, especially near the 250-400 hPa level. Overall, these observations jive with the results of Bladé and Hartmann (1993), who found that warm air advection from a mature upstream perturbation acts to enhance stability and occurs 10-15 days prior to the arrival of the perturbation itself. Addi-

tionally, stratiform processes in which cooling via thermodynamic considerations (melting and evaporation) occurs in lower-tropospheric downdrafts and warming via condensation occurs in mid- and upper-tropospheric ascent regions are evident in Fig. 3.26 from day 0 to +5.



Figures 3.27 (l) and 3.28 (r): Time-height cross-sections of anomalous specific humidity (q') for the MJO gridpoint composite event based on events selected with use of 20-100-day filtered TRMM rainfall (Fig. 3.27) and 10-100-day filtered TRMM rainfall (Fig. 3.28; see Section 3.2 for explanation). The corresponding composite timeseries of total precipitation are plotted beneath both figures. Contours are identical to those used in Fig. 3.13.

The moisture variables examined in this study are presented in Figures 3.27-3.30. In keeping with the meridionally-averaged case, the moisture maximum is observed 1-2 days after intense precipitation at a level near 500 hPa. The pre-convective low-level moistening begins in earnest at about the same time as in Fig. 3.13, near day -15. Prior to this, moistening is highly episodic in nature. For comparison, we present q' and RH' (Figs. 3.28 and 3.30, respectively) using the 10-100-day filter and smaller search area, as mentioned in Section 3.2. In these figures, a solid layer of elevated moisture levels is observed below 650 hPa from day -17 to day -7. It is believed that preconditioning via low-level moistening and warming serves to destabilize the atmosphere, making it vulnerable to future convective episodes (Bladé and Hartmann, 1993; Hu and Randall, 1994). Figs. 3.24-3.30 clearly suggest that preconditioning of this sort plays an important role in the generation and evolution of the MJO wave, and this topic will be discussed more in Section 4.2.4.

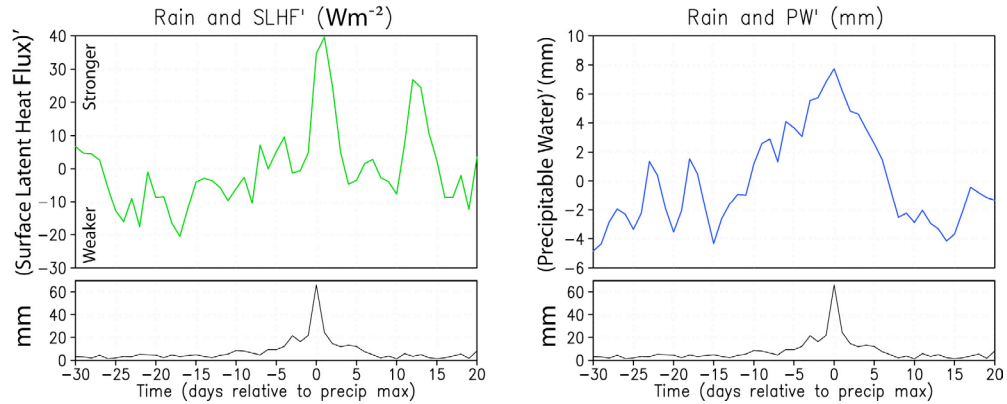


Figures 3.29 (l) and 3.30 (r): Time-height cross-sections of anomalous relative humidity (RH') for the MJO gridpoint composite event based on events selected with use of 20-100-day filtered TRMM rainfall (Fig. 3.29) and 10-100-day filtered TRMM rainfall (Fig. 3.30; see Section 3.2 for explanation). The corresponding composite timeseries of total precipitation are plotted beneath both figures. Contours are identical to those used in Fig. 3.14.

Profiles of several atmospheric and oceanic variables appear in Figures 3.31-3.36. Again, for ease of comparison, the y-axis ranges of each plot match those of the meridionally-averaged case. Concerning perturbations of surface evaporative fluxes (SLHF') in Fig. 3.31, relatively weak values are noted prior to intense convection. Strong surface fluxes (large positive values) develop at the time of maximum rainfall and quickly retreat toward background levels by day +3, a much more rapid decline than that seen in Fig. 3.15. A potent secondary SLHF' peak occurs on day +12 and coincides nicely with the secondary zonal wind anomaly peak (Fig. 3.22). Scrutinizing the meridionally-averaged SLHF' results, it is clear that surface fluxes are far more active on scales of a few hundred kilometers or less. Despite its position within the dry phase, this secondary SLHF' peak ultimately contributes to the low-level moistening that will eventually prepare the atmosphere for yet another intraseasonal convective event (LJ96a).

Though noisier, precipitable water anomalies (Figure 3.32) are similar to those seen in Fig. 3.16. The temporally asymmetric behavior is again noted, with a gradual increase in pre-convective PW' and above-normal column water between days -10 and +7.

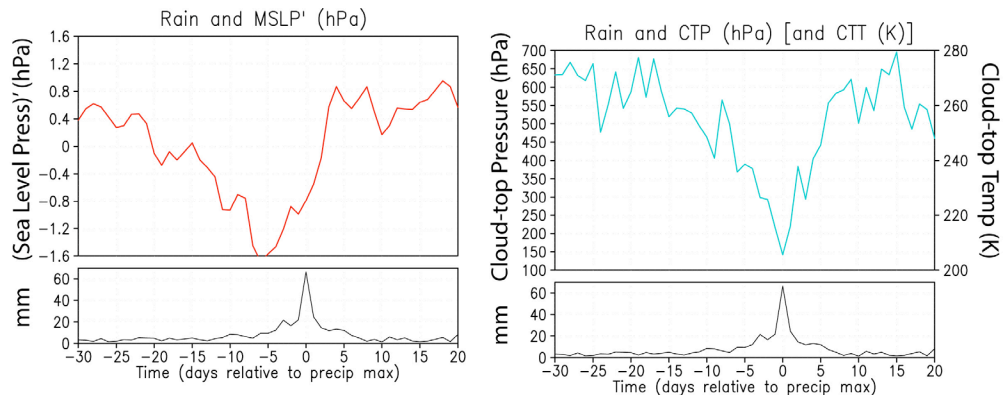
Concerning perturbations in mean sea-level pressure (MSLP'; Figure 3.33), a broad maximum precludes intense rainfall by 4-6 days. Arguments detailing the origins of this



Figures 3.31 (l) and 3.32 (r): Composite timeseries of the departures of surface latent heat flux (SLHF') and precipitable water (PW') from the MJO background state for the individual gridpoint framework. The composites are based on the same events as those contained in Fig. 3.22.

observation are outlined in Section 3.3. We also note that the magnitude of this minimum as well as the range of anomalies surpass those of the meridionally-averaged framework.

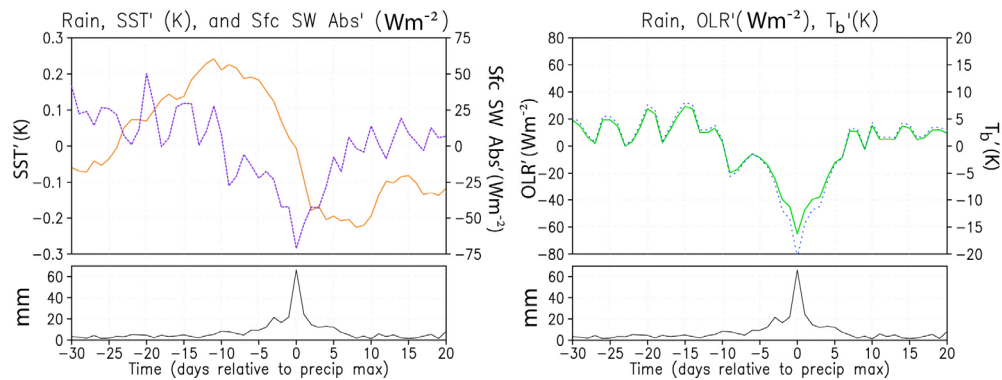
The composite MODIS-derived CTP (and CTT) is displayed in Figure 3.34. In general, CTP values during the dry MJO phase are 50-150 hPa higher than those resulting from the $10^{\circ}S-5^{\circ}N$ averaging scheme. Prior to day -12, CTPs remain near or below the approximate



Figures 3.33 (l) and 3.34 (r): As in Fig. 3.31, but for anomalous mean sea-level pressure (MSLP') and MODIS-derived cloud-top pressure (CTP; the right vertical axis of Fig. 3.34 also indicates the approximate cloud-top temperature CTT).

tropical freezing level of 550 hPa (Johnson et al., 1996). After day -12, cloud tops increase steadily, rising to the tropopause level and possibly higher by day 0 (Danielsen, 1993), after which time they return to typical dry phase levels. Following maximum rainfall, lowering cloud tops return to approximately 600 hPa by day +12. At this time, and as we will show

in Figs. 3.35 and 3.36, surface solar absorption (SSA') and OLR' values are near their background levels. This time also coincides with the secondary peak in surface westerly winds. Collectively, this does not support the result from LJ96a that westerly wind bursts tend to occur concomitantly with high cirrus coverage, and thus reduced OLR values. One explanation of this discrepancy might involve the geographic location and number of events contained within each composite. It is possible that MJO wave passages within the localized TOGA COARE IOP region tend to be associated with strong cirrus outflow, or alternatively that the three events captured during the 1992-93 project coincidentally had strong cirrus outflow that may not be the case with typical wave passages in that area. Another explanation might involve the convective parameterizations associated with the ERA40 dataset. Given that ERA40 precipitation totals and variances are notably higher than TRMM, the reanalysis model might also overestimate the zonal winds in close proximity to strong convective episodes associated with the MJO. Similarly, those same convective parameterizations might also poorly model detrained upper-tropospheric moisture from cumulonimbus clouds, and thus overestimate the OLR signal. Further discussion on this topic can be seen in Sections 4.2.2 and 4.2.3.



Figures 3.35 (l) and 3.36 (r): As in Fig. 3.31, but for anomalous sea-surface temperatures (SST' ; solid orange line in Fig. 3.35), anomalous solar radiation absorbed at the surface (SSA' , or “Sfc SW Abs”; dotted purple line in Fig. 3.35), anomalous OLR (OLR' ; solid green line in Fig. 3.36), and anomalous brightness temperature (T_b' ; dotted blue line in Fig. 3.36).

The evolutions of gridpoint-based SST' and SSA' appear in Figure 3.35. As with the meridionally-averaged case, maximum SST' leads maximum rainfall by about two weeks

(~0.25 cycle). Two minima in SST' (day +7 and +19) occur approximately one week following the corresponding maxima in u' and $SLHF'$ (see Figs. 3.22 and 3.31, respectively). With a lag of greater than one week, SST' follows SSA' , although the latter is quite noisy. Maximum SSA' values (-75 Wm^{-2}) coincide with maxima in cloud heights, vertical motions, upper-level moisture, and rainfall on day 0.

Figure 3.36 depicts the OLR' and T_b' profiles. The gridpoint-based results closely match the 10°S - 5°N -averaged profiles, with slightly positive perturbations during the dry phase interrupted by a sharp wet phase minimum. Minima in OLR' (-65 Wm^{-2}) and T_b' (-20 K) appear to be within the range of previous studies (K-CW01, SK03, LJ96a).

Chapter 4

Results and Discussion II: Mechanisms of the MJO

Thus far, several important observations concerning the temporal and spatial evolution of the MJO have been presented. Key elements of an MJO wave passage include a gradual pre-convective heating and moistening of the lower troposphere occurring simultaneously with weak low-level upward motion, a transition to intense rainfall during the wet phase, and a rapid post-convective drying trend.

In this chapter, we turn our attention to the advective and convective processes that relate to heat and moisture, as associated with the MJO. These mechanisms represent the effects of large-scale components and the *collective* effect of small-scale components, including intrusions of drier air from the subtropics and shallow cumulus transports. The term *collective* is used because small-scale processes such as heating by shallow cumulus growth occur on scales that are small compared to the area of the $2.5^\circ \times 2.5^\circ$ ($\sim 8 \times 10^4 \text{ km}^2$) ERA40 gridbox. While individual shallow cumuli have a small effect on the larger environment, over time the effect of the shallow cumulus *regime* can have a significant impact on the initiation and maintenance of the MJO (Nitta and Esbensen, 1974; LJ96b; DeMott and Rutledge, 1998).

4.1 Advective and Convective Processes of the MJO

In the following subsections, we will focus on the horizontal and vertical components of advective transport of heat and moisture; introduce and analyze MJO convective processes (apparent heating [Q_1] and moistening [Q_2]); discuss physical relationships among Q_1 , Q_2 , T , and q ; and investigate some basic aspects of the apparent moisture sink. Lastly, we present a brief comparison of MODIS-derived CTP and GLAS-derived cloud-top heights, and discuss the implications of possible differences between these two sources in the context of cirrus cloud coverage.

4.1.1 Horizontal and vertical components of advective transport of heat and moisture

Our first investigation involving the advective processes associated with the MJO addresses specific humidity q . The derivation of the moisture budget analysis is outlined in Appendix B and essentially involves a decomposition of the anomalous time rate of change of q , $\left(\frac{\partial q}{\partial t}\right)'$, into horizontal and vertical advective components. The result of this simple derivation is an equation for the tendency of q' ,

$$\frac{\partial q'}{\partial t} = -\left(u \frac{\partial q}{\partial x}\right)' - \left(v \frac{\partial q}{\partial y}\right)' - \left(\omega \frac{\partial q}{\partial p}\right)' + S_q' - C', \quad (4.1)$$

where u , v , and ω are the zonal, meridional, and vertical winds, and S_q and C the sources and sinks of q , respectively. We chose the advective form of the moisture budget equation in order to diagnose changes in q at a particular point or latitudinal band. As is noted in Appendix B, the contributions by the anomalous moisture sources and sinks (evaporation and condensation, respectively) are not explicitly analyzed due to the absence of these ERA40 data on individual pressure levels.

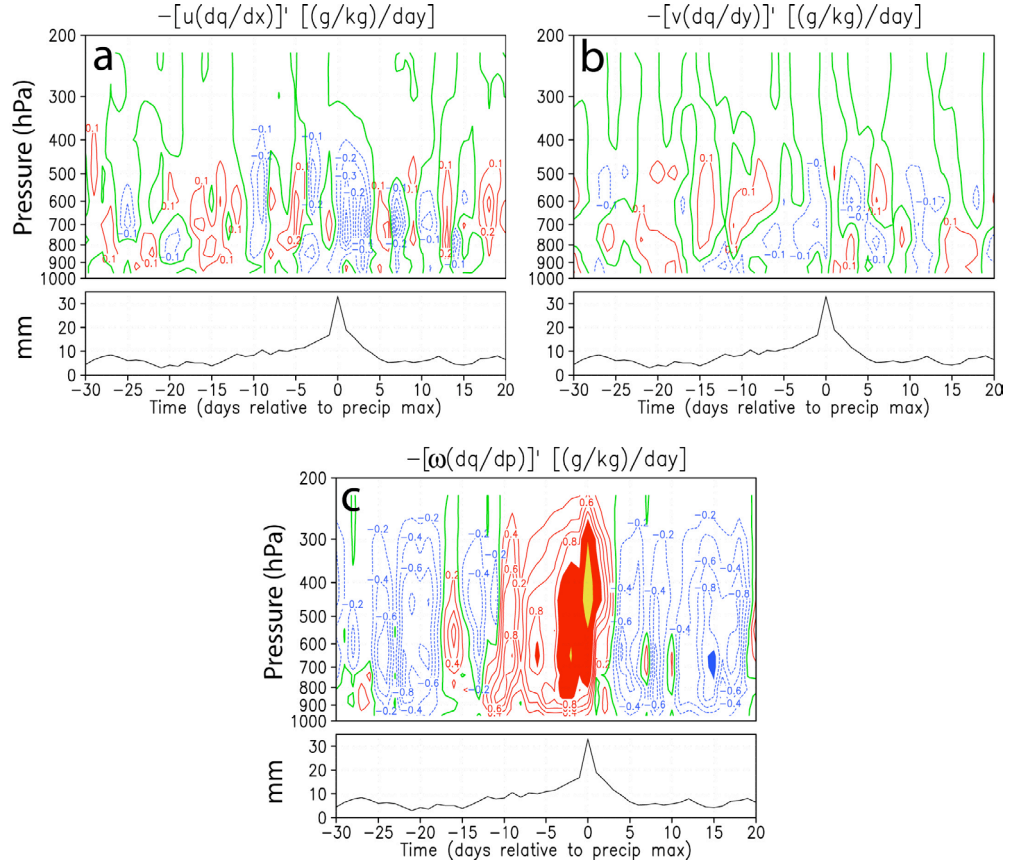


Figure 4.1: Time-height cross-sections of the zonal (a), meridional (b), and vertical (c) components of the anomalous time rate of change of specific humidity $\left[\left(\frac{\partial q}{\partial t}\right)'\right]$ for the meridionally-averaged (10°S - 5°N) framework. The events contained in this composite were selected with use of 20-100-day filtered TRMM rainfall (see text for explanation). The composite timeseries of total precipitation is plotted beneath all panels. Solid red lines indicate positive departures from the MJO background state (moistening), dashed blue lines represent negative departures (drying), and thicker green lines the zero contour (see text and Appendix A for details). Blue, red, and yellow shading indicate values less than -1.0 (g/kg)/day, between $+1.0$ and $+2.0$ (g/kg)/day, and greater than $+2.0$ (g/kg)/day, respectively. Lag days are indicated below the rainfall timeseries, with day 0 corresponding to the day of maximum total rainfall. Negative lag days represent those days prior to intense rain.

Figure 4.1 displays the zonal (a), meridional (b), and vertical (c) components of advective transport of q for the meridionally-averaged framework (10°S - 5°N). Overall, horizontal advection produces drying in the few days before and after the day of maximum rainfall. Of particular interest is the strong drying by the u wind on days 0 to +4, from 650 to 800 hPa. Weak but consistent drying by the horizontal wind is also noted throughout the lower troposphere between days +10 and +12, the time of westerly wind bursts (WWBs). Unlike the horizontal components of q transport, the vertical component (Figure 4.1c) appears to play the dominant role in the two weeks leading up to maximum rain intensity. After an

initial mid-tropospheric impulse on day -16, a steadier vertical transport of moisture emanating from the surface commences on day -13. Maxima in vertical q transport first occur at 650 hPa on day -2 and later at 450 hPa on day 0. The vertical component continues to increase q through day +3, in stark contrast to the decisive drying by the u wind. The strongest subsidence drying is delayed until approximately two weeks following maximum convective activity and coincides with the WWB apparent in Fig. 3.9.

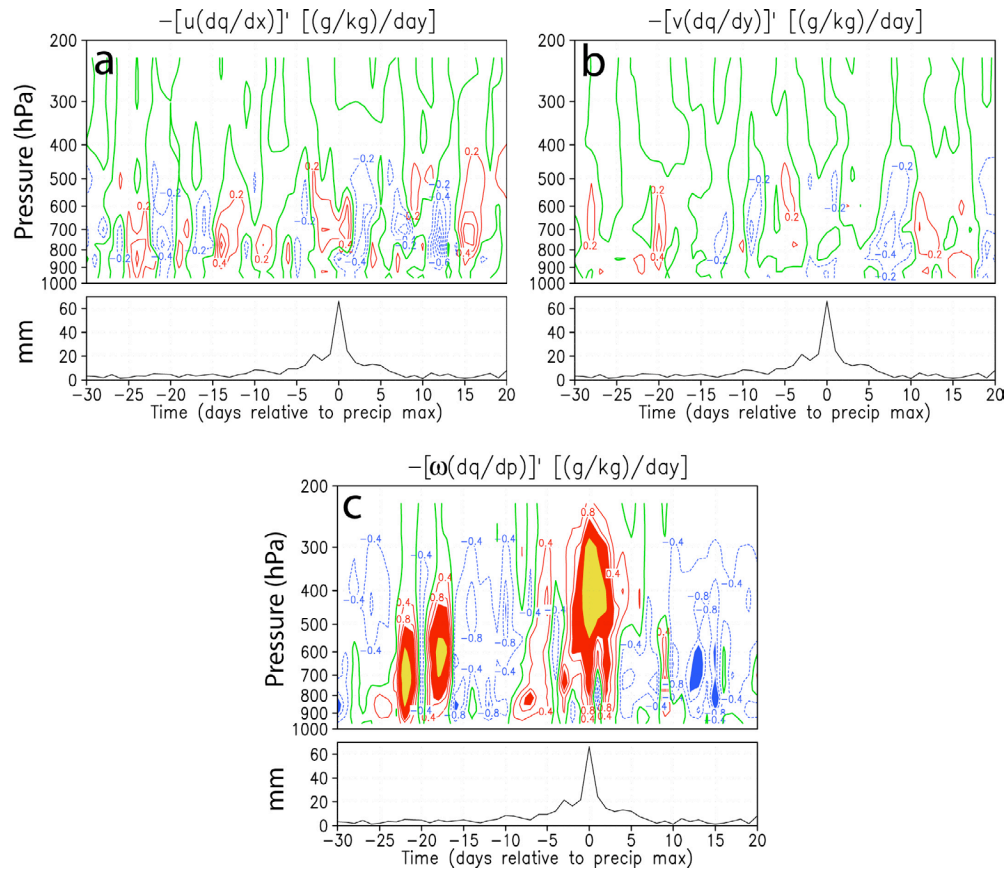


Figure 4.2: As in Figure 4.1, but for the individual gridpoint framework and based on events selected with use of 20-100-day filtered TRMM rainfall (see Section 3.2 for explanation). The corresponding composite timeseries of total precipitation are plotted beneath both figures. Contours and shading are identical to those used in Figure 4.1.

Concerning the gridpoint-based framework (Figures 4.2 and 4.3), the results are qualitatively similar. For clarity, the contour interval for the gridpoint-based transport cross-sections is *twice* that of the meridionally-averaged case. Despite a brief burst of moistening near 700 hPa on day +1, a drying trend quickly follows. Comparison of Figs. 4.2 and 4.3

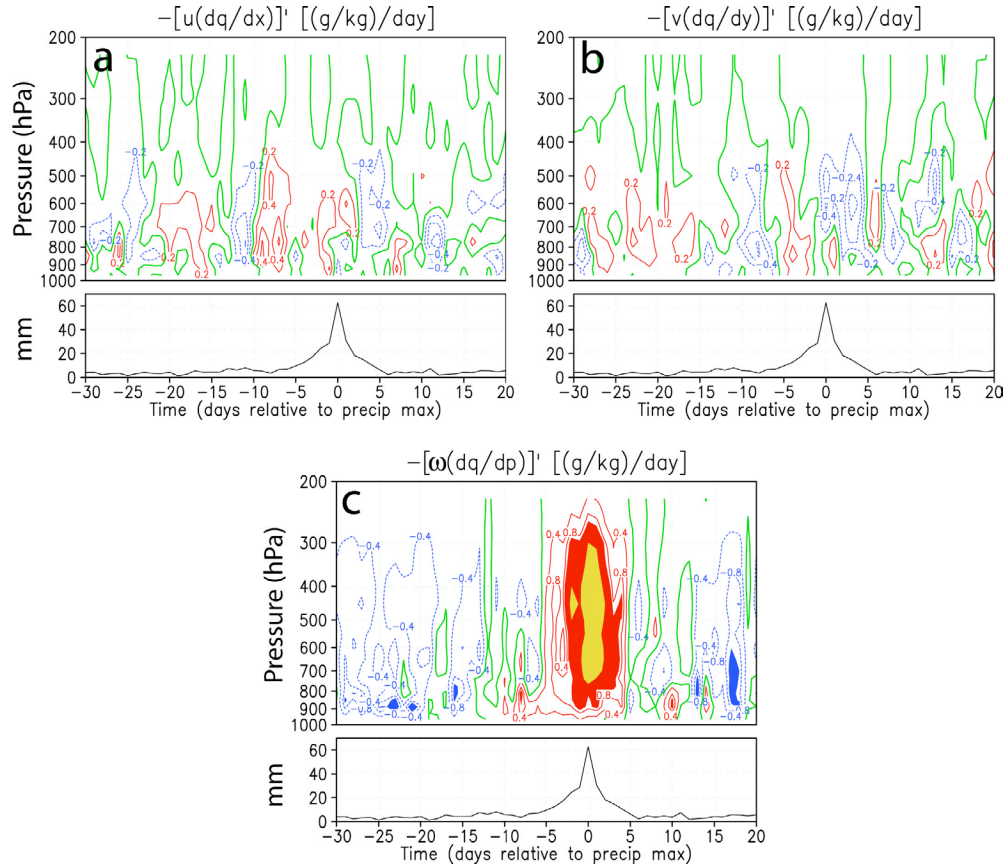


Figure 4.3: (Above) As in Figure 4.1, but for the individual gridpoint framework and based on events selected with use of 10-100-day filtered TRMM rainfall (see Section 3.2 for explanation). The corresponding composite timeseries of total precipitation are plotted beneath all figures. Contours and shading are identical to those used in Figure 4.1.

suggests that the effects of preconvective moistening by the horizontal wind may have some importance in the increase in q , but nonetheless is usually dominated by the vertical transport component at a given time and pressure. Similar to the meridionally-averaged case, these vertical q transports in the gridpoint framework serve to increase low-level moisture prior to intense rainfall. We interpret the vertical structure between days +3 and +6 of Fig. 4.2c as a stratiform precipitation signature in which dry air is entrained into the lower-tropospheric mesoscale downdrafts (below 550 hPa) while moistening continues during that time within the upper-tropospheric ascent region (Houze, 1982). Deep-layer subsidence drying does not occur until after day +10, at about the same time as the WWB (Fig. 3.22). A final characteristic worthy of attention is the episodic vertical q transport in

Fig. 4.3c. These “flame-like” features are generally capped at the 500 hPa level and are suggestive of the attempts of shallow cumuli and cumulus congestus in moistening and heating the lower troposphere. This topic will be discussed in more detail later in this chapter.

The tropical environment in which the MJO exists is one of minute temperature fluctuations. The massive amount of convective latent heat release is primarily balanced in the Tropics by vertical motion and radiative cooling, ultimately resulting in a deep tropospheric overturning and nearly constant temperatures at a given pressure level (e.g., Charney, 1963; Cox and Griffith, 1979). With this in mind, it is not surprising that advective *horizontal* temperature transports $[-(u \frac{\partial T}{\partial x})', -(v \frac{\partial T}{\partial y})']$; cross-sections not shown] are very weak. The tendency equation for T' is derived in Appendix B and may be written as

$$\frac{\partial T'}{\partial t} = -\left(u \frac{\partial T}{\partial x}\right)' - \left(v \frac{\partial T}{\partial y}\right)' - \left(\omega \frac{\partial T}{\partial p}\right)' - \frac{1}{c_p} \left(\omega \frac{\partial \phi}{\partial p}\right)' + \frac{\dot{Q}'}{c_p}, \quad (4.2)$$

where T represents air temperature, c_p the specific heat at constant pressure, ϕ the geopotential, \dot{Q} the rate of heating by radiation, and u , v , and ω the traditional wind components. The composite profiles of the horizontal component of $\frac{\partial T'}{\partial t}$ fail to show any physically-consistent pattern and thus are largely inconclusive. However, vertical motions manifested in adiabatic cooling serve to nearly offset the latent heating within regions of convection. Such cooling is evident in the composite (Fig. 4.4) of the vertical transport component of the anomalous temperature tendency equation (4.2), which combines the effects of upward transport of relatively warmer lower-tropospheric air with the adiabatic cooling process. From Fig. 4.4, we note that adiabatic expansion effects far outweigh the $-(\omega \frac{\partial T}{\partial p})'$ term. The MJO dry phase, a time of deep-layer subsidence warming, is sharply interrupted by strong adiabatic cooling during the intense convection of the wet phase. In the meridionally-averaged framework (Fig. 4.4), a cooling of about 5-6 K/day is noted and must be compensated by latent heating of a similar value. Larger values of cooling are

noted in the individual gridpoint-based case (Fig. 4.5). This convective compensation will be outlined in the next section.

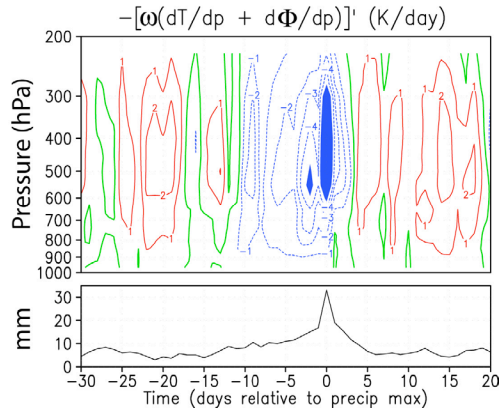


Figure 4.4: Time-height cross-section of total vertical advective contribution to the anomalous time rate of change of temperature $\left[\left(\frac{\partial T}{\partial t}\right)'\right]$ for the meridionally-averaged (10°S - 5°N) framework. The events contained in this composite were selected with use of 20-100-day filtered TRMM rainfall (see text for explanation). The composite timeseries of total precipitation is plotted beneath the cross-section. Solid red lines indicate positive departures from the MJO background state (warming), dashed blue lines represent negative departures (cooling), and thicker green lines the zero contour (see text and Appendix A for details). Blue shading indicates values less than -5 K/day. Lag days are indicated below the rainfall timeseries, with day 0 corresponding to the day of maximum total rainfall. Negative lag days represent those days prior to intense rain.

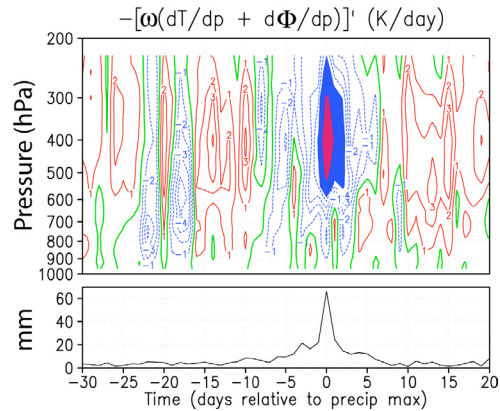


Figure 4.5: As in Figure 4.4, but for the individual gridpoint framework and based on events selected with use of 20-100-day filtered TRMM rainfall (see Section 3.2 for explanation). The corresponding composite timeseries of total precipitation is plotted beneath the cross-section. Contours and shading are identical to those used in Figure 4.4, with the addition that magenta shading indicates values less than -10 K/day.

Thus far we have analyzed the horizontal and vertical components of moisture and temperature advective transport, and how these elements contribute toward perturbations in the time rates of change of q and T . Such transports are critical at all phases of the MJO wave passage. Of particular interest in this paper are the physical mechanisms that occur as

the wave approaches—up to two weeks prior to maximum rainfall—and as the wave departs—up to two weeks following maximum rainfall. Figs. 4.1-4.5 suggest that different transport components have unique impacts on the MJO wave at different stages of the cycle. In terms of q' , the suite of figures indicates that, overall, the change in q' due to vertical motion is more important than that from horizontal flows during the two weeks *preceding* the peak of the wet phase. During this time, particularly near day -10, increases in q' due to rising motion are observed in the lower troposphere while a depletion of q' due to sinking motion is noted in the middle and upper troposphere. These observations alone point toward an enhancement of the shallow cumulus regime. Moisture detrained from these growing clouds is a probable source for the increase in q' within the lower troposphere. The vertical moisture transport of Figs. 4.1-4.3 corresponds to an area of non-zero Q_2' (Fig. 4.9c), indicating that processes not resolved on the ERA40 grid scale (e.g., cumulus activity) are occurring. Maloney and Hartmann (1998; hereafter MH98) conducted an EOF-based composite study of the MJO and found that boundary layer moisture convergence plays a critical role in preconditioning the atmosphere for convection. Our results supporting the importance of vertical cumulus transport of moisture would then complement any local horizontal convergence, aiding in the atmospheric preconditioning.

During the two weeks *following* maximum precipitation, several key differences are evident. As seen in Figs. 4.1-4.3, residual moistening by vertical motion continues up to day +3 and slightly longer above 500 hPa (see Fig. 4.2c). In contrast, lower-tropospheric drying by the horizontal wind begins almost immediately following the intense rainfall. Essentially, the initial decrease in q' 1-3 days after the maximum rainfall may be attributed in part to the horizontal winds. Soon after day +4, deep subsidence drying develops, but this drying due to sinking motion is not maximized until approximately day +12. To highlight these immediate and delayed post-convective drying processes, we present Fig. 4.6. This graphic depicts the combined effects of the horizontal and vertical components that

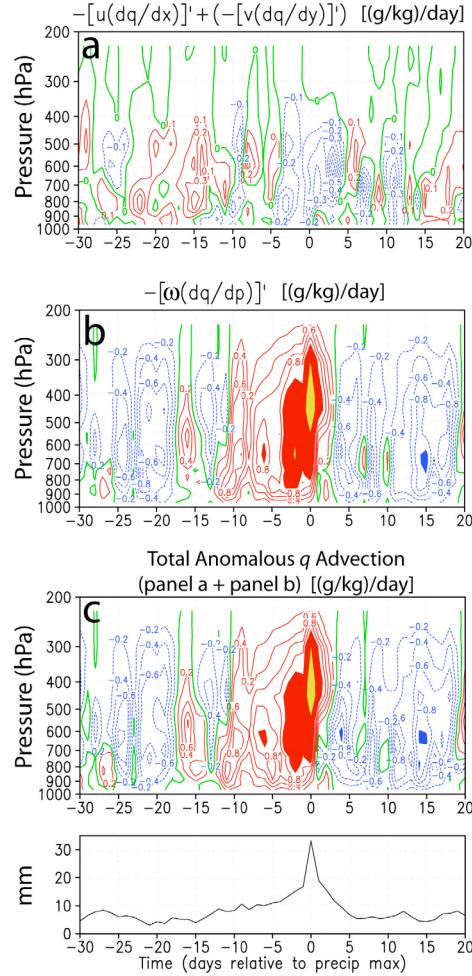


Figure 4.6: Time-height cross-sections of the horizontal (a), vertical (b), and combined (horizontal + vertical) (c) components of the anomalous time rate of change of specific humidity $[\frac{\partial q'}{\partial t}]'$ for the meridionally-averaged (10°S - 5°N) framework. The events contained in this composite were selected with use of 20-100-day filtered TRMM rainfall (see text for explanation). The composite timeseries of total precipitation is plotted beneath panel (c). Solid red lines indicate positive departures from the MJO background state (moistening), dashed blue lines represent negative departures (drying), and thicker green lines the zero contour (see text and Appendix A for details). Blue, red, and yellow shading indicate values less than -1.0 $(g/kg)/day$, between $+1.0$ and $+2.0$ $(g/kg)/day$, and greater than $+2.0$ $(g/kg)/day$, respectively. Lag days are indicated below the rainfall timeseries, with day 0 corresponding to the day of maximum total rainfall. Negative lag days represent those days prior to intense rain.

contribute toward changes in q' for the meridionally-averaged case. Panel (a) displays the strong and immediate drying brought about by the horizontal wind component between day 0 and +5. By comparison with panels (b) and (c), it is clear that the horizontal drying component has an impact on the moisture level, particularly during the first three days following the peak of the wet phase and at a pressure $[\frac{\partial q'}{\partial t}]'$ range of 650-850 hPa. This could perhaps be evidence of a lower-tropospheric dry jet punching eastward behind the intense

convection, with the dry air originating in the subtropics. This topic will be addressed again with the aid of spatial maps in Sections 4.2.2 and 4.2.3. The gridpoint-based results (not shown), a composite of fewer events, are less clear but indeed support the rapid horizontal and delayed vertical drying in the lower troposphere. The concept of immediate and delayed drying mechanisms has not been explicitly discussed in previous studies. MH98 investigate the rapid post-convective drying processes in the context of Rossby wave circulations emanating from the equatorial heat source (as in Gill, 1980). Our results support their findings, that drying is associated with strong lower-tropospheric westerly winds and boundary layer divergence at about two pentads following intense rainfall. We point out, however, that a more immediate drying component is seen in our reanalysis composites, a small-scale feature that might not be seen in the pentad-mean, bandpass-filtered data of MH98.

4.1.2 Convective processes of the MJO (Q_1 and Q_2)

Propagating wave disturbances in the warm-ocean tropical regions tend to be organized in clusters which contain a multitude of individual deep convective cells and span spatial scales of $O(1000 \text{ km})$ (Nakazawa, 1988; see Figure 4.7 for illustration). In this study, the data are available in single gridboxes of $O(100 \text{ km})$, while the deep convective clouds themselves are only several kilometers across. These scale differences generate many questions concerning the relationships between convection and its environment. Do the convective clouds and macro-scale motion systems mutually influence each other? Is it possible to detect the contributions of convective processes based on data sampled from the larger-scale environment? Pioneering work by Yanai et al. (1973) provides answers to these questions in the form of the *apparent heat source* (Q_1) and *apparent moisture sink* (Q_2).

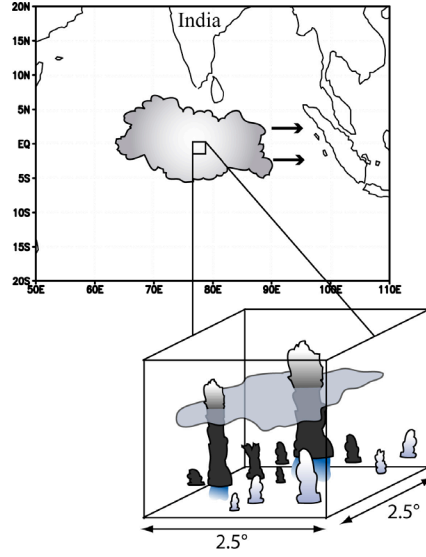


Figure 4.7: Schematic diagram illustrating cloud system scale differences. The larger map (above) depicts an eastward-propagating intraseasonal oscillation (ISO) organized on scales of $O(1000 \text{ km})$. Within a single reanalysis gridbox (e.g., ERA40, $2.5^\circ \times 2.5^\circ$), which itself constitutes a small area of the ISO, an ensemble of convective clouds exists. Deeper convective towers may be “connected” by stratiform or cirriform clouds associated with detrained moisture. A number of shallow cumuli (darker shading) exist underneath the stratiform or anvil clouds and may not be detected by satellite sensors, while others (lighter shading) develop under clearer skies. The apparent heat source (Q_1) and moisture sink (Q_2) account for the contributions of the convective cloud ensemble to the larger-scale environment.

The magnitude of atmospheric heating or cooling brought about by convective processes can be deduced by measuring perturbations in the heat and moisture budgets applied on large scales. Ideally, the budget analysis is conducted on scales that are large enough to contain an ensemble of individual convective clouds and small enough to be only a fraction of the total cloud-cluster area (Emanuel, 1994; see Figure 4.7). The $2.5^\circ \times 2.5^\circ$ ERA40 gridboxes conveniently match the preferred scale size. The equations for Q_1 and Q_2 used in this study are:

$$\frac{Q_1}{c_p} \equiv \left[\frac{\partial T}{\partial t} + \mathbf{v}_h \cdot \nabla_h T + \left(\frac{p}{p_o} \right)^\kappa \omega \frac{\partial \theta}{\partial p} \right] \quad (4.3)$$

$$\frac{Q_2}{c_p} \equiv \frac{-L}{c_p} \left[\frac{\partial q}{\partial t} + \mathbf{v}_h \cdot \nabla_h q + \omega \frac{\partial q}{\partial p} \right] \quad (4.4)$$

where c_p is the specific heat at constant pressure, T is temperature, \mathbf{v}_h the horizontal wind vector, ∇_h the horizontal gradient vector, p the pressure, $p_o = 1000 \text{ hPa}$, κ the ratio of the dry air gas constant R to c_p , ω the pressure velocity, θ the potential temperature, L the

latent heat of vaporization at 0°C, and q the specific humidity. These forms of Q_1 and Q_2 (derivations of which are presented in Appendix C) are adapted from LJ96b. For Q_2 , we employ $q \equiv \frac{m_v}{m_t}$ in substitution of water vapor mixing ratio $w \equiv \frac{m_v}{m_d}$ —where mass of vapor m_v , unit mass of dry air m_d , and $m_t = m_v + m_d$ have been used—but the differences between q and w are at most 1-2%. The concepts of Q_1 and Q_2 were originally designed (Yanai et al., 1973) to analyze data from experiment sounding arrays (e.g., Operation Redwing at the Marshall Islands, Joint Task Force Seven, 1956), in which case each variable would represent an array mean. In the present study, the variables constitute reanalysis gridbox means. In (4.3), Q_1 is a combined measure of heating by radiation (Q_R), net latent heating [$L(c - e)$], and the convergences of three-dimensional eddy transports of sensible heat. In (4.4), Q_2 represents the net latent heating and the convergences of three-dimensional eddy moisture transports (the *horizontal* eddy transports of moisture and sensible heat are typically neglected). Returning to the budgets, if there are non-zero residuals computed from the large-scale budget analyses [RHSs of Eqs. 4.3 and 4.4], these residuals represent the effects of “subgrid-scale” convection on the larger gridbox area. In addition to describing the magnitudes of heating and drying, the relative vertical locations of Q_1 and Q_2 maxima provide information on the type of precipitation (convective vs. stratiform; Johnson and Young, 1983; Luo and Yanai, 1984; LJ96a) and convective intensity, as will be seen shortly.

Climatological (1984-2001) boreal-winter (November-February, “NDJF”) profiles of Q_1 and Q_2 for the Pacific warm pool region appear in Figure 4.8. In panels (a) and (b), dual maxima in the heating rates correspond to convection associated with the double ITCZ pattern that is common during NJDF for the specified geographic region [near Equator, 150°-160°E]. Overall, Q_1 is stronger than Q_2 in a mass-weighted vertical average. Recall that Q_1 here *includes* radiation Q_R , vertical profiles of which are unknown in this analysis.

Recall also that the vertical integral of the quantity $(Q_1 - Q_2 - Q_R)$ is equal to the moist static energy (h) flux at the surface (Yanai et al., 1973). By our estimates, a surface h flux

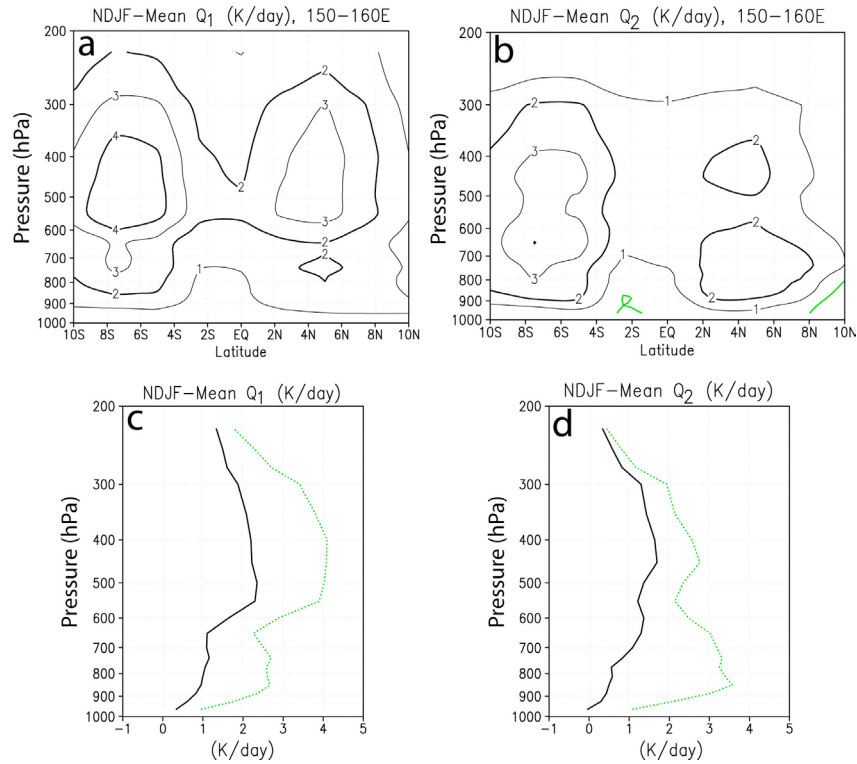


Figure 4.8: November-February (NDJF) climatological-mean (1984-2001) latitude-height cross-sections of the apparent heat source (Q_1 ; a) and apparent moisture sink (Q_2 ; b) averaged from 150°E-160°E (West Pacific warm pool region). Positive contours alternate thin (odd) and thick (even), with thick green line indicating the zero contour. NDJF profiles of Q_1 (c) and Q_2 (d) for the TOGA COARE IFA region (solid black line, 2.5°S 155°E, located between ITCZ cores) and the northern ITCZ core (dotted green lines, 5°N 155°E) are also displayed.

within a reasonable range of previous studies [Yanai et al. (1973), LJ96a] is obtained by assigning a mass-weighted vertical average of Q_R to be approximately -1.1 K/day. In the GARP Atlantic Tropical Experiment (GATE), Q_R mass-weighted vertical averages of about -1.2 to -1.3 K/day were observed (Cox and Griffeth, 1979). The Q_1 and Q_2 peaks are slightly larger in the Southern Hemisphere (rising branch of the Hadley cell) but are located near the same pressure level, indicating a moderate contribution from stratiform precipitation to the total precipitation. In the Northern Hemisphere, the Q_1 peak is near 450 hPa while Q_2 is maximized at 750 hPa. This separation suggests that much of the total

precipitation is due to vigorous convection, and that stratiform processes play a comparatively smaller role in the hydrologic cycle. As mentioned in the previous paragraph, eddy transports factor into Q_1 and Q_2 . Alternate forms of the heating and drying equations are (from Luo and Yanai, 1984):

$$Q_1 - Q_R = L(c - e) - \frac{\partial}{\partial p} \overline{s' \omega'} \quad (4.5)$$

$$Q_2 = L(c - e) + L \frac{\partial}{\partial p} \overline{q' \omega'} \quad (4.6)$$

Here, the horizontal eddy transport terms have been neglected leaving only the vertical eddy transports (final terms on the RHSs of Eqs. 4.5 and 4.6). Within stratiform regions, vertical eddy transports are small and cloud heating occurs at the same pressure level as maximum condensation (the Q_1 and Q_2 peaks are nearly collocated in the vertical). During vigorous convection, vertical eddy transports become important and maximum diabatic heating ($Q_1 - Q_R$) occurs well above the maximum condensation (Q_2), and thus the two peaks are vertically separated (Johnson and Young, 1983; Luo and Yanai, 1984; LJ96a). The profiles presented in Figs. 4.8a and 4.8b are quite similar to those shown in LJ96b (their Fig. 13), with the exception of slightly weaker peak heating rates within the ITCZ cores. This difference might be attributed to the difficulties of remotely sensing the atmospheric layers within deep convection, thus slightly degrading the satellite data used in ERA40.

Profiles of climatological (1984-2001) Q_1 and Q_2 for two geographic points are presented in panels (c) and (d) of Fig. 4.8. The solid black lines match the TOGA COARE Intensive Flux Array (IFA) location (2.5°S, 155°E) and correspond to a region between the double ITCZ rainfall maxima. The dotted green lines represent heating profiles from within the northern ITCZ core (5°N, 155°E). In the IFA region, Q_1 has a relatively flat peak near 500 hPa, while Q_2 is slightly weaker with a broad maximum between 350 hPa and 600 hPa. This vertical structure reflects the relative minimum in precipitation between

the ITCZ cores and the importance of stratiform processes in the IFA region. In contrast, the top-heavy Q_1 profile for the ITCZ core location has a strong peak (4 K/day) at 400 hPa, while Q_2 is maximized at 850 hPa (3.5 K/day). This heating structure clearly indicates the abundance of vigorous convection within the northern ITCZ core (Luo and Yanai, 1984).

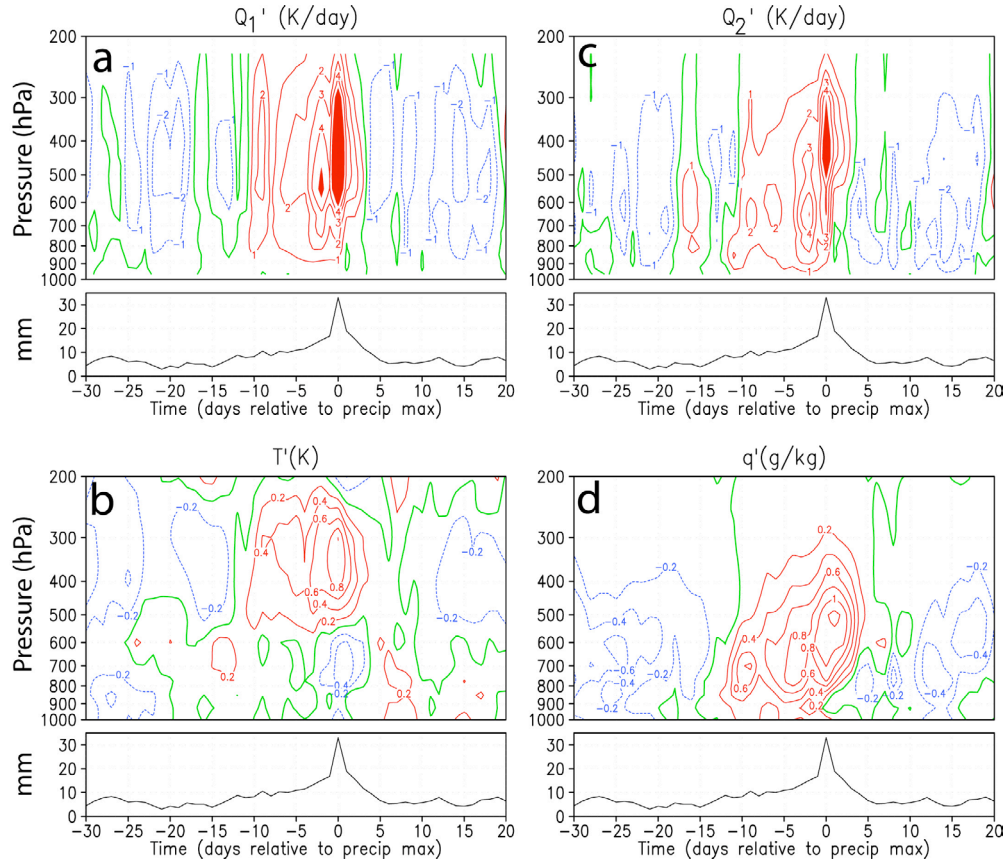


Figure 4.9: Time-height cross-sections of Q_1' (a), T' (b), Q_2' (c), and q' (d) for the meridionally-averaged (10°S - 5°N) framework. The events contained in this composite were selected with use of 20-100-day filtered TRMM rainfall (see text for explanation). The composite timeseries of total precipitation is plotted beneath all panels. Solid red lines indicate positive departures from the MJO background state, dashed blue lines represent negative departures, and thicker green lines the zero contour (see text and Appendix A for details). Red shading indicates values greater than 5 K/day. Lag days are indicated below the rainfall timeseries, with day 0 corresponding to the day of maximum total rainfall. Negative lag days represent those days prior to intense rain.

Composite cross-sections of Q_1' , T' , Q_2' , and q' for the meridionally-averaged framework appear in Figure 4.9 (panels a, b, c, and d, respectively). The T' and q' profiles are identical to those shown in Figs. 3.12 and 3.13. As was mentioned in Section 4.1.1, adiabatic cooling associated with strong vertical motions in the middle troposphere must be balanced by convective warming, primarily in the form of latent heat release and radiative

effects. To within 1 K/day, this balance is achieved, as clearly seen by a comparison of the convective heating (Fig. 4.9a) and adiabatic cooling anomalies (Fig. 4.4). In the remainder of this section, we will review the general features of these heating and drying profiles and briefly touch on the basic physical mechanisms implied by the data. A detailed discussion of the physical connections between the structure of the data and MJO cloud processes is presented in Section 4.2.1.

During the convectively-suppressed phase of the MJO, a mix of lightly-precipitating and non-precipitating shallow cumuli exist (DeMott and Rutledge, 1998; LJ96b). Their signature is reflected in Fig. 4.9a and 4.9c, particularly prior to day -20, where there is weak heating and drying below ~ 750 hPa and general anomalous cooling and moistening above this level. Radiative emission to space ($Q_R < 0$, one factor contributing to Q_1') is the likely source of the mid- and upper-tropospheric cooling during the suppressed stage. Vertical growth and increased intensity of the low-level cumuli are apparent between days -15 and -10 as Q_1' and Q_2' values become elevated. Simultaneously, $T' > 0$ and $q' > 0$ below ~ 550 hPa. Around one week prior to the maximum rainfall, deep convection has developed as suggested by the separation of the Q_1' and Q_2' peaks. Convective precipitation culminates a few days before maximum *total* rainfall intensity as evidenced by the vertically-separated peaks of Q_1' and Q_2' during this time. This total precipitation maximum is associated with both convective and stratiform processes owing to the nearly collocated Q_1' and Q_2' peaks at 450 hPa. From day +2 to +5, the cooling and moistening observed in the middle to lower troposphere presumably corresponds to the evaporation of stratiform precipitation (LJ96b). As was discussed in Section 4.1.1, however, this is also a time of moderate drying influences by the low-level horizontal wind, a process that likely contributes toward the more rapid drying below 700 hPa as is seen in Fig. 4.9d. The suppressed stage of the MJO gradually resumes after day +5, with negative anomalies of Q_2 signaling a lack of precipitation.

Many of the same features outlined in the meridionally-averaged framework also appear in the individual gridpoint-based composites (see Fig. 4.12). Figure 4.12(p-s) displays the heating and moistening profiles for the composite derived using a 10-100-day filter and small search area (see Chapter 2). This composite is qualitatively similar to that computed using the 20-100-day filter and larger search area but contains more individual events and is less noisy. As in the meridionally-averaged case (Fig. 4.9), Fig. 4.12(p-s) portrays the extensive deep-layer radiative cooling and mostly non- or weakly-precipitating shallow cumuli 2-4 weeks prior to maximum rainfall. Between days -15 and -5, low-level heating episodically grows toward the middle troposphere as a change from moistening to drying occurs below 600 hPa. This structure likely signifies the transition of shallow cumuli (light precipitation) to mid-level cumuli and cumulus congestus (increasing precipitation). The robust convection and stratiform signatures appear similar to those in Fig. 4.9, particularly between days -3 and +3, and are again followed by a gradual return to the suppressed MJO phase.

4.2 Putting It All Together

A number of characteristic physical processes, introduced and briefly discussed thus far in Chapter 3 and Section 4.1, are noted in the ERA40 and MODIS datasets for periods of heightened MJO wave activity. Which mechanisms are important during the growth and decay stages of the MJO wet phase, and how do these atmospheric and oceanic components ultimately generate, maintain, and quell intense convection? With the aid of composite profiles and spatial map sequences, we now highlight and summarize the key features of this tropical phenomenon—particularly the approach and departure of the wet phase—in Sections 4.2.1, 4.2.2, and 4.2.3.

4.2.1 Driving heat and moisture variances

Wave generation, amplification, and maintenance require an energy source. In the midlatitudes, this source may be supplied from strong zonal jets and baroclinic instability associated with large horizontal thermal contrasts. Since such jet stream activity and horizontal T contrasts are not typically found in the tropics, an alternative source—the generation of eddy available potential energy (EAPE) and its conversion to eddy kinetic energy (EKE) due to *localized* heating and moistening—feeds tropical waves. EAPE is associated with increases in T variance and is increased when $Q_1' T' > 0$ [“heating where it is hot, cooling where it is cold” (Lorenz, 1955)].

Vertical profiles of $Q_1' T'$ and $-Q_2' q'$ averaged over the entire composite MJO event (days -30 to +20) appear in Figure 4.10. Averaged time *segments* of $Q_1' T'$ and $-Q_2' q'$ during pre-convective, convective, and post-convective MJO periods for the gridpoint-based framework are presented in Figure 4.11. We chose to show the gridpoint-based

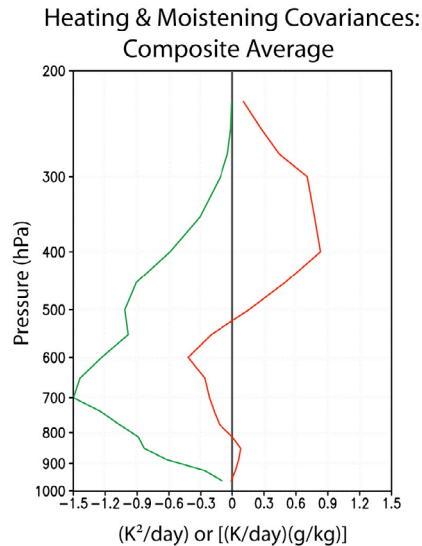


Figure 4.10: Vertical profiles of heating ($Q_1' T'$; red line) and moistening ($-Q_2' q'$; green line) averaged over the entire MJO composite event based on the individual gridpoint framework. The entire MJO composite event constitutes lag days -30 to +20. The events contained in this composite were selected with use of 10-100-day filtered TRMM rainfall (see text for explanation). The units of $\overline{Q_1' T'}$ are (K^2 / day) while those of $\overline{-Q_2' q'}$ are $[(K/day)(g/kg)]$.

composite rather than that of meridional averaging because, although the two qualitatively share similar features, the latter has far smaller magnitudes owing to the averaging process. From Fig. 4.10, we see that there are distinct differences between the heating and moistening covariance components. Below 800 hPa and above 500 hPa, Q_1 (diabatic and radiational heating) drives temperature variances and thus acts as a source of EAPE when averaged over the duration of the MJO lifecycle. The time-averaged heating covariance reaches a minimum near 600 hPa, likely a result of the strong convective heating of rain-cooled air around day 0 (this is verified in Figs. 4.9a and 4.9b). Q_2 , in contrast, works to minimize q variance throughout the troposphere, tending to moisten dry air and dry moist air.

We will now focus on Fig. 4.11 and previous composite plots to review the key features of the MJO wave passage as observed in the ERA40 and MODIS datasets, with particular emphasis on the wet phase approach and departure. References to the “basic” variable features (3D winds, T , q , SLHF, OLR, etc.) will appear many times throughout the following discussion. For simplicity (and unless otherwise noted), the references are directed toward Figure 4.12 only. The gridpoint composite based on the 20-100-day filter (e.g., Fig. 3.22), while it shares similar characteristics with the composite based on the 10-100-day filter (Fig. 4.12), contains fewer events and is more susceptible to spurious features not directly associated with the MJO (e.g., the convective impulse near day -20 in Fig. 3.24).

Suppressed/undisturbed stage (days -30 to -15). During the period 2-4 weeks prior to the most intense rainfall, deep, vigorous convection is suppressed largely due to abundant dryness and widespread subsidence. Lightly-precipitating shallow cumuli with warmer-than-freezing cloud tops exist, and precipitation is at a minimum. Weak easterly wind anomalies in the lower to middle troposphere (Fig. 4.12a) support relatively weak ocean-atmosphere fluxes and attendant weak ocean mixing (hence an “undisturbed” ocean). This, combined with strong shortwave absorption at the surface (SSA) and above-normal OLR, results in increasing SST’ with time (Fig. 4.12j). Precipitable water (PW) is at a minimum;

dry anomalies exist at all levels and are most negative at 600-750 hPa (Fig. 4.12e). Anomalous cool air is noted above 500 hPa and in the lower troposphere, while a weak warm layer persists at mid-levels (500-800 hPa; Fig. 4.12d). From Fig. 4.11a, we can deduce the physical mechanisms likely associated with the observed atmospheric conditions during the suppressed phase (dotted purple lines). Above 450 hPa in Fig. 4.11a, $\overline{Q_1' T'}$ is positive and *relatively large* (feature marked “1”), indicating cooling of the observed anomalously-cool air. Because advective and convective processes do not appear to be active at this time and altitude (e.g., Fig. 4.12c), we can infer that radiational cooling is the leading Q_1' component increasing T variance. At mid-levels, cooling ($Q_1' < -1$ K/day; Fig. 4.12p)

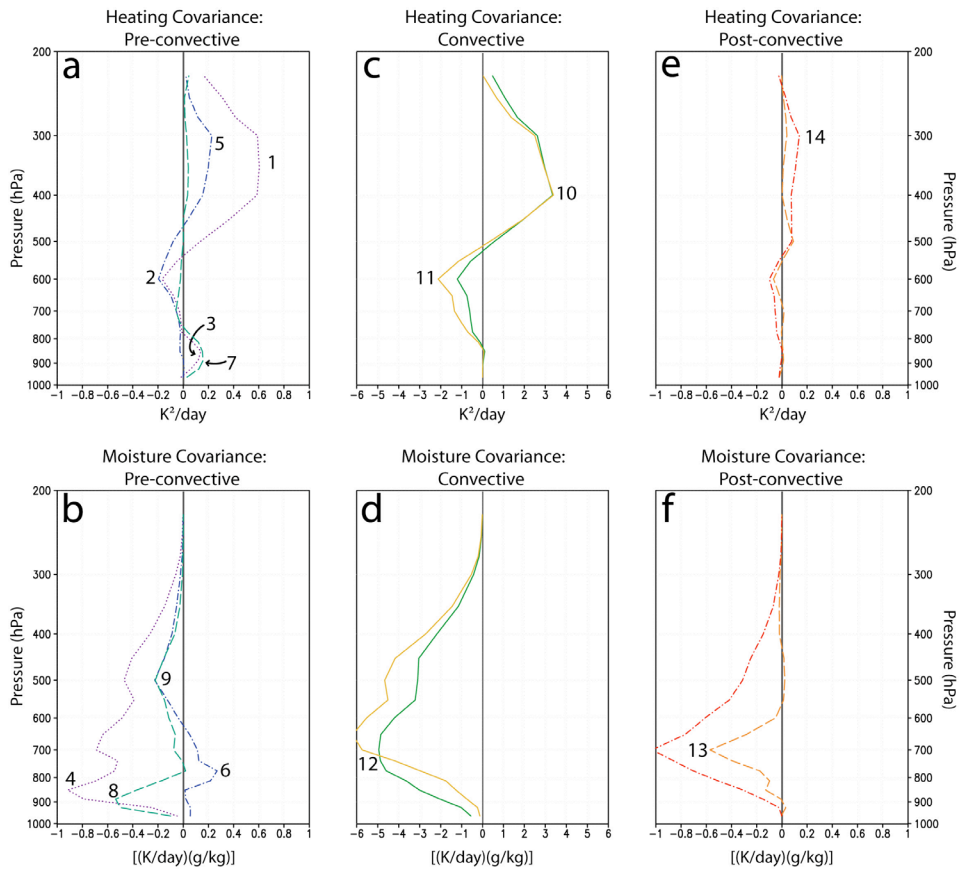


Figure 4.11: Vertical profiles of heating ($Q_1' T'$; top row) and moistening ($-Q_2' q'$; bottom row), averaged over pre-convective (left column), convective (middle column), and post-convective (right column) MJO stages for the gridpoint-based framework. The events contained in this composite were selected with use of 10-100-day filtered TRMM rainfall (see text for explanation). Profiles are represented by dotted purple lines (days -30 to -15), dash-dot blue lines (days -15 to -10), dashed aqua lines (days -10 to -5), solid green lines (days -5 to 0), solid light-orange lines (days 0 to +5), dashed orange lines (days +5 to +10), and dash-dot red lines (days +10 to +20). Numbers indicate physical features that are discussed in the text.

extends down to ~600 hPa, which approximately coincides with the top of the warm, dry layer (inversion; Fig. 4.12r). We therefore presume that the 600-hPa minimum in $\overline{Q_1' T'}$ (“2” in Fig. 4.11a) corresponds to radiational cooling from near the inversion top. Below 800 hPa, there is cooling [“3” in Fig. 4.11a] and moistening [“4” in panel (b)] of cool, dry air, possibly the signature of evaporation from lightly-precipitating shallow cumuli. During the suppressed phase, $\overline{-Q_2' q'} < 0$ throughout the entire troposphere, indicating that q'^2 is diminishing with time (Fig. 4.11b).

End of suppressed phase (days -15 to -10). An enhancement in the effectiveness of lower-tropospheric moistening by shallow cumuli, likely due to an increase in their number and coverage as evidenced by the decline in anomalous surface shortwave absorption (SSA'; Fig. 4.12j), heralds the end of the suppressed phase. The more widespread coverage of shallow cumuli is also reflected in the profiles of ω' , T' , and q' , with a trend toward more negative values of ω' and more positive values of T' and q' in the lower troposphere (panels c, d, and e of Fig. 4.12, respectively). During this stage, there are comparatively sharp declines in MSLP' and CTP, but deep convection remains isolated and precipitation rates light. Moderate lower- to mid-tropospheric easterly wind anomalies (Fig. 4.12a) continue and maintain steady, weak surface fluxes, resulting in a maximum of SST' near day -10 (Fig. 4.12j). The heating and moistening covariance profiles (dot-dashed blue lines in Figs. 4.11a and 4.11b, respectively) suggest that radiative cooling (“5”), albeit weaker, continues above 450 hPa. Weak radiational cooling (“2”) from the top of the mid-level warm (and progressively more moist) layer also persists. Between 650 hPa and 800 hPa, detrainment from shallow cumuli has moistened and continues to moisten the layer. This observation, combined with only a minimal increase in precipitation, aids in increasing q variance at low levels (“6” in Fig. 4.11b). Collectively, mid- and upper-level radiational cooling, elevated SSTs, and low-level heating and moistening effectively increase convective available potential energy (CAPE), thus destabilizing the atmosphere and precondition-

ing the region for an impending intensification of convection (e.g., K-CW01). These features lend support to the discharge-recharge theory, rather than stratiform instability. Details will be discussed in Section 4.2.4.

Approaching fringes of the wet phase (days -10 to -5). This stage is characterized by the increasing coverage, intensity, and vertical growth of cumulus clouds. Upward vertical motions and positive temperature and moisture perturbations become elevated and rapidly extend toward the upper troposphere as deep convection becomes more active (panels c, d, and e of Fig. 4.12, respectively). After a brief lull in rainfall, precipitation rates trend upward and are associated with a warming and drying at low levels. At this time, easterly wind anomalies become slightly stronger with upper-level westerly anomalies becoming more prominent (Fig. 4.12a). Ocean surface fluxes remain at or below normal, yet SST' steadily decreases from its peak as SSA' and OLR' gradually fall. The start of a broad pressure minimum occurs during this phase, and PW and cloud-top heights increase as low-level moisture is advected upward (see Fig. 4.12n for advection). Several interesting features are noted in the day -10 to -5 covariance profiles (dashed aqua lines in Figs. 4.11a and 4.11b). Although there is little activity above 400 hPa, low-level convective heating of warm, moist air ("7", $\overline{Q_1' T'} > 0$) below 750 hPa drives T variance and helps in the intensification of convective clouds. Simultaneously, the enhanced condensation rate (i.e., rainfall production) by growing cumuli dries the atmosphere below 800 hPa ("8" in Fig. 4.11b), while these same clouds continue to detrain vapor into the overlying dry layer near 500 hPa (see Fig. 4.12e), preparing the atmosphere for deep convection as in the discharge-recharge theory.

Onset of convective wet phase (days -5 to 0). Convective precipitation and anomalous vertical moisture transport are greatest within the 5 days preceding the maximum *total* rainfall rate, as evidenced by the separated Q_1' and Q_2' peaks (Figs. 4.12p and 4.12q, respectively). Leading up to day 0, low-level westerly wind anomalies rapidly replace

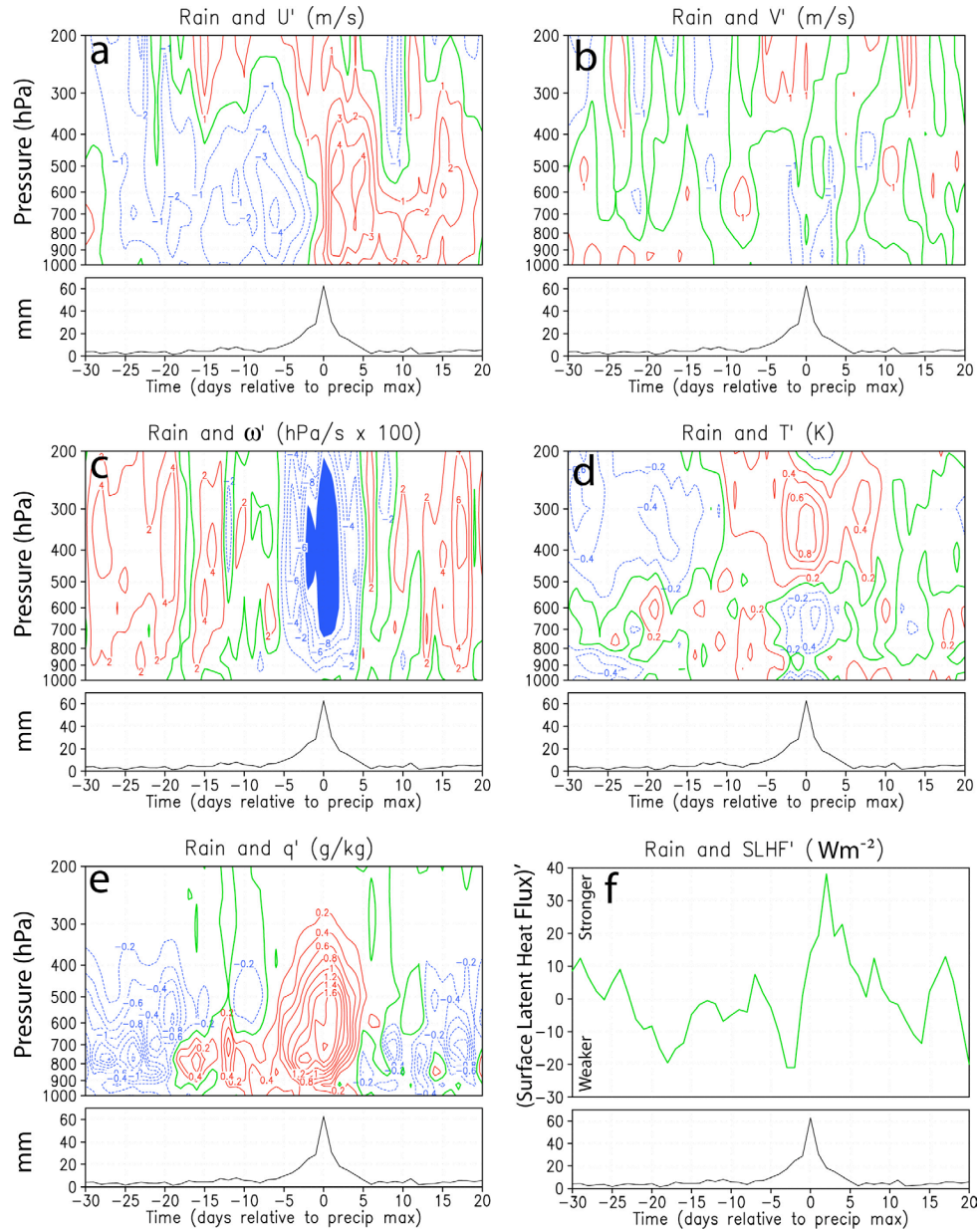


Figure 4.12: Time-height cross-sections of zonal wind (u' , a), meridional wind (v' , b), pressure velocity (ω' , c), temperature (T' , d), and specific humidity (q' , e) anomalies as well as the timeseries of surface latent heat flux anomalies ($SLHF'$, f) for the composite MJO event based on the individual gridpoint framework. The events contained in this composite were selected with use of 10-100-day filtered TRMM rainfall (see text for explanation). The composite timeseries of total precipitation are plotted beneath all panels. Solid red lines indicate positive departures from the MJO background state, dashed blue lines represent negative departures, and thicker green lines the zero contour (see text and Appendix A for details). Blue shading in panel c represents values less than -0.1 hPa/s ($\times 100$). Lag days are indicated below the rainfall timeseries, with day 0 corresponding to the day of maximum total rainfall. Negative lag days represent those days prior to intense rain.

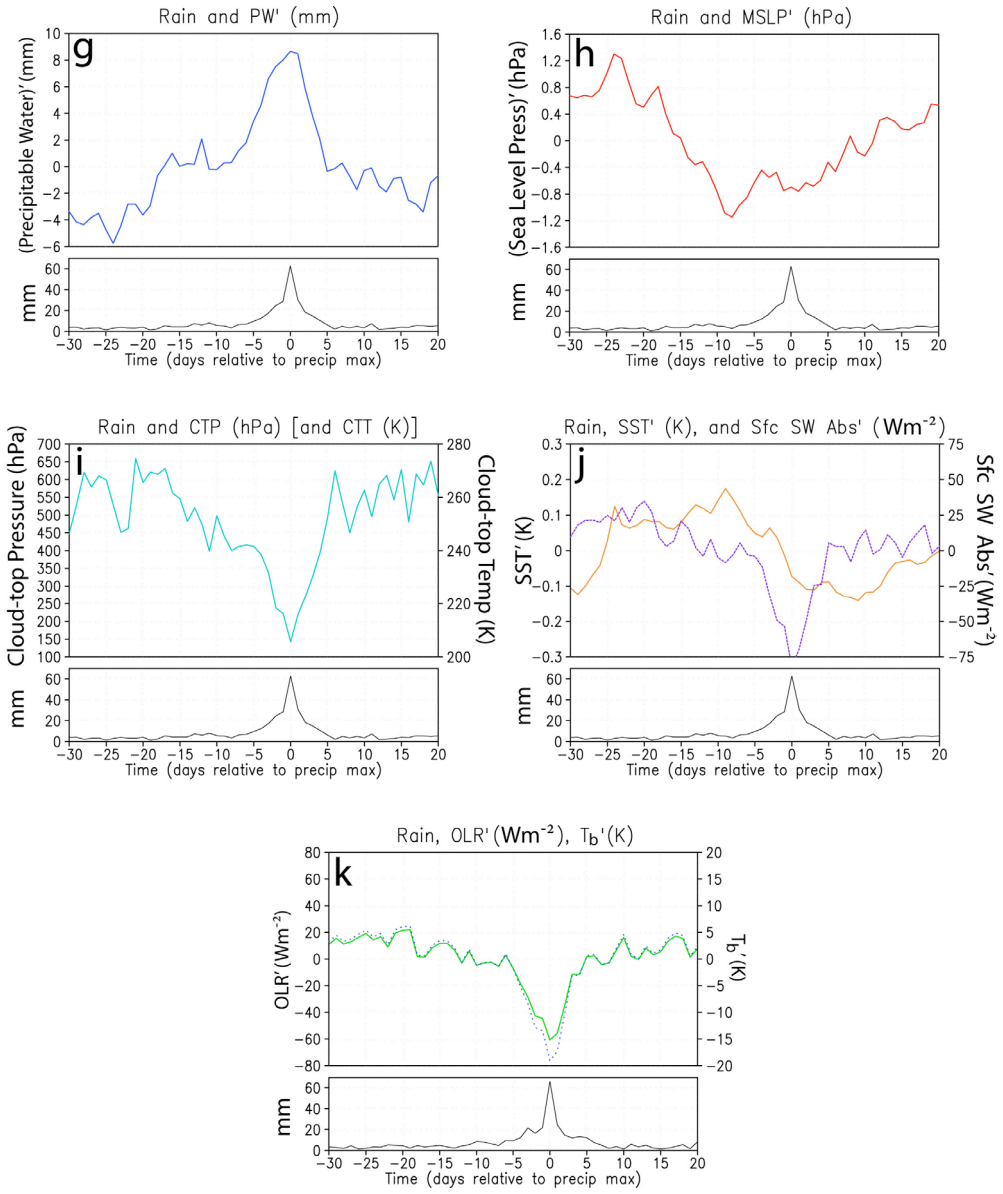


Figure 4.12 (continued): Composite timeseries of the departures of precipitable water (PW' , g), mean sea-level pressure ($MSLP'$, h), MODIS-derived cloud-top pressure (CTP, i; cloud-top temperature CTT also indicated at right), sea-surface temperature (SST' , solid orange line in j) and solar radiation absorbed at the surface (SSA' , or "Sfc SW Abs"; dotted purple line in j), and outgoing longwave radiation (OLR' , solid green line in k) and brightness temperature (dotted blue line in k) from the MJO background state for the individual gridpoint framework.

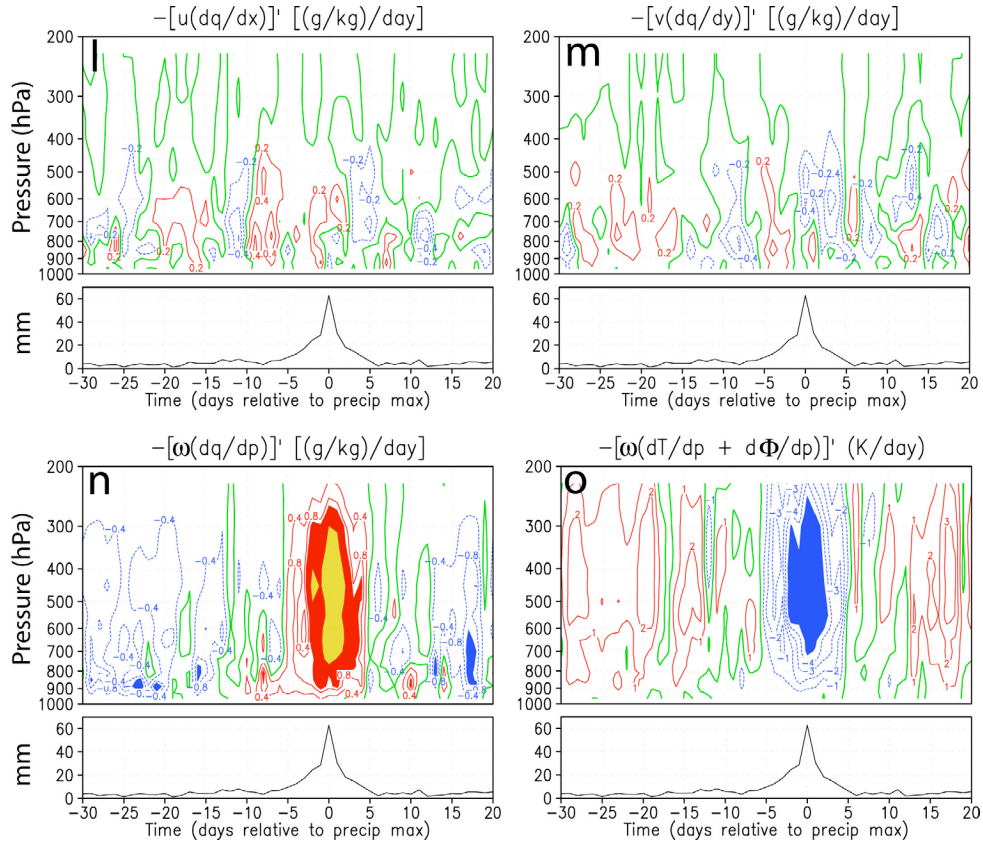


Figure 4.12 (continued): Time-height cross-sections of the zonal (l), meridional (m), and vertical (n) components of the anomalous time rate of change of specific humidity $\left[\left(\frac{\partial q}{\partial t}\right)'\right]$ as well as the total vertical advective contribution to the anomalous time rate of change of temperature $\left[\left(\frac{\partial T}{\partial t}\right)'\right]$ for the individual gridpoint framework. Blue, red, and yellow shading in panel (n) indicates values less than -1.0 (g/kg)/day, between $+1.0$ and $+2.0$ (g/kg)/day, and greater than $+2.0$ (g/kg)/day, respectively. Blue shading in panel (o) represents values less than -5 K/day.

easterly anomalies and continue to intensify (Fig. 4.12a). From the structure of lower-tropospheric wind anomalies, we infer that this stage is also the time of greatest low-level convergence, in partial support of a wave-CISK-like mechanism (see Section 4.2.4). Additionally, for the first time in the MJO lifecycle, meridional wind anomalies become active and blow weakly from the north (Fig. 4.12b). Owing to the enhanced near-surface wind anomalies, $SLHF'$ begins to increase rapidly on day -1 (Fig. 4.12f). During this stage, pressure minimums are reached, and PW' and cloud-top heights climb to their highest levels as SSA' and OLR' drop to their most negative values. The enhanced cloud coverage and thickness, as well as the rapidly-increasing precipitation rate, causes a sharp

decline in SST (Fig. 4.12j). Concerning moisture, maximum q rises from 750 hPa on day -3 to ~600 hPa on day 0 and continues upward. Also near day 0, mesoscale, stratiform precipitation processes begin to gain importance and are reflected in the cooling trend below 500 hPa (a result of evaporation and melting within the mesoscale downdrafts; see Section 4.2.4). At this time, competing upward vertical velocities are maximized in the middle troposphere near 400 hPa (Fig. 4.12c), just below the peak in positive temperature anomaly (~0.9 K, day 0; Fig. 4.12d). From Fig. 4.11c and 4.11d, we see immediately that the heating and moistening covariance magnitudes during the height of the wet phase are many times larger than those of pre- or post-convective periods (note the horizontal axis differences). The green lines in panels (c) and (d) represent such profiles for the convective wet phase (days -5 to 0). In panel (c), cloud heating efficiently drives T variance in the upper troposphere, especially near 400 hPa (“10”), while T variance is diminished in the mid-troposphere due to convective heating of rain-cooled air (“11”). Between 600 hPa and 800 hPa, $-\overline{Q_2' q'}$ is large and negative due to the rapid and widespread conversion of vapor to liquid (condensation). Not surprisingly, this observation supports the jump of total precipitation intensity just prior to day 0.

Transition to stratiform wet phase (days 0 to +5). During this transition stage, stratiform precipitation processes persist as robust convection gradually dissipates. A westward tilt with height is indicated by the maximum in upper-level divergence, which appears to lag low-level convergence by 3-5 days (see u' gradient in Fig. 4.12a). While once confined mainly to the lower troposphere, the Q_2' peak slowly rises and elongates vertically to partially merge with the Q_1' maximum (see Figs. 4.12p and 4.12q), signaling the stratiform trend. Additionally, the T' minimum (650 hPa) follows T' maximum (350 hPa) by 1-4 days and indicates evaporative cooling from stratiform precipitation (see Fig. 4.12d). Vertical velocities diminish toward zero as mid- and lower-level mesoscale downdrafts become more extensive and further counter dissipating convective updrafts (see Fig. 4.12c). The

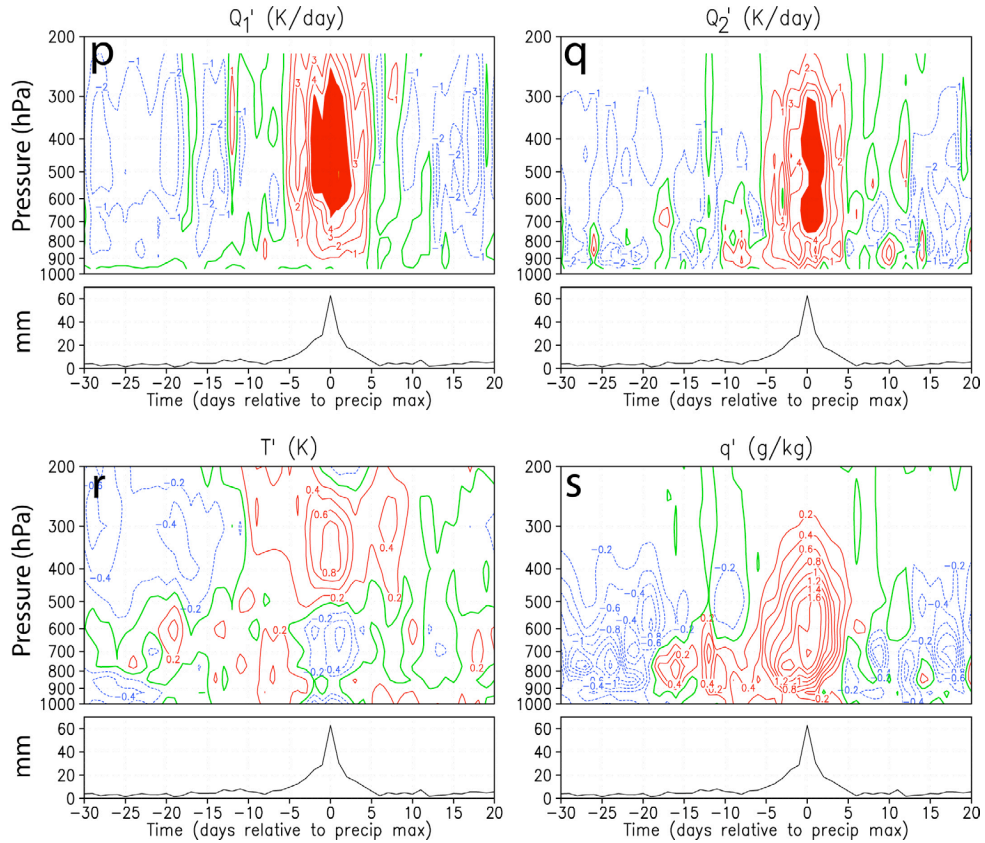


Figure 4.12 (continued): Time-height cross-sections of Q_1' (a), T' (b), Q_2' (c), and q' (d) for the individual gridpoint framework. Red shading indicates values greater than 5 K/day.

residual upward motions on days +2 to +4 may reflect convective updrafts triggered by a reduction in convective inhibition (CIN) associated with stratiform instability (see Section 4.2.4). From profiles of T' and q' , we note that the mid-level cooling and moistening due to stratiform processes can continue well beyond day +5 (e.g., Fig. 4.12d). Surface westerly winds peak during or 1-2 days following the maximum total rainfall and accompany the strong $SLHF'$ spike, as SST' continues its steady decline. It is important to note that moderate, nearly immediate drying by the horizontal wind initially counters residual vertical moistening and aids in decreasing q' at low levels (e.g., Fig. 4.6a). Deep-layer subsidence drying is not active during this stage of the MJO lifecycle (Fig. 4.12c). This horizontal drying by the initial westerly wind anomalies has not been strongly emphasized in the

literature but may be an important component in the MJO lifecycle. Between days 0 and +5, PW' and cloud-top heights sharply decrease, OLR' and SSA' rapidly increase, and MSLP slowly begins to rise. From Figs. 4.11c and 4.11d (yellow lines), most of the heating and moistening features (“10”-“12”) are nearly identical to those of the previous (“convective”) stage. Mid-level cooling combined with steady convective heating results in a noticeably larger $|\overline{Q_1' T'}|$ at 600 hPa (“11”), however. In addition, the most intense drying (condensation; as seen in $-\overline{Q_2' q'}$) shifts upward and is uniformly greater in magnitude than that of the previous stage between 700 hPa and 400 hPa, supporting the observed rise in the Q_2' peak (see Fig. 4.12q).

Departing fringes of wet phase (days +5 to +10). Total rainfall intensity returns to “suppressed-phase” values between days +5 and +10 as stratiform precipitation processes slowly end and only extremely isolated deep convection is present. Surface westerly and upper-tropospheric easterly wind anomalies remain steady (Fig. 4.12a), yet SLHF perturbation magnitudes are temporarily reduced ahead of the westerly wind burst (WWB). The development and slow strengthening of deep-layer subsidence contributes to a general decrease in q' , and PW' and cloud-top heights continue to slowly decrease as the troposphere dries. Surface pressures steadily rise as the main convective disturbance departs to the east, and SSA and OLR return to background levels. Tropospheric heating covariances are very weak during this time (dashed orange line in Fig. 4.11e). In the moisture covariance profile [same line in Fig. 4.11f], a moderate negative peak near 700 hPa (“13” in Fig. 4.11f) arises during a transitional period in which residual condensation (drying of moist air) evolves into a moistening of dry air through evaporation. In both of these “sub-stages”, q variance is reduced.

Returning to the suppressed phase (days +10 to +20). After day +10, deep convection is stifled by potent vertical shear associated with the WWB (Figs. 3.22 and 4.12a), the return of anomalously dry air (particularly at 600-800 hPa; Fig. 4.12e), and strong environ-

mental subsidence (Fig. 4.12c). Several studies have suggested that this dry air may have its origins in the subtropics (Numaguti, 1995; DeMott and Rutledge, 1998 and references therein). This topic will be discussed further in Section 4.2.3. During this stage, towering convection has “died out,” and like the cataclysmic extinction 65 million years ago, the only entities remaining (shallow cumuli) in the aftermath of the event are those that require minimal resources (small amounts of boundary layer heat and moisture) for sustainability. The highlight of this stage is the WWB, typically observed between days +10 and +15. WWBs, as seen in Figs. 3.22 and 4.12a, are usually associated with strong, deep-layer subsidence, maximum tropopausal easterly wind anomalies, a secondary peak in SLHF', and the transport of dry air on WNW winds (LJ96b). The westerly anomalies generally peak at 650-800 hPa and tend to occur near or just after the minimum in SST', according to the ERA40 composites. That the SST' minimum can occur *before* the WWB seems counter-intuitive, considering ocean surface fluxes (which are a major factor modulating SSTs) are maximized *during* the WWB. In defense of this feature, the SSA' timeseries indicates that surface solar absorption returns to average values by day +5, and this would oppose ocean cooling during the WWB. Nonetheless, we are hesitant to make any meaningful deductions based on this feature in the SST' composite, as it is unclear whether it is truly physical or an ERA40 model deficiency. Several studies (e.g., LJ96a) have reported that WWBs may be associated with residual cirrus coverage; this issue will be addressed in Section 4.2.3. The intensified ocean-atmosphere fluxes brought on by the WWB act to warm the lower troposphere below 850 hPa, while lightly-precipitating shallow cumuli develop and contribute toward weak, localized drying. The heating and moistening covariance profiles for this stage (dot-dashed red lines in Figs. 4.11e and 4.11f, respectively) indicate a weak and gradual increase of T'^2 (“14”) due to upper-level radiative cooling (~300 hPa; Fig. 4.12p). In general, the heating covariances are small because $T' < 0.2$ K throughout most of the troposphere. Moistening of very dry air, particularly near 700 hPa, results in a nega-

tive peak of $-\overline{Q_2' q'}$ at this level and is reminiscent of the profile structure for the pre-convective suppressed phase (dotted purple line in Fig. 4.11b).

4.2.2 Spatial composite, gridpoint-based

The composite cross-sections presented thus far provide detailed information about the temporal and vertical variability of an MJO wave passage. To gain a flavor of the *horizontal* spatial characteristics of the tropical disturbance, we display a composite time sequence of maps (Figure 4.13) centered on the geographic location of the maximum total rainfall (corresponding to day 0). The map sequences are based on a composite of nine individual MJO events selected using a 20-100-day filter and large search area (see Chapter 2). The data that appear, however, are 3-day running averages of *unfiltered* composite departures from an 18-year calendar-day mean. These anomalies are slightly different than those used in the composite cross-sections of Section 3.4. Because the day-0 geographic point (hereafter the “origin point” and circled in each panel of Fig. 4.13) may be located in either the Northern or Southern Hemisphere (recall that the latitudinal domain is approximately 10°S-5°N; see Fig. 3.21) and at various longitudes along the tropical band, care must be taken when interpreting the results, particularly with respect to cyclones, anticyclones, and cross-equatorial flows. Figure 4.13 is meant only to shed some light on the *qualitative* spatial features and their time evolution in the context of the MJO.

Three-day averaged rain and 850 hPa horizontal wind anomalies [\mathbf{v}_h' ; column (a)]; OLR' and 200 hPa \mathbf{v}_h' (b); q' and \mathbf{v}_h' at 600 hPa (c); and ω' and \mathbf{v}_h' at 600 hPa (d) for lag days -15, -5, 0, +5, and +12 are displayed in Fig. 4.13. Hereafter, q' and ω' at 600 hPa will be written q_{600}' and ω_{600}' , respectively. On day -15 during the end of the convectively-suppressed phase, precipitation surrounding the origin point is light and sporadic; low-level (600 hPa and 850 hPa) \mathbf{v}_h' are light and easterly and underlie strong, meridionally-convergent westerly \mathbf{v}_h' at 200 hPa; OLR' > 0; $q_{600}' < 0$; and $\omega_{600}' > 0$ (sinking

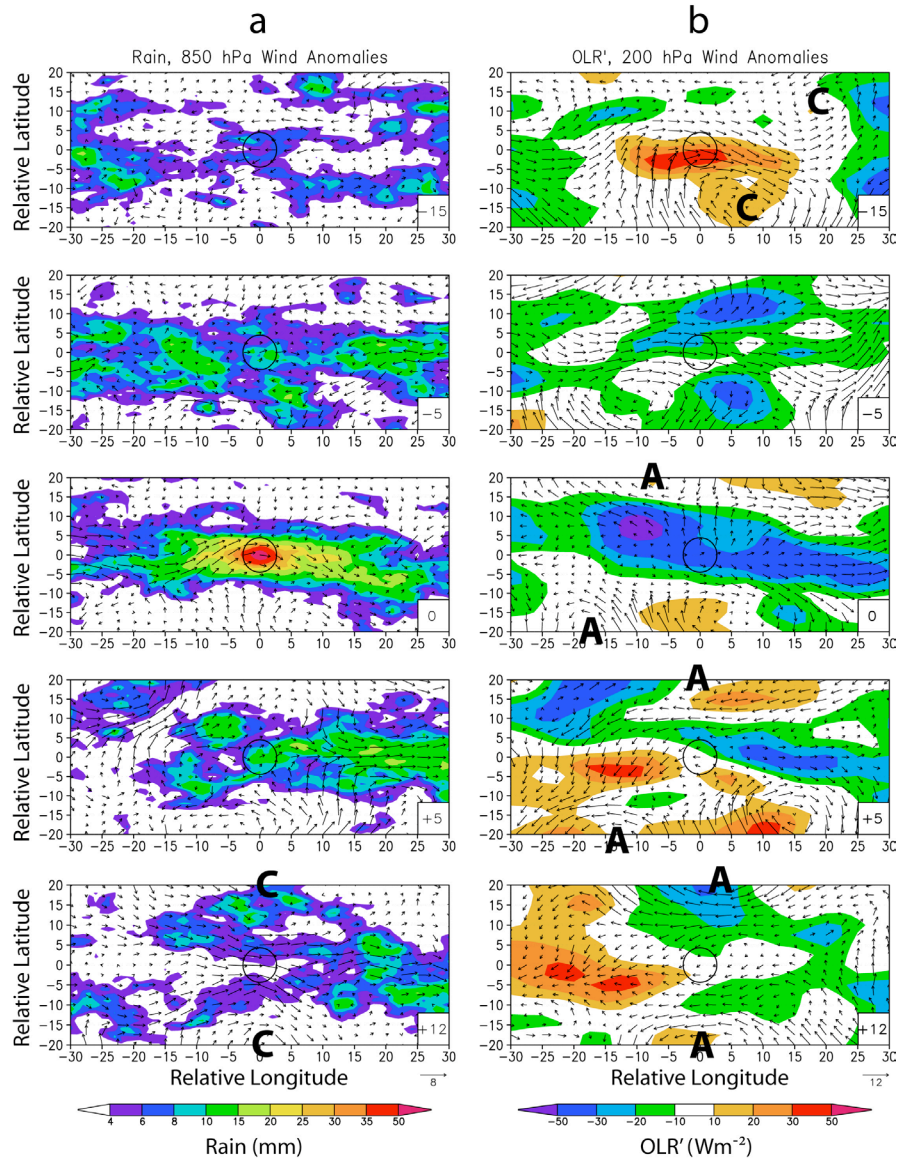


Figure 4.13: Composite map sequences of TRMM total rainfall and $\mathbf{V}_{850 \text{ hPa}}'$ (column a), and OLR' and $\mathbf{V}_{200 \text{ hPa}}'$ (column b) for the individual gridpoint framework. The events contained in this composite were selected with use of 20-100-day filtered TRMM rainfall (see text for explanation). Anomaly values represent departures from the climatological mean (1984-2001) and not the MJO background state. Lag days are located in the lower-right corner of each panel. Maximum wind vector magnitudes (m/s) appear just above and right of the color scales at the bottom of each column. The zero lag day corresponds to the day of maximum total rainfall at the 0 longitude/0 latitude point (the “origin point”, circled in each panel). It is important to note that the zero latitude line does *not* correspond to the Equator but rather is *relative* to each event in the composite. Letters “A” and “C” represent anticyclonic and cyclonic gyres as discussed in the text.

motion). In the 200 hPa \mathbf{v}_h' field, cyclonic gyres (marked “C” in Fig. 4.13b, day -15) are noted to the southeast and northeast of the origin point. At 850 hPa, easterly anomalies at the zero latitude are flanked by weak poleward flows, suggesting near-surface divergence

and tropospheric subsidence. These features are similar to those found by Hendon and Salby (1994, hereafter HS94), who constructed maps of 35-95-day filtered upper- and lower-tropospheric variables.

By day -5, rainfall has increased across the zero latitude band. Inspection of the precipitation patterns during days -4 through -1 (not shown) clearly indicates the rainfall disturbance approaching from the west, despite a local maximum positioned at [0° lat, +20° lon (of origin point)] on day -5. Weak, meridionally-convergent, westerly \mathbf{v}_h' in the lower-troposphere; strong zonal westerly \mathbf{v}_h' at 200 hPa; $OLR' < 0$; $q_{600}' > 0$; and $\omega_{600}' < 0$ are observed and suggest a transition from the dry phase to the wet convective stage of the MJO. Between days -5 and 0, plots of $SLHF'$ and \mathbf{v}_h' at 1000 hPa (not shown) indicate only a small increase in ocean-atmosphere fluxes and weak *westerly* wind anomalies, suggesting that, at least for most of the individual events in this composite, the WISHE mechanism does not appear to play a substantial role in MJO wave development. This topic will be discussed more in Sections 4.2.3 and 4.2.4.

The maximum total precipitation rate is observed on day 0 at the origin point (by construction) and is organized in a latitudinal band approximately 20° in latitude by 50° in longitude. Lower-tropospheric westerly \mathbf{v}_h' peak near 850 hPa, with strong meridional convergence to the north and south at this level (Fig. 4.13a, day 0). At 200 hPa, the wind anomaly pattern displays moderate divergence, and a zone of negative OLR' stretches from (+10° lat, -15° lon) to (-5° lat, +30° lon). Both q_{600}' and ω_{600}' have a similar spatial structure and are close to their most positive and negative values, respectively. The upper-level flow field (Fig. 4.13b, day 0) resembles the expected tropical atmospheric response to localized heating (Gill, 1980), with a rapidly-propagating Kelvin response (easterly wind anomalies) to the east and a slow Rossby response (westerly wind anomalies) to the west of

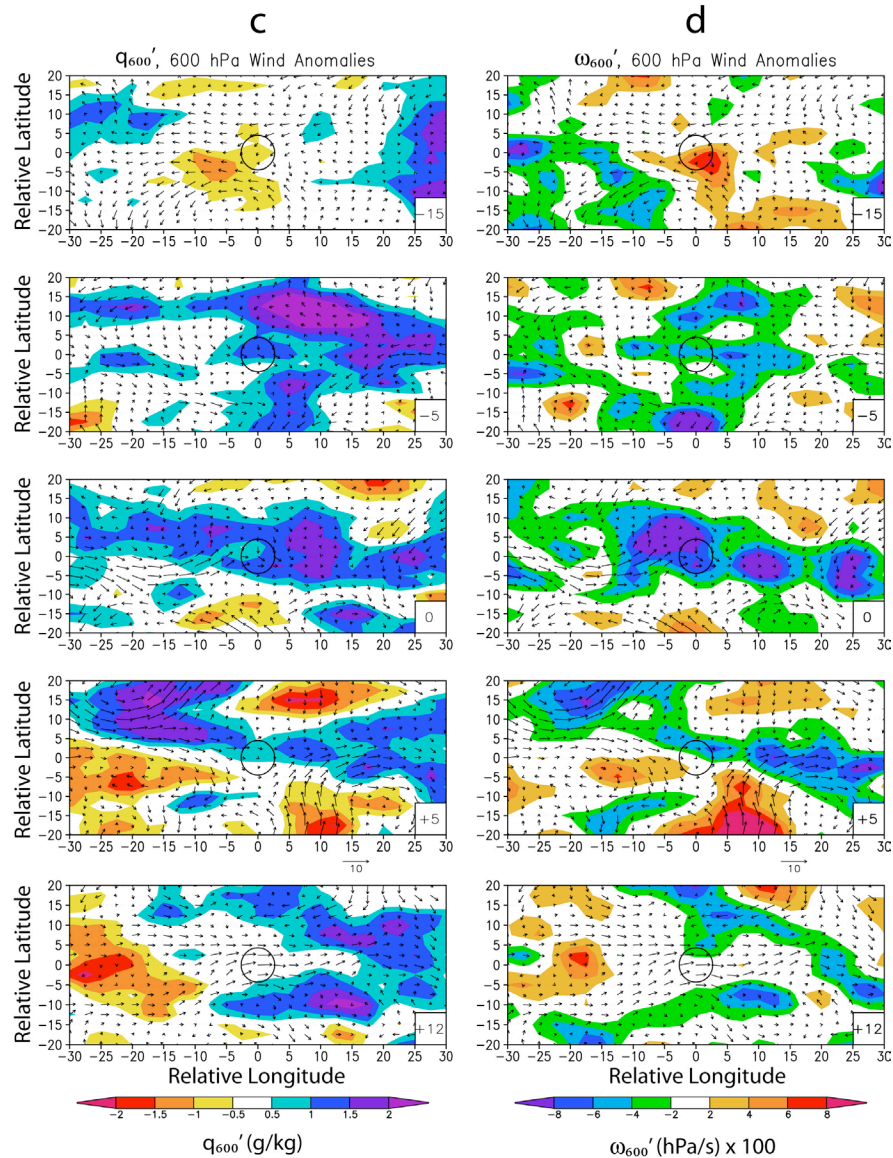


Figure 4.13 (continued): Composite map sequences of $q_{600 \text{ hPa}}'$ and $\mathbf{V}_{600 \text{ hPa}}'$ (column c), and $\omega_{600 \text{ hPa}}'$ and $\mathbf{V}_{600 \text{ hPa}}'$ (column d) for the individual gridpoint framework. The zero lag day corresponds to the day of maximum total rainfall at the 0 longitude/0 latitude point (the “origin point”, circled in each panel). It is important to note that the zero latitude line does *not* correspond to the Equator but rather is *relative* to each event in the composite.

the heat source. Additionally, dual anticyclonic gyres (“A” in Fig. 4.13b, day 0) have developed and flank the precipitation maximum to the west at $\pm 20^\circ$ latitude.

The intense precipitation and initial low-level westerly wind burst have shifted 10° - 30° east of the origin point by day +5 (Fig. 4.13a). In the upper troposphere, the anticyclonic

gyres noted on day 0 have also shifted slightly eastward and poleward but remain strong (“A” in Fig. 4.13b, day +5). This matches the results of HS94 (their Fig. 3). At this time, drier air from the west begins to infiltrate the zonal band near the origin point. This dry intrusion can be seen in the tongue of below-normal q_{600}' extending eastward to (-5° lat, -5° lon), as well as the area of subsidence at 600 hPa just southwest of the origin point. Beginning on day +5, the patterns of rainfall, OLR' , q_{600}' , and ω_{600}' develop northern and southern branches near and to the west of the origin point, while patterns remain coherent and maximized along the zero latitude line to the east. This branching is noted in the dual rainfall maxima at (-7.5° lat, $\pm 7.5^\circ$ lon), and presumably represents a slow latitudinal migration of the MJO signal (see Fig. 2 of Madden and Julian, 1994). Maloney and Hartmann (1998), like HS94, note that strengthening west winds of the type seen in Fig. 4.13 are associated with a coupled Kelvin-Rossby circulation, with the main area of precipitation being separated into northern and southern lobes as the Rossby waves propagate poleward.

Leading up to day +12, the main area of precipitation continues to move well east of the origin point. The northern and southern branched structures, visible in all variables displayed, continue to migrate slowly poleward and dissipate. Day +12 was chosen to illustrate the lower-tropospheric wind patterns associated with the composite westerly wind burst (see Fig. 3.22). At and below 600 hPa, substantial westerly wind anomalies are observed near the origin point. Dual low-level cyclonic gyres (“C” in Fig. 4.13a, day +12; associated with the strong meridional convergence to the west) flank the origin point to the north and south at more than $\pm 20^\circ$ latitude. At 200 hPa, anticyclonic gyres (“A” in Fig. 4.13b, day +12) create an opposite flow pattern to that of the lower levels, as in HS94. In general, the tongues of $OLR' > 0$, $q_{600}' < 0$, and $\omega_{600}' > 0$ have extended farther east along the zero latitude line and signify the return to the dry phase of the MJO.

4.2.3 Single event (spatial), gridpoint-based (21 October 1998)

The map series displayed in Fig. 4.13 represent averages of dynamical, radiative, and hydrologic fields over nine individual events. These particular MJO events are located at different geographic points and various times throughout the boreal winter. How do the atmospheric fields behave on the basis of a single event? Are the physical features noted in the composite of Fig. 4.13 also seen in the single-event map sequence? In response to these questions, we present map sequences (Figure 4.14) for a single MJO event centered at (2.5°S, 67.5°E) (the “origin point”; circled in each frame of Fig. 4.14) with corresponding total rainfall maximum of 80.1 mm on 21 October 1998 (“day 0”). This event shares many of the characteristics described in the composite map sequence (Fig. 4.13), but is unique in that it appears to capture the initiation of an MJO wave in the equatorial west-central Indian Ocean. As in Fig. 4.13, map sequences of total rainfall, v_h' at 850 hPa and 200 hPa, and OLR' will be displayed. We also show v_h' at 1000 hPa and 775 hPa, q_{775}' , ω_{775}' , SLHF', and PW' for purposes of discussion. The 775 hPa pressure level is chosen to illustrate rapid low-level drying following the main convection. At 600 hPa, lingering moisture—possibly from anvil detrainment or evaporation associated with stratiform precipitation—is observed through day +10.

Fifteen days prior to the most intense total precipitation rates, 850 hPa v_h' are light and from the east-southeast. No precipitation is falling at this time. OLR' and q_{775}' are above background levels and ω_{775}' is weakly positive, indicating an environment unfavorable for deep convection. Upper-tropospheric wind anomalies near the origin point are light and, as in the composite (Fig. 4.13), a strong cyclonic gyre is positioned to the southeast with a weaker cyclonic system to the northeast (marked “C” in Fig. 4.14b, day -15). Surface flux perturbations on day -15 and all other lag days examined are above 18-year climatological values, suggesting that the lower troposphere is abnormally turbulent during periods of

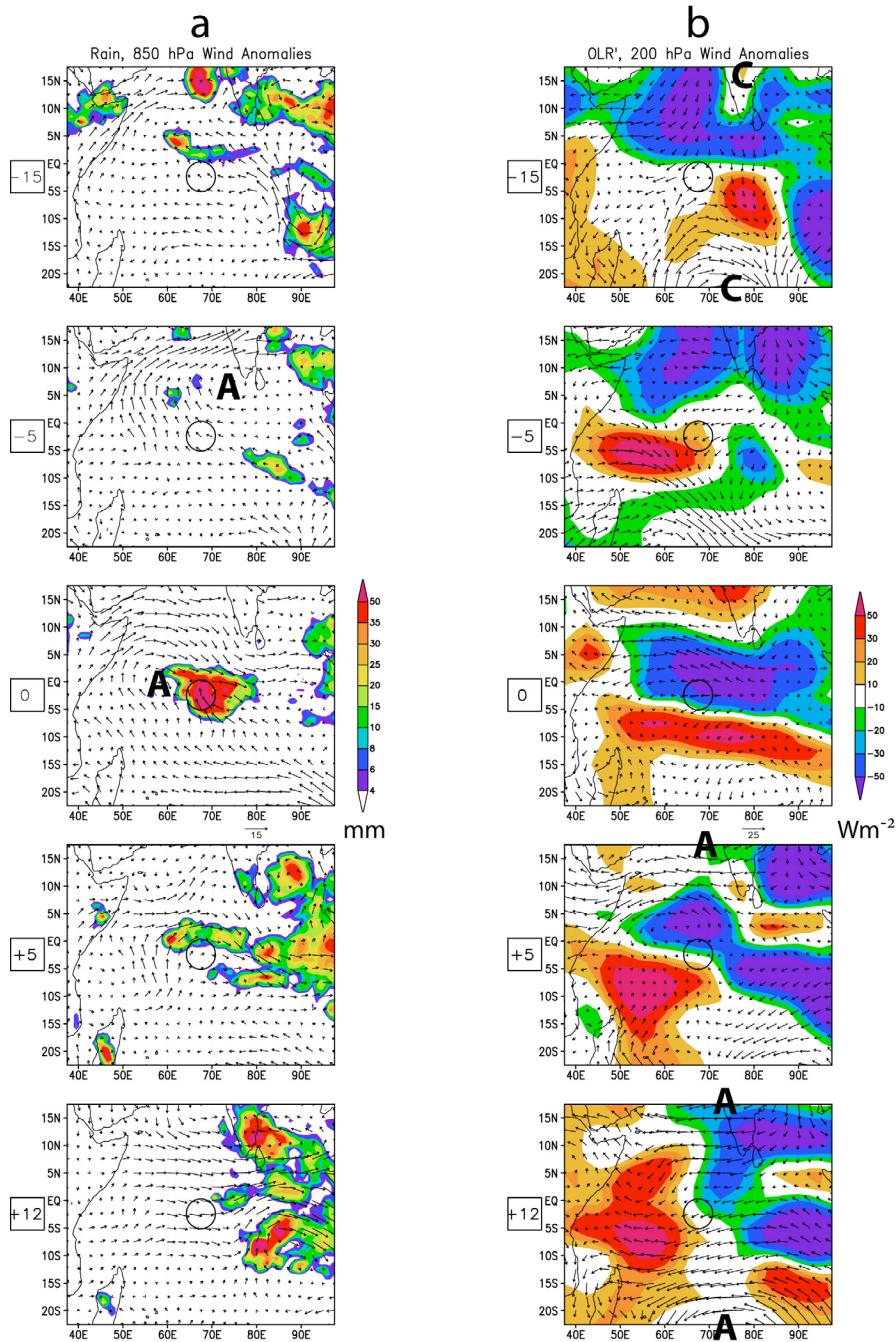


Figure 4.14: Map sequences of TRMM total rainfall and $\mathbf{V}_{850 \text{ hPa}}'$ (column a), and OLR' and $\mathbf{V}_{200 \text{ hPa}}'$ (column b) for the single event of 21 October 1998 based on the individual gridpoint framework. Anomaly values represent departures from the climatological mean (1984-2001) and not the MJO background state. Lag days are located to the left of each panel and correspond to the same lag days as seen in the composite map sequences of Figure 4.13. Maximum wind vector magnitudes (m/s) appear just below the x-axis of the day-0 panel. The zero lag day corresponds to the day of maximum total rainfall at the geographical base point (2.5°S , 67.5°E , circled in each panel). Letters “A” and “C” represent anticyclonic and cyclonic gyres as discussed in the text.

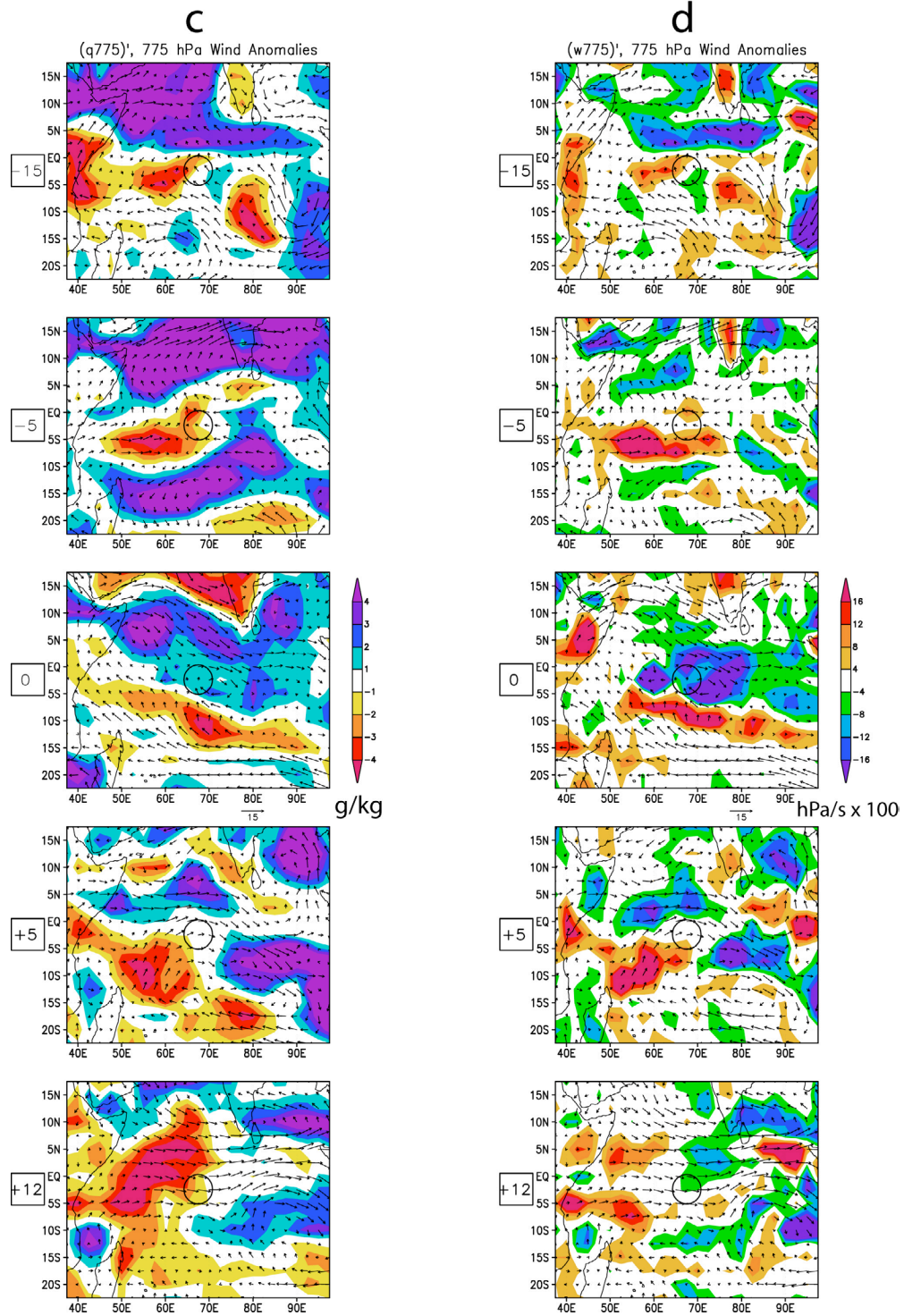


Figure 4.14 (continued): Map sequences of $q_{775 \text{ hPa}}'$ and $\mathbf{V}_{775 \text{ hPa}}'$ (column c), and $w_{775 \text{ hPa}}'$ and $\mathbf{V}_{775 \text{ hPa}}'$ (column d) for the single event of 21 October 1998 based on the individual gridpoint framework.

increased MJO wave activity and thus supporting the use of the “MJO background state” concept (see Appendix A).

Around day -10 (not shown), a potent low-level cyclonic gyre develops just west of Indian and is complemented by an anticyclonic system positioned over Sri Lanka, creating a strong, onshore, westerly flow and heavy rainfall over India. Over the next few days, the cyclone drifts northward and the anticyclone migrates slowly southwestward to its position on day -5 (“A” in Fig. 4.14a, day -5). This set-up appears to favor a strengthening of the Somali Jet and its associated cross-equatorial flow, abundant moisture transport across the Arabian Sea, and intense rainfall over India. Throughout the troposphere above the origin point, \mathbf{v}_h' is easterly, and almost no rain has accumulated since day -15. Highly-moistened areas coupled with rising motion are noted to the north and south of the origin point (especially across the Arabian Sea), but OLR' and ω_{775}' remain slightly above average at the origin point on day -5. Ocean-atmosphere flux anomalies are quite strong on day -5 but weaken considerably between days -5 and -2.

Between days -5 and 0, the low-level anticyclonic gyre (“A” in Fig. 4.14a, day 0) continues to drift southwestward to a position west of the origin point by day 0. During its migration, the northerly flow on the east side of the anticyclonic gyre encounters an increasingly-stronger southeasterly flow near the origin point, greatly enhancing low-level convergence and possibly lending support to a CISK-like mechanism. An area of precipitation rapidly blossoms directly over the origin point on day -3 (not shown) and strengthens to its maximum intensity on day 0 (Fig. 4.14a, day 0). For this event, intense rainfall developed *in situ* and did not propagate toward the origin point from the west, making this something of a unique situation. On day 0, low- to mid-tropospheric \mathbf{v}_h' rapidly shift from easterly to westerly, while at 200 hPa \mathbf{v}_h' remains easterly and meridionally divergent. At this time, a dry air mass is seen over southern India and the Arabian Sea. Despite maxima in amplitude

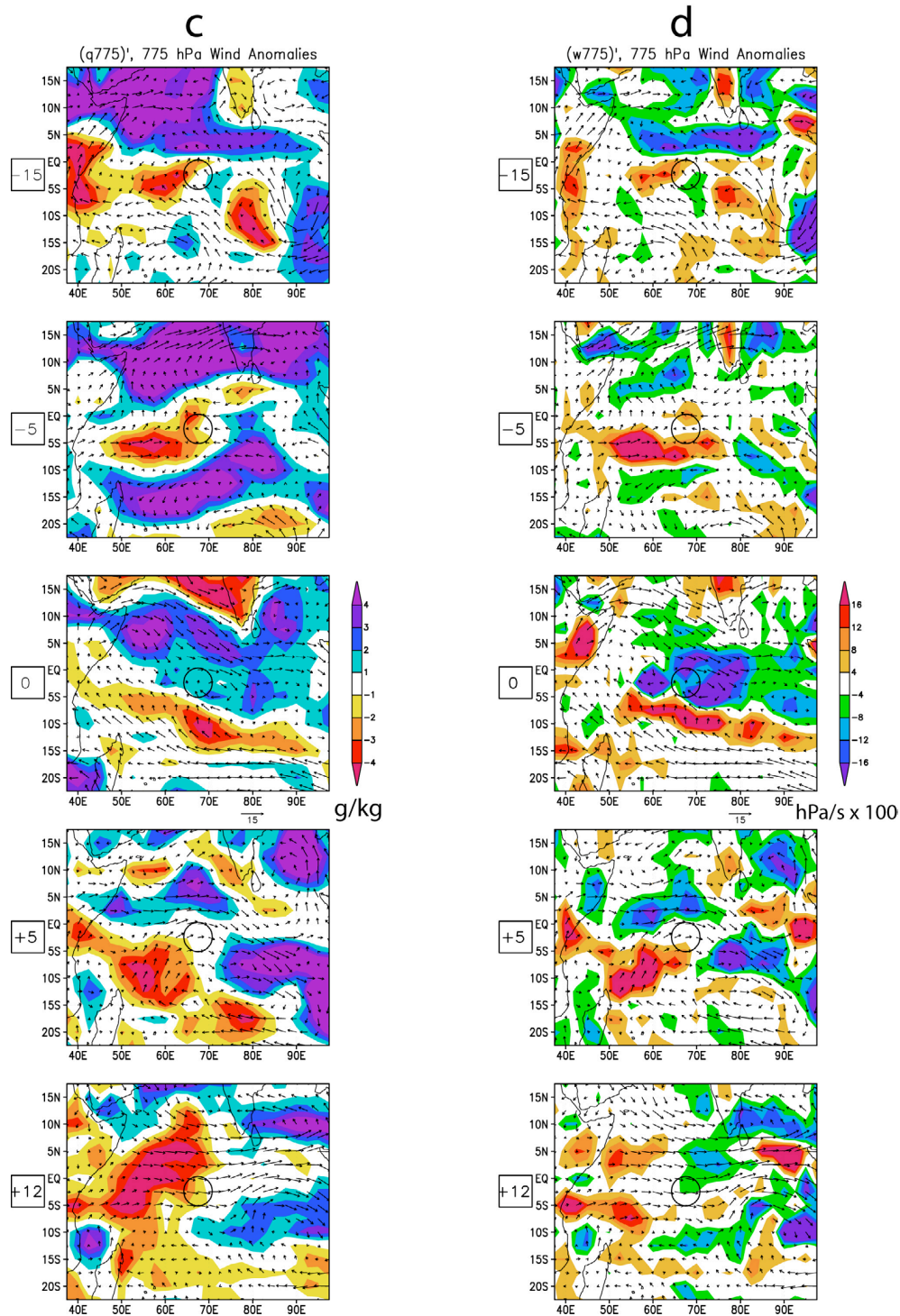


Figure 4.14 (continued): Map sequences of $q_{775 \text{ hPa}}'$ and $\mathbf{V}_{775 \text{ hPa}}'$ (column c), and $w_{775 \text{ hPa}}'$ and $\mathbf{V}_{775 \text{ hPa}}'$ (column d) for the single event of 21 October 1998 based on the individual gridpoint framework.

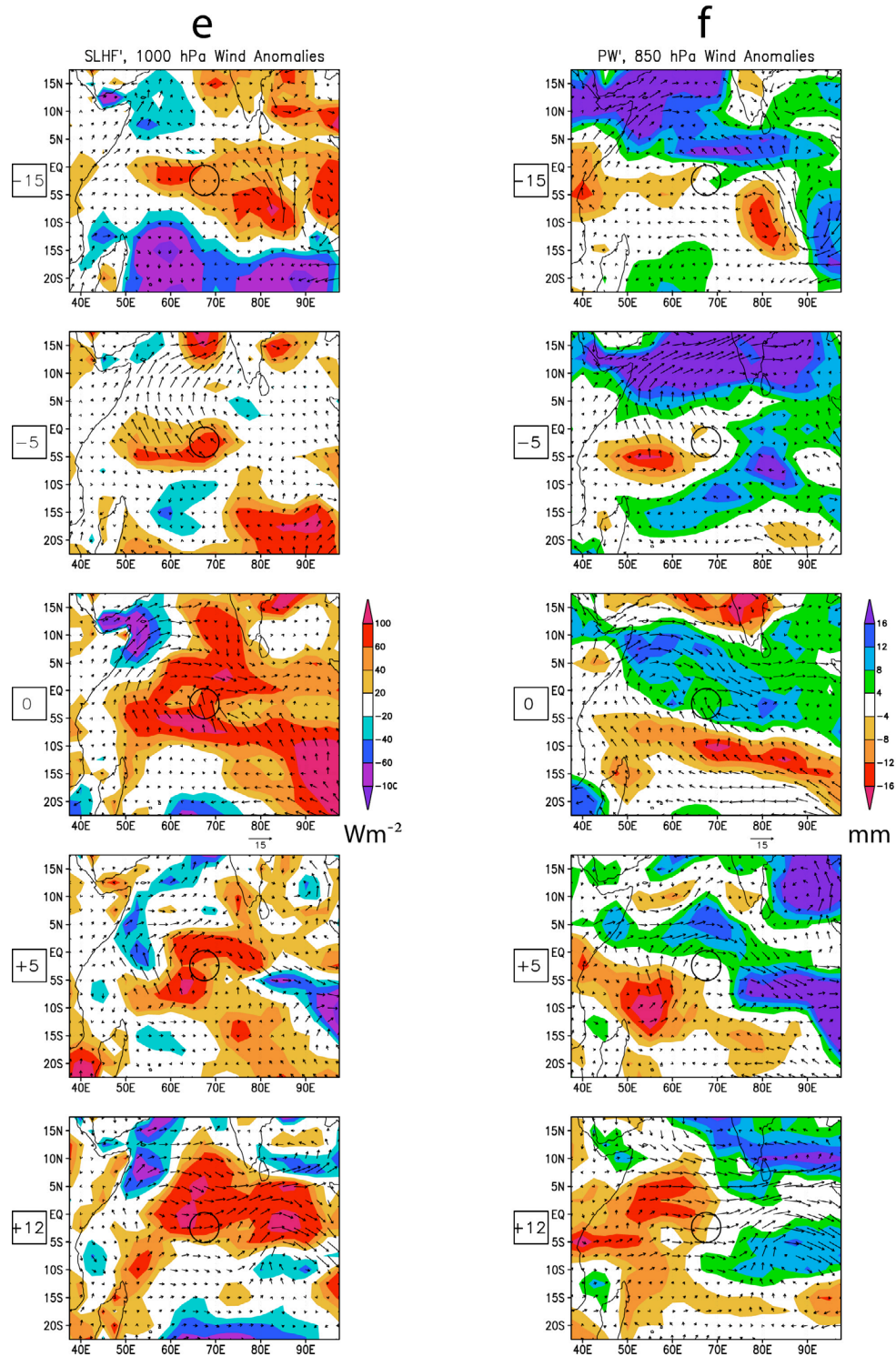


Figure 4.14 (continued): Map sequences of $SLHF'$ and $V_{1000 \text{ hPa}}'$ (column e), and PW' and $V_{850 \text{ hPa}}'$ (column f) for the single event of 21 October 1998 based on the individual gridpoint framework.

for q_{775}' and PW' (positive peaks) and ω_{775}' (negative peak) on day -1, the magnitudes of these perturbations remain large through day 0. OLR' is close to its minimum value, signifying the presence of deep convection. Additionally, negative OLR anomalies extending northwestward from the origin point (and the area of intense precipitation) could possibly signify the advection of upper-level moisture associated with anvil detrainment by strong easterly winds (see Fig. 4.14b, day 0). After a relative minimum on day -2, $SLHF'$ increases as surface winds become stronger on day 0. Interestingly, the zonal banded structure noted in the composite (e.g., Fig. 4.13b, day 0) is clearly seen in the single-event map series (e.g., Fig. 4.14b, day 0).

Following the episode of heavy precipitation on day 0, the area of intense rainfall shifts eastward to near $100^\circ E$ by day +5. Residual, lighter rain bands to the north and south of the origin point are observed and are not unlike the branched rain structures noted in the composite (Fig. 4.13a, day +5). The low-level anticyclonic gyre (“A” in Fig. 4.14a, day 0) has drifted southward across the Equator and weakened significantly by day +5. A northward drift and slight clockwise pivot of the zonal banded structure (e.g., Fig. 4.14b, day +5) are noted, where the axis dividing $OLR' > 0$ (south and west) from $OLR' < 0$ (north and east) is now oriented WNW-ESE and runs through the origin point. At the origin point, OLR' remains slightly below normal while ocean-atmosphere flux and PW anomalies continue to be above average. Low- and mid-tropospheric \mathbf{v}_h' are westerly while $\mathbf{v}_h' \approx 0$ in the upper troposphere. Despite the missing anticyclonic gyre to the southwest, some evidence of an upper-level anticyclonic gyre to the north of the origin point (“A” in Fig. 4.14b, day +5) is seen and matches this feature in the composite (Fig. 4.13b, day +5). Concerning moisture, inspection of the q_{775}' and ω_{775}' fields between days 0 and +5 (not shown) indicates that a rapid drying trend at 775 hPa is associated with westerly \mathbf{v}_h' but not sinking motion, further supporting the importance of the initial low-level advection of dry air by westerly wind anomalies as discussed in Section 4.1.1. Another important fea-

ture noted in the low-level moisture field is the southward progression (despite weakening) of dry q_{775}' seen over India on day 0. A pocket of dry air has shifted southward and is located at (10°N, 55°E) on day +5. Simultaneously, another dry air mass has developed near (10°S, 55°E).

Precipitation lingers to the east of the origin point as strong westerly wind anomalies develop on day +12. These lower-tropospheric (below 500 hPa) westerlies remain steady through day +20 (not shown). At upper levels, dual anticyclonic gyres (“A” in Fig. 4.14b, day +12) located 20-25° north and south of the origin point resemble a coupled Kelvin-Rossby response, closely match those features in the composite figure (“A” in Fig. 4.13b, day +12), and are associated with moderate easterly wind anomalies near and along the Equator. These upper-level easterly wind perturbations are likely advecting high-altitude moisture associated with anvil clouds generated from the deep convection well to the east, causing OLR' to remain negative despite $PW' < 0$, $q_{775}' < 0$, and $\omega_{775}' \approx 0$ at the origin point. This observation of lingering $OLR' < 0$ during a WWB was also noted during TOGA COARE (LJ96a). The previously zonally-banded structure (e.g., OLR' on day -5) has now become a longitudinally-banded (N-S) feature, with $OLR' < 0$ to the east and $OLR' > 0$ to the west of the origin point. This organization was partially achieved by a merging of dry air masses to the west of the origin point. The pocket of dry air at 775 hPa seen on day +5 (Fig. 4.14c, day +5) continued its southward drift (not shown), eventually merging with an expanding dry air mass centered near (7.5°S, 50°E). Following the air mass merger, this very dry air and attendant subsidence are advected toward the origin point on day +12. Daily maps of PW' (not shown) clearly display the merging of independent, dry air masses of subtropical origin at approximately 10° west of the origin point. Following the merging of the air masses, lower-tropospheric dry air is advected to the origin point 2-4 days later. The dry air mass is associated with large and positive OLR' , $PW' < 0$, negative q' at and below 600 hPa, and positive (sinking) ω' at and below 600

hPa. Finally, $SLHF'$ increases once again as strong surface winds related to the WWB migrate over the origin point.

4.2.4 Wave theories and the MJO: How does it work?

Over the past three decades, several theories have been proposed detailing the physical mechanisms that generate instability and wave amplification. Versions of these theories fall into four basic categories (as outlined in Chapter 1): wave-CISK, surface evaporation feedback (WISHE), stratiform instability, and discharge-recharge. In this section, we make use of the results of our analyses to determine the consistencies and differences between each proposed theory and the observations.

As discussed in Chapter 1, wave-CISK involves instability that occurs as a result of “cooperation” between localized convective heating and its environmental large-scale circulation [e.g., Hayashi (1970), Lindzen (1974)]. Possible evidence of wave-CISK-like processes is noted in the observation that initial robust convection [Fig. 4.12q, day -4; this convection is associated with a positive correlation between latent heating (Q_2' ; Fig. 4.12q) and warm anomalies (T' ; Fig. 4.12r)] appears to occur at and just prior to maximum low-level convergence as assessed by the temporal gradient of u' (Fig. 4.12a, days -4 to +1). Whether this convergence is a direct result of convective heating is unclear. Data of higher spatial resolution would be needed to confirm the precise relationships between convection and larger-scale low-level convergence. Below 500 hPa near day 0, a second-mode baroclinic structure (warm-over-cold) is associated with convective heating of anomalously-cool air (Figs. 4.12p and 4.12r, respectively). This is inconsistent with wave-CISK-like theories which require a positive correlation between deep-layer warm anomalies and convective heating. From Figs. 4.12p and 4.12r and Figs. 4.9a and 4.9b, deep convective heating lags low-level T' maxima by about 1-2 weeks (out of phase by more than 0.25 cycles as in SK03). It is possible that the inferred shallow cumuli partake in a CISK-like

process in which shallow heating generates weak low-level moisture convergence, but this is beyond any application of the reanalysis data ($2.5^\circ \times 2.5^\circ$) being used in this study. Many inconsistencies between wave-CISK theory and observations are apparent: the predicted phase speeds of a pure wave-CISK disturbance (15-30 m/s) are far more rapid than the observed MJO (~ 5 -10 m/s), the vertical structures of the predicted wave are much shallower than observations, and no global circumnavigation of the wave is observed as required by pure wave-CISK theory. Overall, certain elements may be important in the evolution of the MJO, but a direct application of the pure wave-CISK theory does not fully explain the observed oscillation.

WISHE theory was designed as a means of explaining wave growth in a quasi-equilibrium (QE) system (Arakawa and Schubert, 1974). Briefly, QE theory states that CAPE is rapidly consumed by convection and that adiabatic cooling nearly offsets latent heating (Emanuel et al., 1994). This balance is nearly achieved, as seen in the composite plots of adiabatic cooling and Q_1' (Figs. 4.12o and 4.12p, respectively). In a strict QE system, warm tropospheric anomalies lead heating by 0.25 cycles such that wave growth via the manufacturing of EAPE is impossible. In WISHE theory as applied to the QE system, wave growth is possible in the presence of basic state easterlies which promote ocean-atmosphere fluxes ahead of the wave. Any convective activity redistributes low-level moist entropy causing column heating to be shifted toward tropospheric warm anomalies and thus a generation of EAPE (Emanuel et al., 1994) is possible. The results of this study—including the time-height composite cross-sections (Chapter 3, Section 4.2.1), spatial composites (Section 4.2.2), and single spatial event (Section 4.2.3)—suggest that the WISHE mechanism is not operating in the events examined. In general, surface fluxes and horizontal wind anomalies are stronger to the west of the disturbance. Even in the single spatial event of Section 4.2.3, which occurred in the western Indian Ocean, surface fluxes were very weak just prior to intense convection. Additionally, many events occurred in a

region of climatological westerlies. Nonetheless, the contribution of ocean-atmosphere surface fluxes in the context of the MJO is not negligible.

Stratiform precipitation is common in the tropical convective regions and likely plays an important role in tropospheric heating and radiative processes (Houze, 1982). Thus, it is reasonable to hypothesize that stratiform processes may serve as a critical component in the interaction between convection and wave growth. The theory of stratiform instability involves the interplay of convective and stratiform heating modes, such that reductions in convective inhibition (CIN) outweigh fluctuations in CAPE in the presence of a warm-over-cold temperature structure (Mapes, 2000). The resulting deep convection and attendant convective heating profile evolve into warm-over-cold stratiform heating, in positive correlation with the original T' structure (thus generating EAPE). Our results do not directly support pure stratiform instability theory for a few reasons. Instead of warm-over-cold anomalies leading intense convection, the MJO wave involves low-level warming and moistening underlying cool, dry anomalies, suggestive of an increase in CAPE rather than a decrease in CIN. Additionally, Mapes (2000) found that pure stratiform instability disturbances are associated with upper-tropospheric warm anomalies positioned about 30° east of maximum convection. Our observations indicate that upper-tropospheric warm anomalies are collocated with convective heating (Q_1' ; Figs. 4.12p and 4.12r). It is possible that the stratiform instability mechanism may be important between days 0 and +5 when stratiform processes appear to be most active (see Fig. 4.12r). Perhaps this mechanism *prolongs* convection and possibly the MJO wet phase itself by reducing CIN and regenerating or maintaining residual convection (e.g., see deep-layer $Q_1' > 0$ for days 0 to +5 in Fig. 4.12p).

The essence of discharge-recharge theory is that a local, gradual build-up of instability through low-level warming and moistening preconditions the atmosphere for episodes of deep convection associated with MJO-like waves. Several aspects of this gradual enhance-

ment of instability and cumulus growth—as outlined in such papers as Bladé and Hartmann (1993), Hu and Randall (1994), and K-CW01—are noted in the results of this study. For example, time-height cross-sections of ω' , T' , q' , and RH' , as well as profiles of PW' , CTP , SSA' , and OLR' clearly suggest a slow build-up of low-level warming, moistening, and cumulus growth (e.g., Figs. 3.16, 3.32, and 4.12e).

Relative to the maximum total rainfall, our results indicate an asymmetry in timescales of the recharge and discharge phases such that convective dissipation and tropospheric drying occur more rapidly than cumulus growth and tropospheric moistening. In Figure 4.15, we present a schematic diagram of the discharge-recharge mechanism as seen in the reanalysis data. In terms of T' and q' (e.g., Figs. 4.12d, 4.12e, and Fig. 4.15), for instance, low-level warming and moistening are maximized for ~10-15 days, deep convection and precipitation processes ultimately serving to stabilize the troposphere are active for ~10 days, and suppressed convection with associated tropospheric drying are observed for ~15 days, thus yielding a 35-40-day oscillation. The timescale of these MJO stages might involve linkages between the hydrologic cycle and the ocean (Stephens et al., 2004) in addition to the atmospheric component as in Bladé and Hartmann (1993). Stephens et al. (2004) propose a humidistat theory in which the hydrologic cycle and SSTs mutually regulate one another. Our results are wholly consistent with those of Stephens et al. (2004), who find that maxima in SST lead maxima in PW and rainfall by about 10 days, and minima in OLR also by 10 days, as has been reported in the present study. The coupling between atmosphere and ocean in the context of the MJO is undoubtedly an important mechanism. Additionally, Stephens et al. (2004) indicate the importance of persistent high cloud coverage during the time of the WWB in stabilizing the atmosphere, which is in agreement with the low OLR values seen in Fig. 4.14b of this study. The concept of distinct MJO phases has also been investigated based on trimodal cloud characteristics (for review, see Johnson et al., 1999). Kikuchi and Takayabu (2004) used TOGA COARE

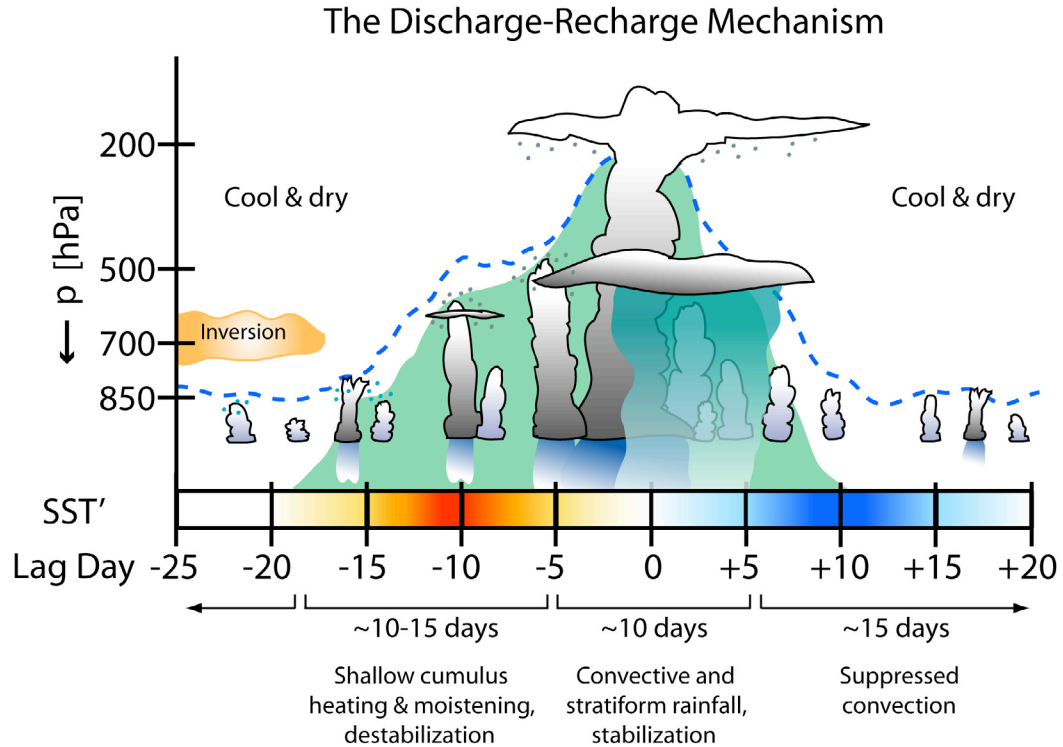


Figure 4.15: Time-height schematic diagram of the discharge-recharge mechanism. Along the horizontal axis appears the sea-surface temperature anomaly [SST' ; red (blue) indicates warm (cold) anomalies] and the lag day relative to time of maximum total rainfall (day 0). Stages of the discharge-recharge process, as seen in the ERA40 data, appear below the lag days. The approximate top level of convective cloud processes is indicated by the dashed blue line, while the green shading represents the approximate area of $q' > 0$. Light blue dots above shallower convective clouds represent moistening via detrainment, while gray dots below stratiform cloud types represent ice crystal fall-out and moistening. Convective precipitation is indicated by darker-blue rain shafts, and stratiform precipitation areas are light-blue and slightly transparent.

results to show that cloud growth occurs in stages associated with stable layers near (1) the trade wind inversion, (2) the freezing level (~ 550 hPa), and (3) the tropopause. While we see some hesitation in the vertical growth of moisture near the freezing level (e.g., Figs. 3.27 and 4.12s), the spatial resolution of the datasets used in the present study and differing results between compositing frameworks largely prohibit any decisive conclusions from being drawn in terms of trimodal cloud characteristics.

Evidence in support of the *localized* destabilization via low-level warming and moistening is noted in the fairly weak horizontal wind convergence (Fig. 3.22) and dominance of anomalous vertical moisture transport (Fig. 4.2) over horizontal moisture transport ~ 5 -15

days prior to maximum rainfall. Such observations suggest that, for most of the events in the composites presented, the build-up of low-level heat and moisture is accomplished by *local* mechanisms rather than by large-scale advective processes.

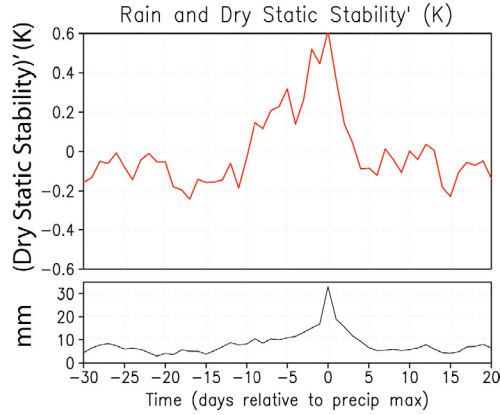


Figure 4.16: Composite timeseries of anomalous dry static stability ($\hat{\theta}' = \frac{\theta_{250}' - \theta_{775}'}{2}$) for the meridionally-averaged (10°S-5°N) framework. The events contained in this composite were selected with use of 20-100-day filtered TRMM rainfall (see text for explanation). The composite timeseries of total precipitation is also plotted. Anomaly values represent departures from the climatological mean (1984-2001) and not the MJO background state. Lag days are indicated below the rainfall timeseries, with day 0 corresponding to the day of maximum total rainfall. Negative lag days represent those days prior to intense rain.

A final aspect of discharge-recharge theory worthy of comment concerns the spatial characteristics of the MJO events analyzed and their related triggering mechanisms. In this study, most of the individual events are located in the eastern Indian and western Pacific Ocean areas (see Fig. 3.8 or 3.21). We chose these locations to correspond to maximum wet phase amplitude and not wave initiation, and so it is likely that the composite results largely reflect the evolution of a (nearly) fully-developed oscillation. Inspection of dry static stability ($\hat{\theta}' = \frac{\theta_{250}' - \theta_{775}'}{2}$; Figure. 4.16) supports this hypothesis, showing the shape of the $\hat{\theta}'$ profile to be quite similar to a model-generated stability composite of events 90° downstream of wave initiation [Fig. 11c in Bladé and Hartmann (1993); the rise in $\hat{\theta}'$ 10-15 days prior to maximum convective activity is attributed to advection of upper-level warm anomalies by the approaching disturbance]. Bladé and Hartmann focused mainly on instability build-up and subtropical triggering mechanisms for wave initiation in the western Indian Ocean. The individual event (21 October 1998) presented as spatial map sequences

in Fig. 4.14 is also located in the western Indian Ocean and provides some support for discharge-recharge theory as interpreted by Bladé and Hartmann (1993; see their Fig. 11a). Although the signal is noisy, the $\hat{\theta}$ profile (Figure 4.17) indicates a steady decline in stability beginning near lag day -14 to -10, a minimum in $\hat{\theta}'$ a few days prior to deep convection, and a rapid increase in $\hat{\theta}'$ during the deep convection. Note the distinct differences between Figs. 4.16 and 4.17. The destabilization near day -5 is likely due to a sharp increase in moist static energy at 1000 hPa (h_{1000}), while h_{400} remains quite low (not shown). Additionally, the 21 October 1998 event appears to have ties to a subtropical trigger, albeit in the form of low-level convergence near the edge of an anticyclone rather than an area of upper-level divergence impinging on the Tropics as in Bladé and Hartmann (1993).

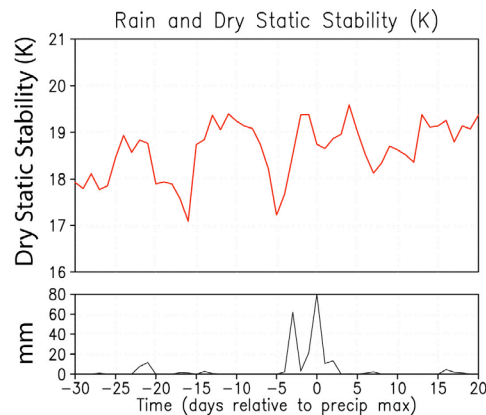


Figure 4.17: As in Figure 4.16 (except $\hat{\theta}$ instead of $\hat{\theta}'$), but for the single event of 21 October 1998 based on the individual gridpoint framework. The timeseries of total precipitation corresponding to this event is also plotted. Lag days are indicated below the rainfall timeseries, with day 0 corresponding to the day of maximum total rainfall. Negative lag days represent those days prior to intense rain.

For most of the events in the composite (located well east of wave initiation), convective triggering is likely accomplished by the propagating wave itself in conjunction with a preconditioned, destabilized environment. Hu and Randall's (1994) emphasis on local nonlinear feedbacks between radiation, convection, and surface fluxes and its governance over the MJO period may be operating in the events examined in this study. In their proposal, increasing low-level T' and q' underlie cool, dry anomalies aloft causing a reduction

in stability, thus leading to convective intensification. Radiative cooling aloft from convective cloud tops steepens the lapse rate and prolongs convection. Gusty surface winds generated by these clouds cause low-level turbulence and $SLHF' > 0$, providing a moisture source and once again prolonging convection. Once upper-level cloud warming overwhelms radiative cooling, and convective downdraft drying wins out over turbulent moistening, convection finally dissipates. As mentioned in recent paragraphs, the build-up of low-level heat and moisture is quite apparent. Unfortunately, we cannot readily assess the cloud-scale relationships between convective clouds and their associated radiative cooling. However, there is evidence in possible support of prolonged convective activity owing to the spike in $SLHF'$ (e.g., Fig. 4.12f) accompanying maximum rainfall. This flux of vapor into to lower levels could aid in prolonging convection as seen in the positive convective heating values extending 5 days after maximum rainfall (Fig. 4.12p). It is unclear, however, whether this prolonged convection may be attributed to stratiform instability processes, the factors associated with Hu and Randall's (1994) theory, or both. Overall, the theory of localized destabilization and discharge-recharge mechanisms is highly appropriate in explaining many of the observed features of MJO wave evolution.

4.2.5 Comments on statistical significance

To assess the quantitative robustness of the major features being presented in this report, we compute statistical significance values. Figure 4.18 (a-c) depicts t-statistic significance values at the 90% level for (a) Q_1' and (b) Q_2' for the individual gridpoint framework, as well as (c) the zonal advective component contributing toward $\frac{\partial q'}{\partial t}$ (as in Fig. 4.1a). Anomalies plotted here are departures from their 1997-2002 averages rather than departures as outlined in Appendix A. This method was implemented solely to test significance in a more straightforward manner rather than using the more complex method described in Appendix A. The 6.5-year span is short, but the composites based on this climatology are

similar to those as computed from the procedure in Appendix A. Additionally, composites based on an 18-year climatology show notable trends (see discussion in Appendix A).

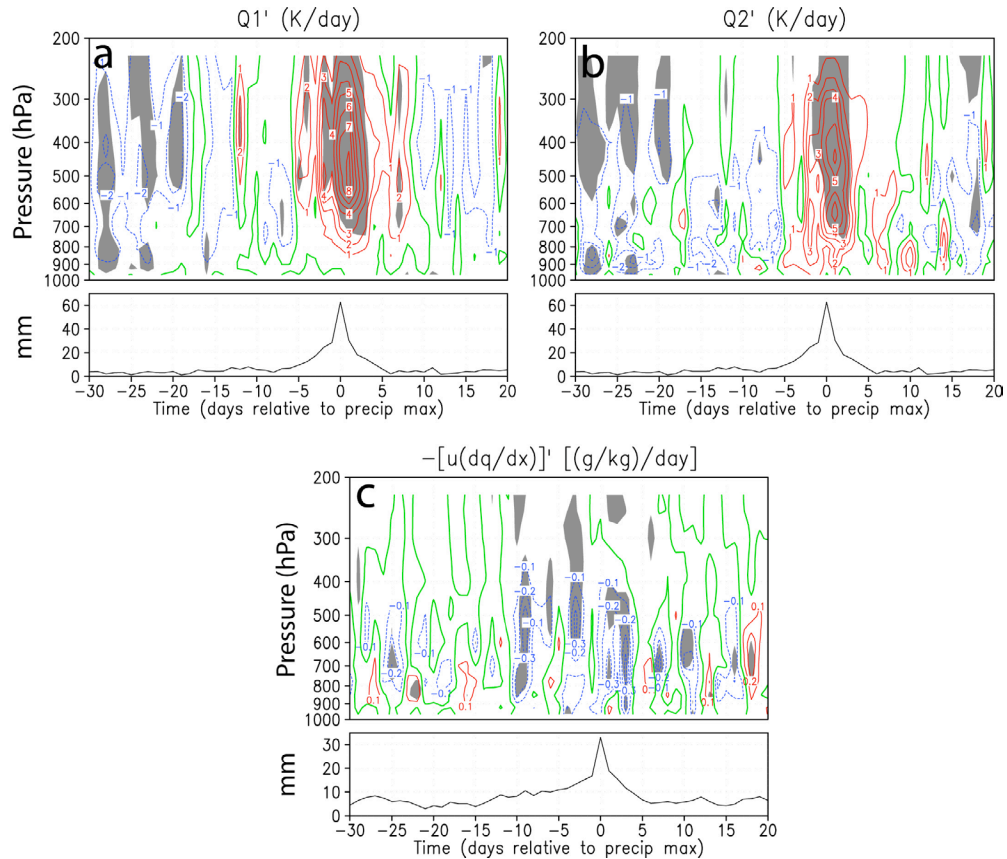


Figure 4.18: Statistical significance shading of the time-height cross-sections of (a) Q_1' and (b) Q_2' for the individual gridpoint framework (as in Fig. 4.12p and 4.12q, respectively), as well as the (c) the zonal component of anomalous time rate of change of specific humidity $[\frac{\partial q'}{\partial t}]'$ for the meridionally-averaged case (as in Fig. 4.1a). Gray shading represents values that exceed the 90% statistical significance level. Departures from the 6.5-year span 1997-2002 are plotted for ease of computing statistical significance. Anomaly features are quite similar to those observed when using the procedure in Appendix A to calculate anomalies (as in Figs. 4.1a, 4.12p, and 4.12q).

Figs. 4.18a and 4.18b indicate a very weak signal but of correct physical sign associated with general pre-convective heating and moistening of the lower levels. Areas of statistical significance, however, are not present where shallow cumulus activity is anticipated. In the first five days following intense rainfall, there is evidence of rapid drying associated with the increase in horizontal winds (Fig. 4.18c). Pockets of gray shading in this area (days 0 to +5, below 500 hPa) suggest that this drying may be statistically significant above the 90% level.

There are many difficulties in applying the concepts of statistical significance to the results in this paper. Due to the short data record of TRMM rainfall (1998-2002) and limited extension of our ERA40 dataset (1997-2002), small sample sizes of approximately 10 events are contained in each of the gridpoint and meridionally-averaged composites. This unavoidable problem sometimes lead to relatively large composite standard deviation values and small degrees of freedom. In addition, statistical theory suggests that 10% of the shading in Fig. 4.18 is random, given a significance threshold of 90%. Despite these statistical limitations, we should not completely discount the physical results. For example, although no significance shading is seen at low levels between days -10 and -5 in the Q_1' plot (Fig. 4.18a), active vertical moisture transport and warm, moist anomalies (see Fig. 4.12) suggest a physical link explained by shallow convective processes (shallow cumuli). Additionally, observational experiments such as TOGA COARE testify to the presence and importance of such shallow cloud activity. Concerning post-convective drying, strong, statistically significant westerly winds occur within five days after intense rainfall and occur simultaneously with a sharp low-level decrease in q' . Although only weak statistical significance is noted in Fig. 4.18c, the conclusion of rapid drying associated with increased zonal winds is not physically unreasonable and has been largely overlooked in previous research studies. We intend to further investigate these mechanisms in the future.

4.3 Exploratory Analyses

In the discussion that follows, we examine the consistency between certain physical parameters, and how well specific variables relate to one another. The primary purpose of this examination is to check the accuracy and physical relationship of moisture (Q_2) and cloud (CTP) variables. In Section 4.3.1, vertically-integrated Q_2 is compared to surface evaporation (E_o) and precipitation (P_o) using several basic assumptions. MODIS-derived

CTP fields are compared and contrasted to high-resolution GLAS cloud data in Section 4.3.2.

4.3.1 Comments on the precipitation budget

Although the apparent moisture sink Q_2 is mainly used to diagnose convective moistening and drying, its vertical integral can also provide an estimate of precipitation P_o (Yanai et al., 1973). Integrating Q_2 from the surface (pressure p_o) to the cloud-top level (pressure p_T) allows a check of consistency between Q_2 and total P_o . One could also use this method to deduce P_o (as in LJ96b) if \mathbf{v} (three-dimensional) and q are known at each pressure level over some area of $O(100 \text{ km})$.

From Yanai et al. (1973),

$$Q_2 \cong L(c - e) + L \frac{\partial}{\partial p} \overline{q' \omega'} \quad (4.7)$$

where the horizontal eddy transports of water vapor have been neglected, and L is the latent heat of vaporization at 0°C , $c \equiv c(x, y, p, t)$ the rate of condensation per unit mass of air, $e \equiv e(x, y, p, t)$ the evaporation of liquid, and $q' \equiv q'(x, y, p, t)$ and $\omega' \equiv \omega'(x, y, p, t)$ the departures of water vapor mixing ratio and pressure velocity from their area means, respectively. As mentioned in Section 4.1.2, we have substituted specific humidity q for water vapor mixing ratio (also q in 4.7). Integrating (4.7) from the cloud-top to the surface,

$$\frac{1}{g} \int_{p_T}^{p_o} Q_2 dp \cong \frac{L}{g} \int_{p_T}^{p_o} (c - e) dp + \frac{L}{g} \left(\overline{q' \omega'} \right)_{p=p_o} \quad (4.8)$$

$$\frac{1}{g} \int_{p_T}^{p_o} Q_2 dp \cong LP_o - \rho_o L \left(\overline{q' \omega'} \right)_{p=p_o} \quad (4.9)$$

$$\frac{1}{g} \int_{p_T}^{p_o} Q_2 dp \cong L(P_o - E_o) \quad (4.10)$$

where P_o and E_o are the surface precipitation and evaporation rates, ρ_o the density of water, p_o the surface pressure, and w' the departure of the vertical velocity (height coordinates) from its area mean. In going from (4.7) to (4.8), we have assumed that the vertical flux of vapor out of the cloud top is insignificant ($-\frac{L}{g} (\overline{q' \omega'})_{p=p_r} \approx 0$). By arriving at (4.9) from (4.8), we have assumed that any and all net liquid condensate within the column falls and reaches the surface as precipitation (i.e., there is no storage of water within the column and no transport of water to neighboring columns). Additionally, the vertical velocity is converted from pressure to height coordinates. To obtain (4.10) from (4.9), we note that the evaporation rate from the ocean or land surface is simply the vertical flux of vapor across the $p = p_o$ surface. The only sources of vapor within the column are the horizontal advection terms associated with Q_2 and the surface evaporation.

A comparison of the LHS and RHS of (4.10) was conducted for several geographic areas in the Indian and Pacific Oceans (see Table 4.1). The first calculation involves a region spanning much of the West Pacific warm pool, including the land masses of eastern Indonesia and Papua New Guinea. Boreal-winter (NDJF) averages of each variable over the range 1997-2002 were used. Averages for the same geographic region of MODIS-derived CTP were employed to assess the level of cloud top for use in the vertical integration of Q_2 . From Table 4.1, it is apparent that the value of the Q_2 vertical integral [LHS of (4.10)] is less than that of the net precipitation [RHS of (4.10)] for the “Warm Pool” case. The mean daily precipitation, as calculated using the Q_2 budget (4.10), is approximately 3 mm/day lower than the direct precipitation output from ERA40. Within the northern branch of the ITCZ (“nITCZ” in Table 4.1), the LHS and RHS of (4.10) differ by $\sim 14 \text{ Wm}^{-2}$, and the ERA40 direct precipitation estimate is about 5 mm/day more than the value calculated from P_o in (4.10). A much closer match in net precipitation is noted for the Eastern Indian Ocean region (“EIND” in Table 4.1), where the LHS is $\sim 9 \text{ Wm}^{-2}$ less than the RHS of (4.10) and calculated P_o is only 0.3 mm/day less than the direct ERA40 model output.

Table 4.1. *Boreal winter-mean* (NDJF) hydrologic variables associated with Equation 4.10. In terms of the geographic regions analyzed, “Warm Pool” is designated as (7.5°S-7.5°N, 120°E-160°E); “nITCZ” corresponds to the northern branch of the ITCZ and spans (2.5°N-7.5°N, 150°E-160°E); and “EIND” corresponds to the equatorial Eastern Indian Ocean and spans (10°S-0°S, 60°E-90°E). $P_{o,a}$ is the mean precipitation rate as calculated from Equation 4.10 using ERA40 non-precipitation variables (essentially, v , q , and E_o). $P_{o,b}$ and E_o are the mean precipitation and evaporation rates (respectively) directly output from the ERA40 model, and CTP is cloud-top pressure.

<i>Parameter</i>	<i>Units</i>	<i>Warm Pool</i>	<i>nITCZ</i>	<i>EIND</i>
Integrated Q_2 (LHS 4.10)	Wm^{-2}	293.9	168.1	197.8
Net precipitation (RHS 4.10)	Wm^{-2}	260.4	182.2	206.9
LHS - RHS (4.10)	Wm^{-2}	+33.5	-14.1	-9.1
$P_{o,a}$ (calculated from 4.10)	mm	10.2	5.8	11.0
$P_{o,b}$ (ERA40 output)	mm	13.1	11.4	11.3
$P_{o,a} - P_{o,b}$	mm	-2.9	-5.6	-0.3
E_o	mm	4.1	5.1	4.2
CTP (MODIS)	hPa	403	427	485
<i>Parameter</i>	<i>Units</i>	<i>Warm Pool</i>	<i>nITCZ</i>	<i>EIND</i>

The precipitation values ($P_{o,b}$) presented in Table 4.1 are based on output from ERA40 only. We also conducted similar experiments by substituting TRMM rainfall for ERA40 rainfall and found differences of similar magnitude (but of opposite sign) between the precipitation estimates of $P_{o,a}$ (as calculated from 4.10) and the directly-measured $P_{o,b}$ (from TRMM). For these calculations, ERA40 evaporation was used. These differences are not unexpected given the discrepancies between TRMM and ERA40 precipitation estimates (e.g., Fig. 3.1).

There are several reasons that might explain why differences exist between the calculated and direct P_o . First, while the assumptions made in deriving (4.10) simplify the problem, they may also may not be entirely appropriate. Water storage within the column and horizontal liquid transports to neighboring columns are distinct possibilities in nature. Additionally, horizontal fluxes of q by eddies and vertical fluxes of q above the cloud top might not be completely negligible in all cases. Another source of error is the estimate of

CTP, which is used as a limit of integration for the LHS of (4.10). Small changes in CTP, combined with the relatively coarse vertical resolution (~ 50 hPa) of the ERA40 model (including the necessary interpolation) and the rapidly-changing Q_2 integral sum with height (not shown), can affect the value of the LHS of (4.10). Physically, it is possible that land mass areas or regions of very intense rainfall might introduce errors into the ERA40 direct precipitation estimates, producing too much rainfall and thus providing a better match with the calculated P_o should corrections be implemented. Given this enormous number of uncertainties and sources of error, we feel that the calculated and “directly-measured” ERA40 P_o are reasonably close.

4.3.2 Cloud-top characteristics: GLAS and MODIS

One challenge facing atmospheric scientists today is achieving an accurate representation of cloud characteristics in the Tropics. In particular, cloud overlap and the determination of multiple cloud layers pose a formidable problem in the context of remotely sensing the data-sparse Equatorial region. Deep convective clouds act as portals through which lower-level water in all phases travels. For deep convective clouds, this moisture is ultimately ejected into the upper troposphere and spreads horizontally, generating high-altitude cirrus clouds which are common in the warm-ocean tropical areas (Jin et al., 1996; Dessler and Yang, 2003). Figure 4.19 displays a latitude-height cross-section of GLAS-derived cloud-top heights totaled from 16 October-19 November, 2003, for the longitude range 80°E - 90°E . Only multi-layer cloud scenes are plotted. Blue, green, and red dots represent the highest, second-highest, and third-highest cloud top heights, respectively. The plot shows that most of the blue dots are found above 12 km (~ 200 hPa), suggesting that high-altitude cloudiness is common in the Tropics. The blue dots are most common where intense convection occurs (see Fig. 3.1), indicating the presence of anvil clouds in the vicinity of towering cumulonimbi. Even on the edges of deep convection near 10°S - 20°S , high-level cloudiness

is still quite common and clearly overlaps the cluster of lower-tropospheric clouds below 3 km (~ 690 hPa). Although these anvil clouds may be very thin (even translucent) their radiative properties can presumably “mask” cloud layers beneath them by partially or completely attenuating the signal of active or passive satellite sensors. How well do the cloud properties in the MODIS $1^\circ \times 1^\circ$, daily gridded dataset capture the true state of the atmosphere? What effects do high cloud layers have on the quantitative, grid-average cloud-top characteristics? We now present a brief investigation to address such issues using MODIS-derived CTP and high-resolution GLAS cloud-height and thickness data.

A single track segment of GLAS cloud data for 20 October 2003 is displayed in Figure 4.20. Between approximately 1248-1312 UTC, ICESat (housing the GLAS instrument) traveled northward along a line from (40°S , 105.7°E) to (40°N , 93.6°E). In Fig. 4.20, detectable cloud location and thickness are represented by vertical blue lines while red dots correspond to the GLAS-derived boundary layer top. When thick cloud layers exist and the signal becomes saturated, no boundary layer information is able to be retrieved. We will focus on the area between the Equator and 20°S . Between 0°S - 7°S , deep, thick clouds with tops near or above 15 km (~ 140 hPa) are detected. Because no boundary layer information exists, it is inferred that the top-down signal has become saturated and that deep convective

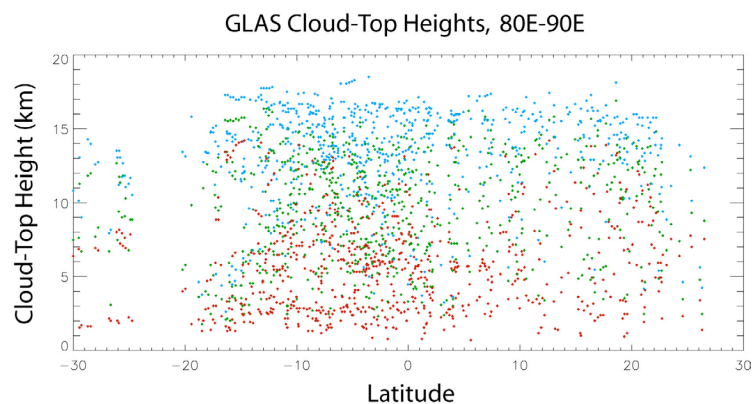


Figure 4.19: Latitude-height cross-section of GLAS-derived cloud-top heights totaled between 16 October-19 November, 2003, for the longitude range 80°E - 90°E . Only multi-layer cloud scenes are plotted. Blue, green, and red dots represent the highest, second-highest, and third-highest cloud top heights, respectively. *GLAS analysis plot courtesy of Maïke Ahlgrimm.*

clouds are likely. From 7°S-15°S, multiple cloud layers appear, with the upper-layer cloud tops ranging from 9-17 km (~310-100 hPa) and the lower layer from 2-4 km (at or below 600 hPa). The upper cloud layer in this area must not be as thick or deep as that closer to the Equator because the signal has not become saturated. As a comparison to the GLAS data, we present MODIS-derived CTP estimates (Figure 4.21). The CTP values represent a 24-hour average for 20 October 2003 binned into 1°x1° gridboxes, providing a reasonably similar match to the GLAS data specifications. Note that Fig. 4.21 captures only a section of the track in Fig. 4.20 (20°S-Equator). From the Equator to 5°S, the deep convection from the GLAS plot is reflected in the MODIS CTP, with most CTP values less than 250 hPa (> 11.5 km). Between 5°S and 11°S along the indicated satellite path, CTPs are less than 550 hPa [> 4.5 km; approaching 350 hPa (~8 km) in some cases]. This situation highlights one limitation of MODIS CTP, in that a single “optimized” cloud-top pressure value must be designated for each pixel, even if multiple cloud layers exist. In this particular example, mid- and high-level cloudiness potentially either masks completely the low-level cloud layer or causes an overestimation of its height due to signal attenuation. We hypothesize that the presence of shallow cumuli might not always be fully represented in the composite CTP plots (e.g., Fig. 3.34), especially in the immediate vicinity of deep convection. From 12°S-20°S, the high-level clouds in Fig. 4.20 are apparently sufficiently translucent for MODIS to detect and select the lower-tropospheric clouds as the optimized layer. At these latitudes, GLAS and MODIS are closely matched and indicate a cloud-top level of below 690 hPa (~3 km). Overall, the MODIS instrumentation provides extensive and accurate cloud information for areas of the globe largely void of surface-based atmospheric measurements. The purpose of this exercise was not to question the integrity of the CTP data, but rather to point out the unavoidable limitations of the CTP retrieval process.

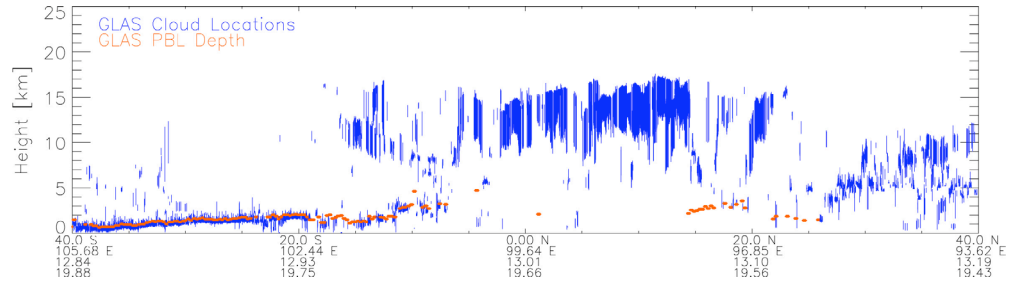


Figure 4.20: A single track segment of GLAS cloud data for 20 October 2003 as represented in a time-height cross-section. Along the x-axis, the numbers from top to bottom indicate latitude, longitude, UTC time, and local time. Between approximately 1248-1312 UTC, ICESat (housing the GLAS instrument) traveled northward along a line from (40°S, 105.7°E) to (40°N, 93.6°E). Detectable cloud locations and thicknesses are represented by vertical blue lines while red dots correspond to GLAS-derived boundary layer tops. When thick cloud layers exist and the signal becomes saturated, no boundary layer information is able to be retrieved (e.g., between 5°N-10°N). *GLAS analysis plot courtesy of Maïke Ahlgrimm.*

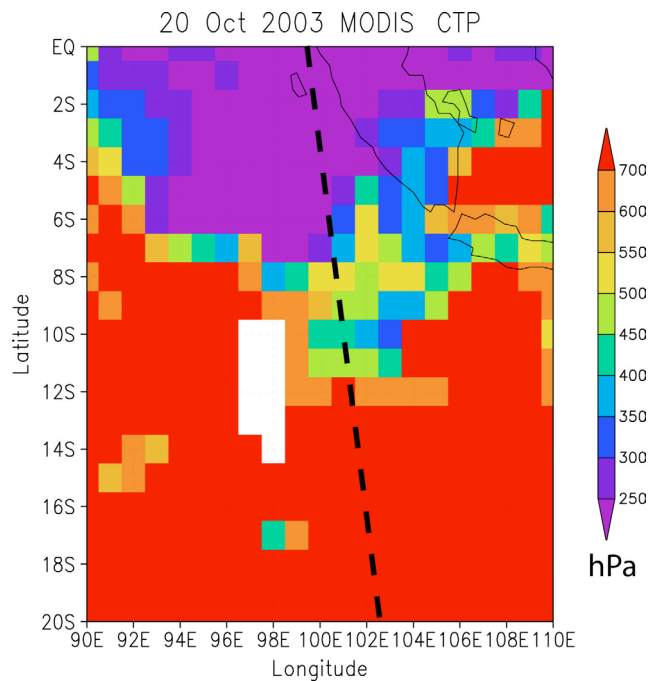


Figure 4.21: MODIS-derived daily-averaged 1°x1° cloud-top pressure (CTP) values corresponding to a time and space location similar to that of the GLAS cross-section in Figure 4.20. Black dashed line represents the approximate ICESat satellite track (housing GLAS instrument). White shading indicates missing data. Purple shading corresponds to lower CTPs and thus deeper convective clouds (heights greater than ~10 km), while red shading represents shallow cloud-top heights (less than ~3 km). For reference, islands of western Indonesia are seen in the upper-right portion of the plot. See text for discussion.

Chapter 5

Summary and Conclusions

The Madden-Julian Oscillation is a complex, convectively-coupled wave operating in the chaotic atmospheric background of the warm-ocean tropical regions. Spectral decomposition of a host of atmospheric (and some oceanic) variables isolates the MJO signal from other wave types and highlights its dominance of tropical intraseasonal variability. Although the MJO is most active within about 15° of the Equator in the Indian and West Pacific Ocean areas, it both influences and is influenced by the extratropics. Unfortunately, the Indian Ocean is one of the most data-sparse regions in the world, with only a handful of stations providing comprehensive surface-based atmospheric measurements. This problem is partially offset by the recent advances and successes of satellite programs such as TRMM, MODIS, and ICESat, which have vastly enhanced meteorological datasets for the geographic locations in question. Despite these advances, improvements in many aspects of the datasets—including precipitation algorithms, spatial and vertical resolution, and more accurate handling of cloud overlap and multiple cloud layers—are necessary. Additionally, a longer data record would greatly benefit climatological or composite studies of the MJO due to the relative infrequency of significant events (1-2 per boreal winter).

This thesis focuses on a number of key elements involved in the birth and death of the MJO wave. Each event analyzed, whether individually or in a composite, is based on the day of maximum total unfiltered rainfall as estimated using TRMM data. Owing to the relatively recent inception of TRMM, exploring the MJO based on comparatively-higher temporal and spatial resolution hydrological data would have been nearly impossible a decade ago. We chose rainfall as the event basis because of its strong ties to latent heating,

the primary driving force of tropical atmospheric circulations. These circulations exist on numerous scales, including cloud-scale turbulence, mesoscale precipitation processes, and planetary motion systems. The precise interaction among these scales remains a vexing problem in the study of the MJO.

The results of this report suggest that reanalysis data is of suitable use in capturing the mesoscale features of the approach and departure of the MJO wet phase. Most previous research studies utilize smoothed or filtered data fields that, while providing “cleaner” results, might miss potentially important small-scale features such as the immediate post-convective drying signal seen in the present study. We have also seen abundant evidence of shallow cumulus activity prior to intense MJO-related rainfall, a physical process that could be masked by smoothing or filtering. In general, the statistical approach used in analyzing certain MJO mechanisms must cater to the scale of that mechanism, which is why we elected to use unfiltered, high-resolution rainfall within a filtered, MJO-related convective envelope.

Our analysis highlights the importance of shallow convective heating and moistening by cumuli prior to the arrival of the intense rainfall (the “birth” of the MJO). During the two weeks leading up to day 0, convective vertical transport of T and q in the lower troposphere and extending into the middle troposphere plays a critical role in “preconditioning” the environment for deep convection, as in Bladé and Hartmann (1993) and K-CW01. Near day 0, precipitation processes evolve from convective to stratiform, according to the vertical structures of Q_1 and Q_2 . Concerning the “death” of the MJO, we note distinct vertical and temporal drying processes. The composite results indicate that there is a tendency for the horizontal winds (\mathbf{v}_h) to be associated with low-level drying soon after the most intense precipitation has ended. This drying related to the initial \mathbf{v}_h maximum occurs a few days earlier than the onset of deep-layer subsidence and 1-2 weeks earlier than the most intense subsidence. We note in the ERA40 data composite that a second \mathbf{v}_h maxi-

imum [the “westerly wind burst” (WWB)] follows the most intense precipitation by ~10-15 days and is associated with deep-layer subsidence drying. Previous studies, including HS94 and MH98, implement smoothed data fields to analyze this delayed post-convective drying. While our results strongly support their findings, we point out that a more immediate drying associated with the horizontal winds may play an important role only a few days following intense rainfall. We hope to conduct further analysis of this potentially important drying process in the future. Finally, spatial map sequences (Section 4.2.3) provide some evidence of the role that subtropical dry-air intrusions play in the drying associated with the WWB.

In terms of wave theories in explaining instabilities and growth associated with the MJO, we find that many of our results are in support of the discharge-recharge hypothesis [Bladé and Hartmann (1993), Hu and Randall (1994), K-CW01]. Preconditioning of the atmosphere by low-level heating and moistening, a fundamental aspect of the discharge-recharge theory, is clearly noted in the results of this study. Although certain elements of generalized wave-CISK, WISHE, and stratiform instability mechanisms are seen, several inconsistencies prohibited a direct application of any one of these proposals to the observed MJO.

Although research on the MJO is currently entering its fourth decade, many aspects of this tropical wave remain a mystery. Which triggering mechanisms operate within the area where the signal emerges (West and Central Indian Ocean), and how does the MJO maintain its rigorous periodicity? To what degree is WISHE important in wave initiation within the Western Indian Ocean region? Are extratropical interactions with the MJO common, and how do these interactions influence MJO wave activity? What observational information is needed to improve model depictions of the MJO? These questions (and many more) face today’s atmospheric scientists who research the MJO. It is our intent to further explore these issues—including wave triggering mechanisms, extratropical connections,

scale interactions, and cloud processes—in the coming years. We also hope to incorporate simplified model and/or general circulation model tests as a means of examining the physical interactions that make the Madden-Julian Oscillation so complex.

Appendix A

Composite Anomaly Calculation

Figure A.1 is a graphical representation of the anomaly calculation used to construct the MJO composite cross-sections. The time-height cross-sections displayed on the left side of Fig. A.1 represent *raw, unfiltered* values of non-precipitation variables. This anomaly calculation procedure is not applied to TRMM rainfall. Essentially, timeseries arrays spanning the chosen lag days (-30 to +20) at a particular pressure level are extracted from each event. The arrays are summed according to lag day to create timeseries A_i . The A_i array itself is summed over all lag days and divided by the grand total number of time points, T . We interpret \bar{A} as the expected value of variable x during an MJO convective event at a particular pressure level. The anomaly A_i' is then calculated as the average of variable x at a particular time lag minus the expected value. All non-precipitation composite cross-sections displayed in Chapter 3 and Sections 4.1 and 4.2.1 involve A' , representing the departure from the expected value (the mean atmospheric state during an MJO event).

We use this calculation method because it cleanly separates anomaly structures from the background state. At an earlier stage of this work, departures from the long-term (18-year) calendar-day averages for each gridpoint were implemented. Using this original procedure, a few of the composite cross-sections displayed like-signed anomalies for most lag times and pressure levels, despite the coherent MJO structures within the cross-section. For example, the temperature composite displayed positive anomalies throughout the cross-section, suggesting that (a) the tropical troposphere during the late 1990s was warmer than previous decades, or (b) MJO events tend to occur in an environment in which much of the

tropical troposphere is warmer than the long-term average. The modified anomaly computation described in Fig A.1 eliminates this small problem through comparison with an MJO background state. For most variables, however, the difference between basing anomalies on climatology or the MJO background state is largely insignificant. In addition, the modified anomaly guarantees a zero time mean, a useful property when calculating time-mean covariances (see Section 4.2.1).

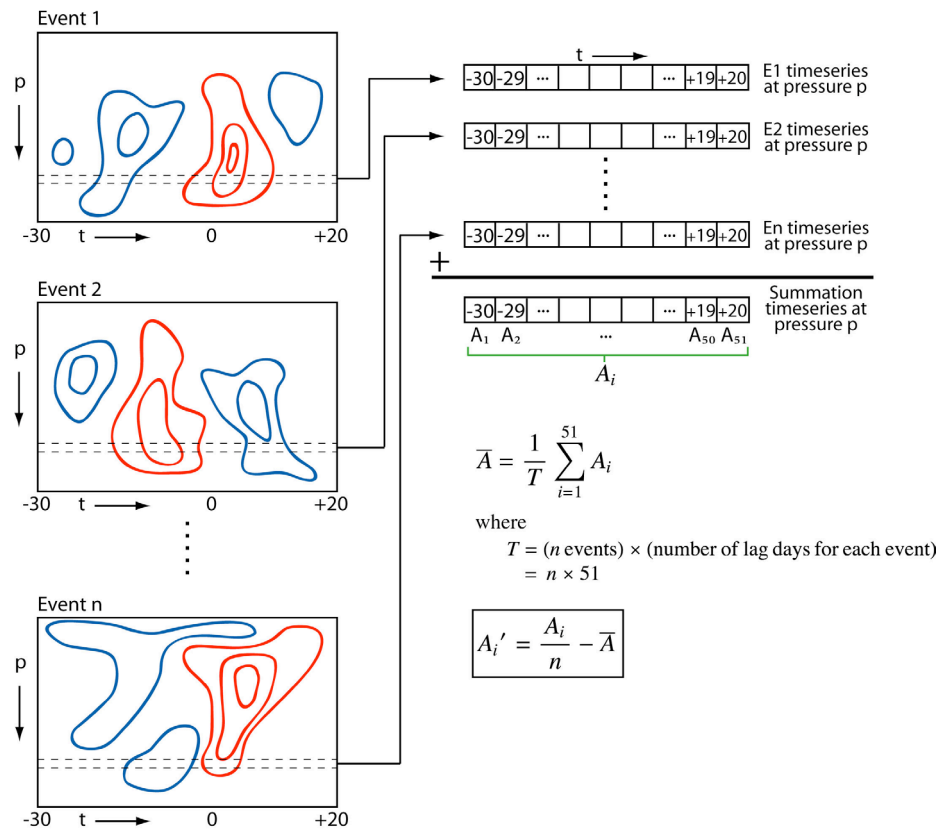


Figure A.1: Illustration detailing the anomaly calculations used to construct MJO composite cross-sections.

Appendix B

Heat and Moisture Budget Analysis: Advective Form

A budget analysis of the thermodynamic energy equation in advective form is performed in order to investigate which terms contribute to the sign and magnitude of $\frac{\partial T'}{\partial t}$. We begin with the thermodynamic energy equation:

$$c_v \frac{DT}{Dt} + p \frac{D\alpha}{Dt} = \dot{Q} \quad (\text{B1})$$

Invoking the hydrostatic approximation, we may find an alternate expression for α :

$$\rho g = -\frac{\partial p}{\partial z} \quad (\text{B2})$$

$$\frac{g \partial z}{\partial p} = -\frac{1}{\rho}$$

$$\frac{\partial \phi}{\partial p} = -\alpha \quad (\text{B3})$$

In (B1), \dot{Q} represents the rate of heating by radiation (Q_R), net release of latent energy [$L(c - e)$], and the vertical convergence of vertical eddy transport of sensible heat ($-\frac{\partial}{\partial p} \overline{s'w'}$) as in Yanai et al. (1973). In (B1), c_v is specific heat at constant volume, T is temperature, p pressure, and α specific volume. Additionally, density ρ and geopotential ϕ are introduced in (B2) and (B3). Noting that $c_v = c_p - R$ and $p \frac{D\alpha}{Dt} = \frac{D}{Dt} (p\alpha) - \alpha \frac{Dp}{Dt}$, we can rewrite (B1) as

$$(c_p - R) \frac{DT}{Dt} + \frac{D}{Dt} (p\alpha) - \alpha \frac{Dp}{Dt} = \dot{Q}$$

$$c_p \frac{DT}{Dt} - \frac{D(RT)}{Dt} + \frac{D(p\alpha)}{Dt} - \alpha \frac{Dp}{Dt} = \dot{Q}$$

Utilizing the equation of state ($p\alpha = RT$), the definition $\frac{Dp}{Dt} = \omega$, and the hydrostatic relation (B3), the second and third terms of the LHS cancel and the above equation becomes

$$\begin{aligned}\frac{DT}{Dt} + \frac{\omega}{c_p} \frac{\partial \phi}{\partial p} &= \frac{\dot{Q}}{c_p} \\ \frac{DT}{Dt} &= -\frac{1}{c_p} \left(\omega \frac{\partial \phi}{\partial p} \right) + \frac{\dot{Q}}{c_p}\end{aligned}\tag{B4}$$

We are seeking the term $\frac{\partial T'}{\partial t}$, and to get this we must calculate (B4) – ($\overline{\text{B4}}$):

$$\begin{aligned}\frac{DT}{Dt} &= -\frac{1}{c_p} \left(\omega \frac{\partial \phi}{\partial p} \right) + \frac{\dot{Q}}{c_p} \\ -\frac{D\overline{T}}{Dt} &= -\frac{1}{c_p} \left(\overline{\omega \frac{\partial \phi}{\partial p}} \right) - \frac{\overline{\dot{Q}}}{c_p} \\ \frac{DT'}{Dt} &= -\frac{1}{c_p} \left(\omega \frac{\partial \phi}{\partial p} \right)' + \frac{\dot{Q}'}{c_p}\end{aligned}$$

$$\frac{\partial T'}{\partial t} = -\left(u \frac{\partial T}{\partial x}\right)' - \left(v \frac{\partial T}{\partial y}\right)' - \left(\omega \frac{\partial T}{\partial p}\right)' - \frac{1}{c_p} \left(\omega \frac{\partial \phi}{\partial p}\right)' + \frac{\dot{Q}'}{c_p}\tag{B5}$$

Equation (B5) allows us to analyze how each of the advective terms affects the local time rate of change of the temperature anomaly T' . The fifth term on the LHS, $\frac{\dot{Q}'}{c_p}$, will not be explicitly dealt with in the current analysis as no heating or radiative data is available on individual pressure levels (aside from the surface and TOA) in the ERA40 dataset we obtained.

Similar to the thermodynamic energy budget analysis above, an analysis of the water vapor budget equation in advective form is also performed in order to investigate which terms contribute to the sign and magnitude of $\frac{\partial q'}{\partial t}$. A general form of the water vapor budget equation is:

$$\frac{Dq}{Dt} = S_q - C \quad (\text{B6})$$

where S_q is the vapor source term (evaporation) and C is the vapor sink term (condensation). As with the thermodynamic equation, we must remove the time-mean of each term in order to obtain $\frac{\partial q'}{\partial t}$.

$$\begin{aligned} \frac{Dq}{Dt} &= S_q - C \\ -\frac{D\bar{q}}{Dt} &= -\bar{S}_q + \bar{C} \\ \hline \frac{Dq'}{Dt} &= S_q' - C' \end{aligned}$$

$$\boxed{\frac{\partial q'}{\partial t} = -\left(u \frac{\partial q}{\partial x}\right)' - \left(v \frac{\partial q}{\partial y}\right)' - \left(\omega \frac{\partial q}{\partial p}\right)' + S_q' - C'} \quad (\text{B7})$$

Equation (B7) allows us to analyze the contributions of the various advection terms to the quantity $\frac{\partial q'}{\partial t}$. The water vapor source and sink terms [fourth and fifth terms on the RHS of (B7)] are not explicitly analyzed due to the difficulty in calculating those variables on individual pressure levels.

Appendix C

Simple Forms of the Apparent Convective Heat Source (Q_1) and Apparent Moisture Sink (Q_2)

The derivation of Q_1 , the apparent heat source, has its origins in the thermodynamic energy equation:

$$c_p \frac{DT}{Dt} - \alpha \frac{Dp}{Dt} = Q_1 \quad (C1)$$

Here, Q_1 represents heating by radiation (Q_R), net latent heating [$L(c - e)$], and the vertical convergence of vertical eddy transport of sensible heat ($-\frac{\partial}{\partial p} \overline{s'w'}$) as in Yanai et al. (1973). In (C1), c_p is the specific heat at constant pressure, T temperature, α specific volume, and p pressure. Let $\frac{Dp}{Dt} = \omega$. Invoking the hydrostatic approximation, we find an alternate expression for α :

$$\rho g = -\frac{\partial p}{\partial z} \quad (C2)$$

$$\frac{g \partial z}{\partial p} = -\frac{1}{\rho}$$

$$\frac{\partial \phi}{\partial p} = -\alpha \quad (C3)$$

Substituting the results of (C3) into (C1),

$$\begin{aligned} Q_1 &= c_p \frac{DT}{Dt} + \omega \frac{\partial \phi}{\partial p} \\ &= c_p \left(\frac{\partial T}{\partial t} + \mathbf{v}_h \cdot \nabla_h T + \omega \frac{\partial T}{\partial p} \right) + \omega \frac{\partial \phi}{\partial p} \\ &= c_p \left(\frac{\partial T}{\partial t} + \mathbf{v}_h \cdot \nabla_h T \right) + \omega \frac{\partial}{\partial p} (c_p T + \phi) \\ Q_1 &= c_p \left(\frac{\partial T}{\partial t} + \mathbf{v}_h \cdot \nabla_h T \right) + \omega \frac{\partial s}{\partial p} \end{aligned} \quad (C4)$$

Recall that the dry static energy $s \equiv c_p T + gz = c_p T + \phi$, where we have neglected any changes of gravity with height. Here, s is the summation of the internal and potential energies, g the gravitational constant, z the geometric height, and ϕ the geopotential. The $\frac{\partial s}{\partial p}$ term on the RHS of (C4) may be written alternatively as:

$$\frac{\partial s}{\partial p} = \frac{\partial}{\partial p} (c_p T) + g \frac{\partial z}{\partial p} \quad (\text{C5})$$

$$\frac{\partial s}{\partial p} = \frac{\partial}{\partial p} (c_p T) - \frac{1}{\rho} \quad (\text{C6})$$

$$\frac{\partial s}{\partial p} = c_p \frac{\partial T}{\partial p} - \frac{RT}{p} \quad (\text{C7})$$

$$\begin{aligned} \frac{\partial s}{\partial p} &= c_p \left[-\frac{RT}{p} \frac{1}{c_p} + \frac{\partial T}{\partial p} \right] \\ &= c_p \left(\frac{p}{p_o} \right)^\kappa \left[-\kappa T \left(\frac{p_o}{p} \right)^\kappa \left(\frac{1}{p} \right) + \left(\frac{p_o}{p} \right)^\kappa \frac{\partial T}{\partial p} \right] \\ &= c_p \left(\frac{p}{p_o} \right)^\kappa \left[T p_o^\kappa (-\kappa p^{-\kappa-1}) + \left(\frac{p_o}{p} \right)^\kappa \frac{\partial T}{\partial p} \right] \\ &= c_p \left(\frac{p}{p_o} \right)^\kappa \left[T p_o^\kappa \frac{\partial}{\partial p} (p^{-\kappa}) + \left(\frac{p_o}{p} \right)^\kappa \frac{\partial T}{\partial p} \right] \\ &= c_p \left(\frac{p}{p_o} \right)^\kappa \left[T \frac{\partial}{\partial p} \left(\frac{p_o}{p} \right)^\kappa + \left(\frac{p_o}{p} \right)^\kappa \frac{\partial T}{\partial p} \right] \end{aligned}$$

$$\frac{\partial s}{\partial p} = c_p \left(\frac{p}{p_o} \right)^\kappa \frac{\partial}{\partial p} \left[T \left(\frac{p_o}{p} \right)^\kappa \right] \quad (\text{C8})$$

$$\therefore \frac{\partial s}{\partial p} = c_p \left(\frac{p}{p_o} \right)^\kappa \frac{\partial \theta}{\partial p} \quad (\text{C9})$$

where the hydrostatic approximation has been applied to (C5), the equation of state ($-\frac{1}{\rho} = -\frac{RT}{p}$) has been applied to (C6), and Poisson's equation ($\theta = T \left(\frac{p_o}{p} \right)^\kappa$) has been applied to (C8). In the brief derivation above, R is the dry air gas constant, $\kappa \equiv \frac{R}{c_p}$, and θ is potential temperature. The substitution of (C9) into (C4) yields

$$\boxed{\frac{Q_1}{c_p} \equiv \left[\frac{\partial T}{\partial t} + \mathbf{v}_h \cdot \nabla_h T + \left(\frac{p}{p_o} \right)^\kappa \omega \frac{\partial \theta}{\partial p} \right]} \quad (\text{C10})$$

In (C10), $p_o = 1000$ hPa and each term represents an average over a single ERA40 gridbox ($\sim 8 \times 10^4$ km²). Frequently, the quantity $\frac{Q_1}{c_p}$ is analyzed because it has the more familiar units (K/day).

The derivation of Q_2 , the apparent moisture sink, may be derived from a simple moisture budget equation in pressure coordinates:

$$\begin{aligned}
 L(e - c) &= L \frac{Dq}{Dt} \\
 L(c - e) &= -L \left[\frac{\partial q}{\partial t} + \mathbf{v}_h \cdot \nabla_h q + \omega \frac{\partial q}{\partial p} \right] \\
 \boxed{\frac{Q_2}{c_p} \equiv \frac{L}{c_p} (c - e) = \frac{-L}{c_p} \left[\frac{\partial q}{\partial t} + \mathbf{v}_h \cdot \nabla_h q + \omega \frac{\partial q}{\partial p} \right]} & \quad (C11)
 \end{aligned}$$

In (C11), L is the latent heat of condensation at 0° C; c and e the condensation and evaporation rates, respectively, as functions of height, and q the specific humidity. As with the apparent heat source Q_1 , each term represents an average over a single gridbox ($\sim 8 \times 10^4$ km²), and the apparent moisture sink Q_2 is analyzed in terms of the quantity $\frac{Q_2}{c_p}$, which has units of (K/day).

References

- Arakawa, A., and W. H. Schubert, 1974: Interaction of a Cumulus Cloud Ensemble with the Large-Scale Environment, Part I. *J. Atmos. Sci.*, **31**, 674-701.
- Biello, J. A., and A. J. Majda, 2005: A New Multi-Scale Model for the Madden-Julian Oscillation. *J. Atmos. Sci.* (submitted July 2004).
- Bladé, I., and D. L. Hartmann, 1993: Tropical Intraseasonal Oscillations in a Simple Nonlinear Model. *J. Atmos. Sci.*, **50**, 2922-2939.
- Charney, J. G., 1963: A Note on Large-Scale Motions in the Tropics. *J. Atmos. Sci.*, **20**, 607-609.
- Chang, C.-P., 1977: Viscous Internal Gravity Waves and Low-Frequency Oscillations in the Tropics. *J. Atmos. Sci.*, **34**, 901-910.
- Cho, H.-K., K. Bowman, and G. North, 2004: Equatorial Waves Including the Madden-Julian Oscillation in TRMM Rainfall and OLR Data. *J. Climate*, **22**, 4387-4406.
- Cox, S. K., and K. T. Griffeth, 1979: Estimates of Radiative Divergence during Phase III of the GARP Atlantic Tropical Experiment. Part I: Methodology. *J. Atmos. Sci.*, **36**, 586-601.
- Danielsen, E. F., 1993: In Situ Evidence of Rapid, Vertical, Irreversible Transport of Lower Tropospheric Air into the Lower Tropical Stratosphere by Convective Cloud

Turrets and by Large-Scale Upwelling in Tropical Cyclones. *J. Geophys. Res.*, **98**, 8665-8681.

DeMott, C. A., and S. A. Rutledge, 1998: The Vertical Structure of TOGA COARE Convection. Part II: Modulating Influences and Implications for Diabatic Heating. *J. Atmos. Sci.*, **55**, 2748-2762.

Dessler, A. E., and P. Yang, 2003: The Distribution of Tropical Thin Cirrus Clouds Inferred from Terra MODIS Data. *J. Climate*, **16**, 1241-1247.

Emanuel, K. A., 1987: An Air-Sea Interaction Model of Intraseasonal Oscillations in the Tropics. *J. Atmos. Sci.*, **44**, 2324-2340.

———, 1994: *Atmospheric Convection*. Oxford University Press, New York, 580 pp.

———, J. D. Neelin, and C. S. Bretherton, 1994: On Large-Scale Circulations in Convecting Atmospheres. *Quart. J. Roy. Meteor. Soc.*, **120**, 1111-1143.

Gill, A. E., 1980: Some Simple Solutions for Heat Induced Tropical Circulation. *Quart. J. Roy. Meteor. Soc.*, **106**, 447-462.

Grabowski, W. W., 2003: MJO-Like Coherent Structures: Sensitivity Simulations Using the Cloud-Resolving Convection Parameterizations (CRCP). *J. Atmos. Sci.*, **60**, 847-864.

———, and M. W. Moncrieff, 2005: Moisture-Convection Feedbacks in the Tropics. *Quart. J. Roy. Meteor. Soc.* (submitted July 2003).

- , 2005: Impact of Explicit Atmosphere-Ocean Coupling on Tropical Intraseasonal Oscillations. *J. Atmos. Sci.* (submitted January 2005).
- Hayashi, Y., 1970: A Theory of Large-Scale Equatorial Waves Generated by Condensation Heat and Accelerating the Zonal Wind. *J. Meteor. Soc. Japan*, **48**, 140-160.
- Hendon, H. H., and M. L. Salby, 1994: The Life Cycle of the Madden-Julian Oscillation. *J. Atmos. Sci.*, **51**, 2225-2237.
- Houze, R. A., Jr., 1982: Cloud Clusters and Large-Scale Vertical Motions in the Tropics. *J. Meteor. Soc. Japan*, **60**, 396-410.
- , 1997: Stratiform Precipitation in Regions of Convection: A Meteorological Paradox? *Bull. Amer. Meteor. Soc.*, **78**, 2179-2196.
- Hsu, H.-H., B. J. Hoskins, and F.-F. Jin, 1990: The 1985/1986 Intraseasonal Oscillation and the Role of the Extratropics. *J. Atmos. Sci.*, **47**, 823-839.
- Hu, Q., and D. A. Randall, 1994: Low-Frequency Oscillations in Radiative-Convective Systems. *J. Atmos. Sci.*, **51**, 1089-1099.
- Jin, Y., W. B. Rossow, and D. P. Wylie, 1996: Comparison of the Climatologies of High-Level Clouds from HIRS and ISCCP. *J. Climate*, **9**, 2850-2879.
- Johnson, R. H., and G. Young, 1983: Heat and Moisture Budgets of Tropical Mesoscale Anvil Clouds. *J. Atmos. Sci.*, **40**, 2138-2147.

———, P. E. Ciesielski, and K. A. Hart, 1996: Tropical Inversions at the 0°C Level. *J. Atmos. Sci.*, **53**, 1838-1855.

———, T. M. Rickenbach, S. A. Rutledge, P. E. Ciesielski, and W. H. Schubert, 1999: Trimodal Characteristics of Tropical Convection. *J. Climate*, **12**, 2397-2418.

Kemball-Cook, S. R., and B. C. Weare, 2001: The Onset of Convection in the Madden-Julian Oscillation. *J. Climate*, **14**, 780-793.

Kikuchi, K., and Y. N. Takayabu, 2004: The Development of Organized Convection Associated with the MJO during TOGA COARE IOP: Trimodal Characteristics. *Geophys. Res. Lett.*, **31**, L10101.

King, M. D., W. P. Menzel, Y. J. Kaufman, D. Tanré, B.-C. Gao, S. Platnick, S. A. Ackerman, L. A. Remer, R. Pincus, and P. A. Hubanks, 2003: Cloud and Aerosol Properties, Precipitable Water, and Profiles of Temperature and Water Vapor from MODIS. *IEEE Transactions on Geoscience and Remote Sensing*, **41**, 442-458.

Kummerow, C., J. Simpson, O. Thiele, W. Barnes, A. T. C. Chang, E. Stocker, R. F. Adler, A. Hou, R. Kakar, F. Wentz, P. Ashcroft, T. Kozu, Y. Hong, K. Okamoto, T. Iguchi, H. Kuroiwa, E. Im, Z. Haddad, G. Huffman, B. Ferrier, W. S. Olson, E. Zipser, E. A. Smith, T. T. Wilheit, G. North, T. Krishnamurti, and K. Nakamura, 2000: The Status of the Tropical Rainfall Measuring Mission (TRMM) After Two Years in Orbit. *J. Appl. Meteor.*, **39**, 1965-1982.

- Lin, X., and R. H. Johnson, 1996a: Kinematic and Thermodynamic Characteristics of the Flow Over the Western Pacific Warm Pool during TOGA COARE. *J. Atmos. Sci.*, **53**, 695-715.
- , and ———, 1996b: Heating, Moistening, and Rainfall over the Western Pacific Warm Pool during TOGA COARE. *J. Atmos. Sci.*, **53**, 3367-3383.
- Lindzen, R. S., 1974: Wave-CISK in the Tropics. *J. Atmos. Sci.*, **31**, 156-179.
- Lorenz, E. N., 1955: Available Potential Energy and the Maintenance of the General Circulation. *Tellus*, **7**, 157-167.
- Luo, H., and M. Yanai, 1984: The Large-Scale Circulation and Heat Sources over the Tibetan Plateau and Surrounding Areas during the Early Summer of 1979. Part II: Heat and Moisture Budgets. *Mon. Wea. Rev.*, **112**, 966-989.
- Madden, R. A., and P. R. Julian, 1971: Description of a 40-50 Day Oscillation in the Zonal Wind in the Tropical Pacific. *J. Atmos. Sci.*, **28**, 702-708.
- , and ———, 1972: Description of Global-Scale Circulation Cells in the Tropics with a 40-50 Day Period. *J. Atmos. Sci.*, **29**, 1109-1123.
- , and ———, 1994: Observations of the 40-50-Day Tropical Oscillation — A Review. *Mon. Wea. Rev.*, **123**, 814-837.
- Maloney, E. D., and D. L. Hartmann, 1998: Frictional Moisture Convergence in a Composite Life Cycle of the Madden-Julian Oscillation. *J. Climate*, **11**, 2387-2403.

- Majda, A. J., and M. G. Shefter, 2001: Models for Stratiform Instability and Convectively Coupled Waves. *J. Atmos. Sci.*, **58**, 1567-1584.
- Mapes, B. E., 2000: Convective Inhibition, Subgrid-Scale Triggering Energy, and Stratiform Instability in a Toy Tropical Wave Model. *J. Atmos. Sci.*, **57**, 1515-1535.
- Matsuno, T., 1966: Quasi-geostrophic Motions in the Equatorial Area. *J. Meteor. Soc. Japan*, **44**, 25-43.
- Menzel, W. P., W. L. Smith, and T. R. Stewart, 1982: Improved Cloud Motion Wind Vector and Altitude Assignment Using VAS. *J. Climate and App. Meteor.*, **22**, 377-384.
- Meyers, D. S., and D. E. Waliser, 2003: Three-Dimensional Water Vapor and Cloud Variations Associated with the Madden-Julian Oscillation during Northern Hemisphere Winter. *J. Climate*, **16**, 929-950.
- Nakazawa, T., 1988: Tropical Super Clusters within Intraseasonal Variations over the Western Pacific. *J. Meteor. Soc. Japan*, **66**, 823-839.
- Neelin, J. D., I. M. Held, and K. H. Cook, 1987: Evaporation-Wind Feedback and Low-Frequency Variability in the Tropical Atmosphere. *J. Atmos. Sci.*, **44**, 2341-2348.
- Nitta, T., and S. Esbensen, 1974: Heat and Moisture Budget Analyses Using BOMEX Data. *Mon. Wea. Rev.*, **102**, 17-28.
- Numaguti, A., R. Oki, K. Nakamura, K. Tsuboki, N. Misawa, T. Asai, and Y.-M. Kodama, 1995: 4-5-Day-Period Variation on Low-Level Dry Air Observed in the

- Equatorial Western Pacific during the TOGA COARE IOP. *J. Meteor. Soc. Japan*, **73**, 267-290.
- Palm, S., W. Hart, D. Hlavka, E. Welton, A. Mahesh, and J. Spinhirne, 2002: GLAS Atmospheric Data Products. GLAS Algorithm Theoretical Basis Document, Version 4.2.
- Platnick, S., M. D. King, S. A. Ackerman, W. P. Menzel, B. A. Baum, J. C. Riédi, and R. A. Frey, 2003: The MODIS Cloud Products: Algorithms and Examples from Terra. *IEEE Transactions on Geoscience and Remote Sensing*, **41**, 459-473.
- Reed, R. J., and E. E. Recker, 1971: Structure and Properties of Synoptic-Scale Wave Disturbances in the Equatorial Western Pacific. *J. Atmos. Sci.*, **28**, 1117-1133.
- Roundy, P. E., and W. M. Frank, 2004: A Climatology of Waves in the Equatorial Area. *J. Atmos. Sci.*, **61**, 2105-2132.
- Rui, H., and B. Wang, 1990: Development Characteristics and Dynamic Structure of Tropical Intraseasonal Convection Anomalies. *J. Atmos. Sci.*, **47**, 357-379.
- Simmons, A. J., and J. K. Gibson, 2000: The ERA-40 Project Plan. The ERA-40 Project Report Series No. 1. *This report is available online at <http://www.ecmwf.int/publications/library/do/references/list/192>.*
- Stephens, G. L., P. J. Webster, R. H. Johnson, R. Engelen, and T. L'Ecuyer, 2004: Observational Evidence for the Mutual Regulation of the Tropical Hydrological Cycle and Tropical Sea Surface Temperatures. *J. Climate*, **17**, 2213-2224.

- Straub, K. H., and G. N. Kiladis, 2003: The Observed Structure of Convectively Coupled Kelvin Waves: Comparison with Simple Models of Coupled Instability. *J. Atmos. Sci.*, **60**, 1655-1668.
- Troccoli, A., and P. Kållberg, 2004: ERA-40 Project Report Series No. 13: Precipitation Correction in the ERA-40 Reanalysis. *This report is available online at <http://www.ecmwf.int/publications/library/do/references/list/192>.*
- Webster, P. J., and G. L. Stephens, 1980: Tropical Upper-Tropospheric Extended Clouds: Inferences from Winter MONEX. *J. Atmos. Sci.*, **37**, 1521-1541.
- Weickmann, K. M., G. R. Lusk, and J. E. Kutzbach, 1985: Intraseasonal (30-60 Day) Fluctuations of Outgoing Longwave Radiation and 250 mb Stream Function During Northern Winter. *Mon. Wea. Rev.*, **113**, 941-961.
- Wheeler, M., and G. N. Kiladis, 1999: Convectively Coupled Equatorial Waves: Analysis of Clouds and Temperature in the Wavenumber-Frequency Domain. *J. Atmos. Sci.*, **56**, 374-399.
- Yamagata, T., and Y. Hayashi, 1984: A Simple Diagnostic Model for the 30-50 Day Oscillation in the Tropics. *J. Meteor. Soc. Japan*, **62**, 709-717.
- Yanai, M., S. Esbensen, and J.-H. Chu, 1973: Determination of Bulk Properties of Tropical Cloud Clusters from Large-Scale Heat and Moisture Budgets. *J. Atmos. Sci.*, **30**, 611-627.

———, B. Chen, and W.-W. Tung, 2000: The Madden-Julian Oscillation Observed during the TOGA COARE IOP: Global View. *J. Atmos. Sci.*, **57**, 2374-2396.

Yang, G.-Y., B. J. Hoskins, and J. Slingo, 2003: Convectively-Coupled Equatorial Waves: A New Methodology for Identifying Wave Structures in Observational Data. *J. Atmos. Sci.*, **60**, 1637-1654.

Zhang, C., and H. H. Hendon, 1997: Propagating and Standing Components of the Intraseasonal Oscillation in Tropical Convection. *J. Atmos. Sci.*, **54**, 741-752.